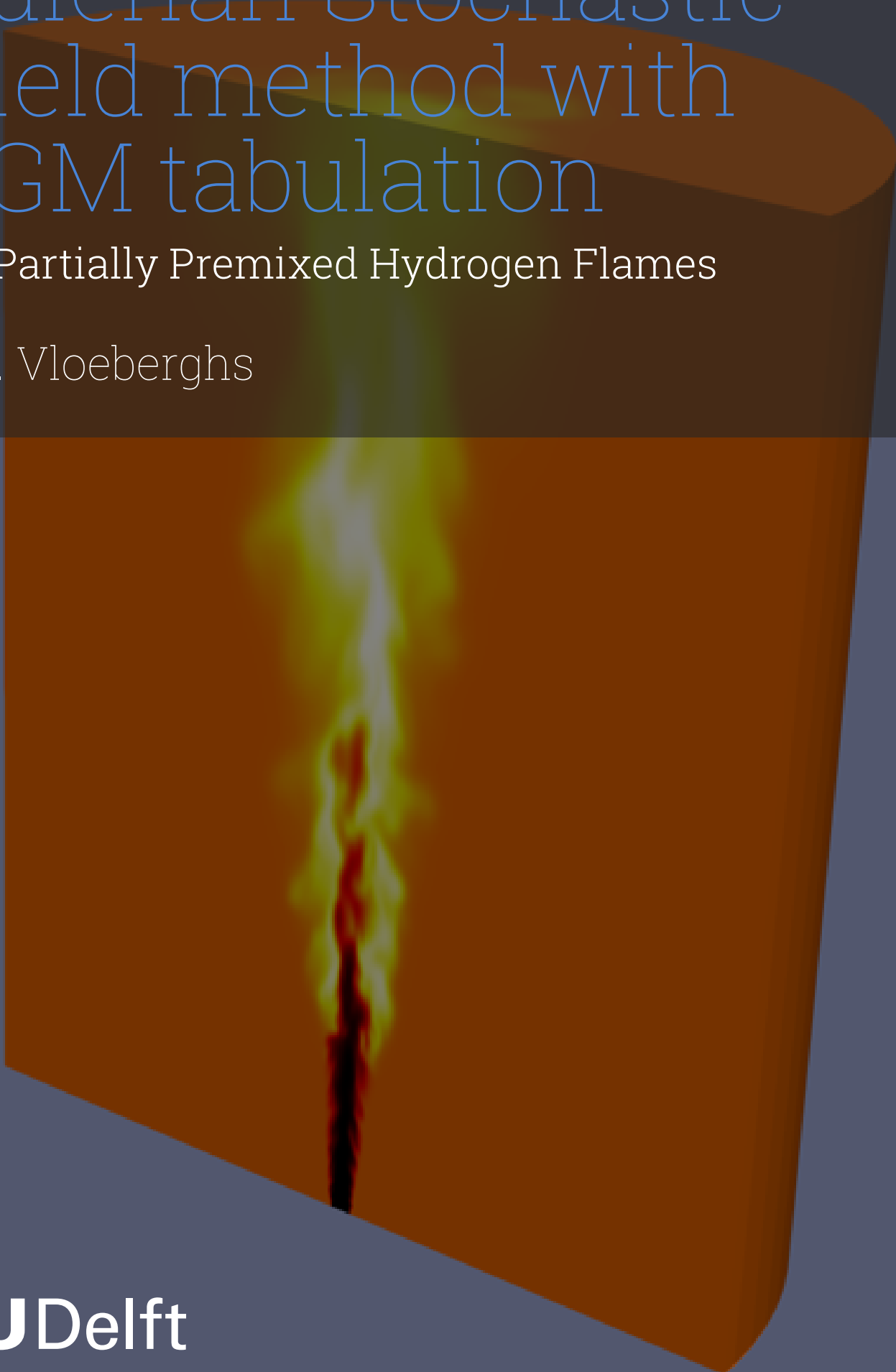


# Eulerian Stochastic Field method with FGM tabulation

for Partially Premixed Hydrogen Flames

V.H. Vloeberghs



# Eulerian Stochastic Field method with FGM tabulation

for Partially Premixed Hydrogen Flames

by

V.H. Vloeberghs

Date: Monday 22<sup>nd</sup> January, 2024  
Project Duration: February, 2023 - February, 2024  
Supervisors: Dr. I. Langella  
Prof.dr. D.J.E.M. Roekaerts  
Faculty: Faculty of Aerospace Engineering, Delft

# Preface

As I present this thesis, a culmination of my journey in Aerospace Engineering, I am filled with a strong sense of gratitude and reflection. This work is not just a testament to my academic pursuit but a mosaic of the invaluable support and guidance I received along the way. Therefore, I would like to use this opportunity to thank a few people in particular who have helped me with this task.

I am very grateful to my supervisors, Ivan and Dirk, for their invaluable guidance and support throughout my journey in numerical combustion. Ivan, despite his extensive commitments, has consistently made time for me, offering insights and advice exactly when needed. His dedication has not only been a source of inspiration but has also played a crucial role in my academic and personal development. Likewise, I owe a great deal of gratitude to Dirk for his exceptional insights into the fundamental theory of combustion. His innovative ideas and fresh perspectives have been a constant source of inspiration, significantly enriching both my understanding and approach to the subject. Both Ivan and Dirk have been steadfast in their mentorship, often challenging me to strive for excellence. Their insistence on diligence and to delve deeper, though occasionally testing my patience, has undeniably helped develop my analytical skills and academic rigour. The success of the code and the quality of this thesis are testaments to their unwavering commitment and guidance. Without their expertise and encouragement, the achievements encapsulated in this work would not have been realized to such an extent.

I would also like to thank Gioele Ferrante whose foundational work on the Cabra flame has been instrumental to my research. Gioele's readiness to assist with practical questions and his extensive work on the Cabra flame through his PhD have significantly accelerated many aspects of my work. His efforts have not only facilitated my progress in code development and postprocessing but have been essential in achieving the level of sophistication and depth evident in my current work. Furthermore, collaborating on the same case with Gioele has continually motivated me, especially in overcoming the numerous challenges and perplexing contradictions inherent in the field of numerical combustion modelling. I would also like to extend my gratitude to other members of the numerical combustion group during my thesis, Boris, Alessandro and Maria, for their time and assistance in this project.

*V.H. Vloeberghs  
Delft, January 2024*

# Abstract

The thesis presents a potential new tool for modelling hydrogen combustion in aircraft combustors, an important step towards the reduction of emissions in aviation. After analysing available models in the literature, the method combining the Eulerian Stochastic Field method with Flamelet Generated Manifold tabulation (FGM-ESF) is selected as the most suitable candidate. This hybrid model can handle the complex flow dynamics typical in combustors, efficiently managing high turbulence and adapting to both premixed and non-premixed combustion modes, while maintaining computational costs at a manageable level. To validate the model on a complex set of regimes, the lifted turbulent  $H_2/N_2$  jet flame in a vitiated coflow, known as the Cabra flame, is selected as the validation case.

The FGM-ESF model aligns well with experimental data in predicting mean velocity, temperature, and mixture fraction. However, it slightly overestimates the root mean square (rms) values of these parameters, likely due to slower mixing rates. Despite this, it closely approximates the FC-ESF outcomes. Notably, the model's performance shows minimal sensitivity to the number of Eulerian stochastic fields used, with two fields being sufficient for effective simulation. Further analysis of instantaneous burning states reveals that the FGM-ESF model typically predicts faster reaction times and higher peak temperatures and water vapour mass fractions relative to the FC-ESF approach. Although these minor differences exist, the FGM-ESF model adeptly captures key qualitative features, such as the prediction of super-adiabatic conditions and a distinct double-peak pattern in conditional reaction rates. Additionally, the computational demands of the FGM-ESF model show reduced sensitivity to the number of stochastic fields relative to the FC-ESF.

The FGM-ESF model effectively captures key features and shows computational efficiency, with the potential for further optimization in parallel computing routines. The thesis demonstrates the FGM-ESF to be a valuable asset by offering a blend of precision and cost-efficiency that is essential for the future development of hydrogen aircraft engines.

# Contents

<b>Abstract</b>	<b>ii</b>
<b>Nomenclature</b>	<b>iv</b>
<b>1 Introduction</b>	<b>1</b>
1.1 Role of emissions in climate change . . . . .	1
1.1.1 Carbon-based emissions . . . . .	1
1.1.2 Nitrogen oxides . . . . .	3
1.1.3 Reducing harmful emissions . . . . .	4
1.2 Hydrogen as a fuel . . . . .	6
1.2.1 Production . . . . .	6
1.2.2 Storage and transportation . . . . .	7
1.2.3 Consumption . . . . .	7
1.3 Towards a hydrogen combustor . . . . .	9
1.3.1 Conventional gas turbine combustors . . . . .	9
1.3.2 Challenges for hydrogen combustors . . . . .	9
1.3.3 Hydrogen combustion designs . . . . .	11
1.3.4 Hydrogen combustion model requirements . . . . .	12
<b>2 Theoretical background</b>	<b>14</b>
2.1 Non-reactive flows . . . . .	14
2.1.1 Governing equations of non-reactive flows . . . . .	14
2.1.2 Direct Numerical Simulation . . . . .	15
2.1.3 Large Eddy Simulation . . . . .	17
2.1.4 Eddy-viscosity models . . . . .	21
2.2 Reactive flows . . . . .	24
2.2.1 Premixed and non-premixed combustion . . . . .	24
2.2.2 Chemical Kinetics . . . . .	25
2.2.3 Thermodynamics of combustion processes . . . . .	26
2.2.4 Governing equations of reactive flows . . . . .	27
2.2.5 Modelling turbulent flames . . . . .	29
2.2.6 Numerical solution algorithms . . . . .	30
<b>3 Literature review</b>	<b>32</b>
3.1 Modelling chemical kinetics . . . . .	32
3.1.1 Detailed chemistry and reduced schemes . . . . .	32
3.1.2 Flamelet-tabulation approach . . . . .	33
3.2 Subgrid-scale flame-turbulence interaction . . . . .	36
3.2.1 Geometric approach . . . . .	36
3.2.2 Mixing approach . . . . .	37
3.2.3 Statistical approach . . . . .	38
3.3 Hydrogen flame experiments . . . . .	41
3.3.1 Swirl burner . . . . .	41
3.3.2 Cabra flame . . . . .	42
3.4 Selected model and research questions . . . . .	45
<b>4 Paper</b>	<b>47</b>
<b>5 Conclusion</b>	<b>82</b>
<b>References</b>	<b>84</b>

# Nomenclature

## Abbreviations

Abbreviation	Definition
CMC	Conditional Moment Closure
CSP	Computational Singular Perturbation
EDC	Eddy Dissipation Concept
ESF	Eulerian Stochastic Fields
ETS	Emissions Trading System
FDF	Filtered Density Function
FGM	Flamelet Generated Manifold
FPI	Flame Prolongation of the ILDM
FPV	Flamelet Progress Variable
ILDm	Intrinsic Low-Dimensional Manifold
ILUC	Indirect Land-Use Change
ISAT	In-Situ Adaptive Tabulation
LES	Large Eddy Simulation
LHV	Lower Heating Value
PMC	Particle Monte Carlo
PAN	PeroxyAcetyl Nitrate
PaSR	Partially Stirred Reactor
PDF	Probability Density Function
PEA	Partial Equilibrium Approximation
PFDF	Presumed Filtered Density Function
QSSA	Quasi Steady-State Approximation
RANS	Reynolds-Averaged-Navier–Stokes
REDIM	REAction DIffusion Manifold
RQL	Rich-Quench-Lean
SAF	Sustainable Aviation Fuels
SMR	Steam Methane Reforming
SGS	SubGrid Scale
TFDF	Transported Filtered Density Function
VOC	Volatile Organic Compounds
WALE	Wall-Adapting Local Eddy-viscosity

## Symbols

Bold symbols indicate a vector or matrix.

Symbol	Definition
$c$	Normalised progress variable
$c_p$	Specific heat capacity at constant pressure
$D_m$	Mass diffusivity of species $m$
$D_{th}$	Thermal diffusivity
$h_s$	Sensible enthalpy
$k$	Kinetic energy
$Le$	Lewis number
$N$	Number of stochastic fields
$n_r$	Number of reactions
$n_s$	Number of species
$n_\alpha$	Number of controlling variables
$\mathcal{P}$	Fine-grained composition PDF
$p$	Pressure
$Pr$	Prandtl number
$\mathcal{R}$	Perfect gas constant
$Re$	Reynolds number
$S_{ij}$	Strain rate tensor
$s_L$	Laminar flame speed
$s_T$	Turbulent flame speed
$Sc$	Schmidt number
$T$	Temperature
$t$	Time
$u_i$	Velocity component in direction $i$
$V_{mi}$	Local diffusion velocity in direction $i$ of species $m$
$W_m$	Molecular weight of species $m$
$dW^n$	$n$ -th stochastic realisation of the Wiener process
$x_i$	Cartesian coordinate in direction $i$
$Y_m$	Mass fraction of species $m$
$Z$	Mixture fraction
$\Delta$	LES filter width
$\delta_{ij}$	Kronecker delta
$\varepsilon$	Energy dissipation rate
$\zeta_\alpha^n$	$n$ -th stochastic realisation of $\phi_\alpha$
$\lambda$	Thermal conductivity
$\mu$	Dynamic viscosity
$\nu$	Kinematic viscosity
$\rho$	Density
$\tau_{ij}$	Shear-stress tensor
$\phi_\alpha$	Scalar quantity of the thermo-chemical state
$\chi$	Scalar dissipation rate
$\Psi$	Thermochemical state
$\psi_\alpha$	Sample space of $\phi_\alpha$
$\dot{\omega}_m$	Source term of species $m$
$\dot{\omega}_T$	Combustion heat release

# 1

## Introduction

Hydrogen-powered aircraft represent a crucial advancement in the journey towards achieving net zero emissions by the year 2050. This chapter delves into the critical role that emissions play in climate change and positions hydrogen as a potential game-changer in mitigating these effects. It explores hydrogen as a viable fuel alternative, shedding light on its unique properties and the implications these have for combustion processes. The chapter then addresses the inherent challenges associated with hydrogen combustion, particularly in the context of aviation. This introduction ends by discussing the need for a new hydrogen combustion model, adept at replicating conditions similar to those in gas turbines, a critical step for the successful integration of hydrogen in aviation propulsion systems.

### 1.1. Role of emissions in climate change

Climate change is one of the most important global problems that humankind is confronted with in the next decades. The conversation frequently centres around global warming. This is understood as the warming of the Earth's surface and atmosphere and is caused by the emission of greenhouse gases, which include methane, carbon dioxide, and nitrous oxides. These gases trap heat within the atmosphere, thereby contributing to the global warming effect. However, climate change also encompasses other critical issues like the acidification of oceans and widespread environmental changes that are caused by the emissions of these gases.

In the realms of energy production and transportation, the most prevalent emissions discussed are carbon-based pollutants and nitrogen oxides. These emissions are integral to numerous industrial processes and play a significant role in the changing climate.

#### 1.1.1. Carbon-based emissions

Today's fossil fuel dependence is beautifully described in Daniel Yergin's *The Prize* *"If it can be said, in the abstract, that the sun energized the planet, it was oil that now powered its human population, both in its familiar forms as fuel and in the proliferation of new petrochemical products. Oil emerged triumphant, the undisputed King, a monarch garbed in a dazzling array of plastics. He was generous to his loyal subjects, sharing his wealth to, and even beyond, the point of waste. His reign was a time of confidence, of growth, of expansion, of astonishing economic performance. His largesse transformed his kingdom, ushering in a new drive-in civilization. It was the Age of Hydrocarbon Man."*

Fossil fuels have brought a level of prosperity that was unimaginable in the pre-oil era. Oil has been instrumental in the evolution of transportation. The development of the internal combustion engine and its subsequent use in automobiles, aircraft, ships, and trains revolutionized the way people and goods move around the globe. This revolution not only enhanced mobility but also played a significant role in globalization, connecting distant parts of the world economically and culturally. Oil has been a fundamental driver of the world's economic and industrial development. Its abundant energy has fueled the growth of industries, transportation, and nations, while also playing a central role in global

geopolitics and policy. The key to oil's success as a dominant energy source lies in a unique attribute: it is a form of ancient solar energy, that is stored in carbon bonds and concentrated over millions of years. Accessing this abundance of energy only requires a few steps: extract, refine, transport and burn. However, there also lies its biggest issue. Breaking these age-old carbon bonds releases amounts of carbon dioxide in the air not seen since the Miocene epoch 15 million years ago [1]. This has some important consequences for the quality of the environment.

It has been shown that carbon dioxide plays a pivotal role in global warming. As a greenhouse gas, CO<sub>2</sub> is central to the greenhouse effect. The greenhouse effect is a natural process where certain gases in the Earth's atmosphere, like CO<sub>2</sub>, trap heat from the sun. These gases allow sunlight to enter the atmosphere freely. When the Earth's surface absorbs sunlight, it radiates it back towards space as infrared heat. Greenhouse gases absorb and re-radiate some of this heat, effectively insulating the planet and keeping it warm enough to sustain life. However, an enhanced greenhouse effect, caused by increased CO<sub>2</sub> levels, leads to a rise in global average temperatures. This warming is a key driver of climate change, contributing to a wide range of changes in weather patterns, sea levels, and various aspects of the natural world. Furthermore, higher temperatures can lead to feedback mechanisms that further increase global warming. For example, warming can cause ice and snow to melt, reducing the Earth's reflectivity and causing it to absorb more solar energy. Additionally, warmer temperatures can release more CO<sub>2</sub> captured in natural carbon sinks, like permafrost or forests through increased wildfires. Additionally, these higher global temperatures have led to the melting of polar ice caps and glaciers. This melting contributes to rising sea levels, which can lead to coastal erosion, increased flooding, and the displacement of populations in low-lying areas.

Carbon dioxide also plays a significant role in ocean acidification, a process that poses a serious threat to marine ecosystems. The oceans act as a major sink for atmospheric CO<sub>2</sub>, absorbing about a quarter of the CO<sub>2</sub> emitted by human activities. While this oceanic uptake of CO<sub>2</sub> mitigates the extent of global warming, it also leads to chemical changes in seawater. When CO<sub>2</sub> dissolves in seawater, it reacts with water to form carbonic acid. Carbonic acid is a weak acid and thus, it partially dissociates into bicarbonate and hydrogen ions. The release of these hydrogen ions reduces the pH of seawater, making it more acidic. The increase in hydrogen ions also affects the concentration of carbonate ions in the ocean. This is because hydrogen ions can combine with carbonate ions to form more bicarbonate ions. This reaction reduces the availability of carbonate ions, which are crucial for marine organisms like corals, mollusks, and some plankton species that use carbonate to form their shells and skeletons. The reduction in carbonate ion concentration makes it more difficult for these organisms to build and maintain their calcium carbonate structures. This can lead to weaker shells and skeletons, affecting their survival, growth, and reproduction. Additionally, the overall change in the chemistry of the ocean can affect various biological processes and ecosystems, potentially disrupting the entire marine food web. Ocean acidification can have far-reaching consequences, not just for marine biodiversity, but also for human societies. Many communities rely on marine resources for food, income, and cultural identity. The decline in the health of coral reefs and other marine ecosystems due to acidification can thus have significant ecological, economic, and social impacts.

Aside from CO<sub>2</sub>, there are also other carbon-based emissions. Methane (CH<sub>4</sub>) ranks as the second most dominant greenhouse gas from human activities after CO<sub>2</sub>. Over the initial two decades following its emission, methane is 84 times more potent than carbon dioxide, and it retains a significant impact, being 28 times more potent than carbon dioxide, even after 100 years [2]. Small amounts of methane are emitted by vehicles, but most of it originates from different sources. Methane emissions are primarily associated with the production and transport of fossil fuels like coal, natural gas, and oil. Additionally, significant methane emissions arise from biological sources such as livestock, other agricultural practices, and the decomposition of organic waste in municipal landfills.

Carbon monoxide is a colourless, odourless gas that is harmful when inhaled in large amounts. It is produced by incomplete combustion of fossil fuels and is a component of vehicle exhaust, industrial emissions, and smoke from wildfires or burning biomass. While not a greenhouse gas, CO has an indirect impact on climate as it affects the atmospheric concentration of methane and ozone.

Volatile Organic Compounds (VOCs) are a large group of carbon-containing chemicals that easily evaporate at room temperature. Sources include vehicle emissions, industrial processes, and the use of solvents and consumer products. Some VOCs are harmful on their own, and they also play a significant

role in the formation of ground-level ozone and secondary organic aerosols, both of which impact air quality and climate.

Soot or black carbon is a fine particulate matter produced from incomplete combustion of fossil fuels, biofuel, and biomass. It is carcinogenic and contributes to the melting of ice and snow when it settles on these surfaces by increasing their absorption of sunlight. It also plays a significant role in the formation of contrails, which are condensation trails left by aircraft in the sky. Contrails are essentially clouds formed when water vapour from an aircraft's exhaust gases condenses and freezes around small particles in the exhaust. Persistent contrails and the cirrus clouds they can develop into are of interest in climate science because they have a warming effect on the Earth's surface. These clouds trap heat radiating from the Earth, contributing to the greenhouse effect.

### 1.1.2. Nitrogen oxides

Another important type of emissions are nitrogen oxides, commonly referred to as  $\text{NO}_x$ . They encompass a group of air pollutants, primarily nitric oxide ( $\text{NO}$ ) and nitrogen dioxide ( $\text{NO}_2$ ). A small amount of these gases is formed from natural processes such as lightning strikes or microbial processes in the soil. However, the most significant source of these gases comes from the combustion of fossil fuels.

$\text{NO}$  is formed through several pathways during combustion. For hydrocarbon combustion, five pathways are identified [3]. A simplified schematic of these paths is shown in Figure 1.1. The paths are the following. (1) Thermal  $\text{NO}$  is formed when oxygen and nitrogen in the air combine. It is very sensitive to temperature: a higher temperature leads to more  $\text{NO}$  formation. (2) Prompt  $\text{NO}$  formation occurs in the early stages of combustion when there are high concentrations of hydrocarbon radicals that react with nitrogen in the air. (3) In the  $\text{NNH}$  pathway, nitrogen reacts with a hydrogen radical to form  $\text{NNH}$ . This intermediate oxidises to form  $\text{NO}$ ,  $\text{N}_2\text{O}$  or  $\text{NH}$ . It also happens in the early stages of hydrogen combustion where a lot of hydrogen radicals are available or in fuel-rich conditions when concentrations of oxygen are lower [4]. (4) The  $\text{N}_2\text{O}$  pathway stems from the reaction between nitrogen in the air with atomic oxygen that forms the intermediate  $\text{N}_2\text{O}$ . This species is a precursor to  $\text{NO}$ . In addition to that,  $\text{N}_2\text{O}$  is also an important greenhouse gas. (5) Fuel  $\text{NO}$  is formed with the nitrogen in the fuel instead of the air in contrast to the other four pathways. These gases are central players in various atmospheric chemical reactions, leading to the formation of harmful byproducts associated with several environmental and health issues.

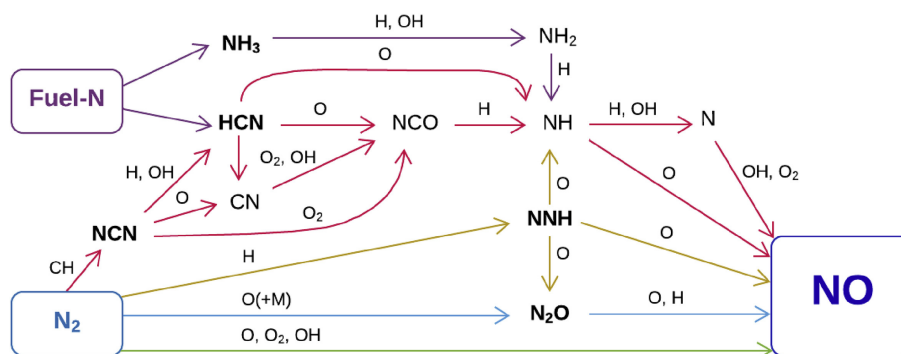


**Figure 1.1:** Simplified scheme of the  $\text{NO}$  formation pathways: thermal  $\text{NO}$  (green), prompt  $\text{NO}$  (red), fuel  $\text{NO}$  (purple),  $\text{N}_2\text{O}$  (blue), and  $\text{NNH}$  (yellow) [5]

$\text{NO}_x$  plays an important role in the formation of smog [6]. There are two types of smog: industrial smog and photochemical smog. While industrial smog results mainly from sulfur dioxide emissions, photochemical smog is intricately linked to  $\text{NO}_x$  emissions. In this type of smog,  $\text{NO}_x$  reacts with VOCs under sunlight, triggering a series of complex chemical reactions. These substances negatively impact vegetation, deteriorate materials like rubber and paint, and pose significant health risks to humans [7]. Notably, ozone, when present in the troposphere, acts as a potent greenhouse gas, contributing to climate change.  $\text{NO}_x$  is also related to acid rain. Nitrogen oxides are a precursor to nitric acid, which is an important component of acid rain [8]. This acidification adversely affects various aspects of the environment: it lowers soil pH, reducing its fertility; acidifies aquatic ecosystems, harming marine life;

and corrodes human-made structures, including significant historical buildings made of limestone and other sensitive materials [9]. In terms of direct health impact, NO<sub>2</sub> itself is particularly harmful. In high concentrations, it is a brown gas with a strong scent that can have a fatal impact on the respiratory system. Even at lower concentrations, NO<sub>2</sub> is associated with mild respiratory issues and asthma leading to chronic health problems [10]. For these reasons, it is important to limit NO<sub>x</sub> emissions as much as possible.

### 1.1.3. Reducing harmful emissions

Although reducing these harmful emissions is a global challenge, Europe has declared that it wants to play a leading role. A key initiative of the European Union in tackling this issue is the "Fit for 55" program. It is a comprehensive legislative package launched by the European Union (EU) as part of its broader European Green Deal initiative. The primary objective of Fit for 55 is to align the EU's climate, energy, land use, transport, and taxation policies with the increased ambition to reduce net greenhouse gas emissions by at least 55% by 2030, compared to 1990 levels. This ambitious target is a significant step towards achieving climate neutrality by 2050.

The package<sup>1</sup>, proposed in July 2021 consists of several key elements, including reforms to the Emissions Trading System (ETS), which is a cornerstone of EU climate policy. The EU proposes to revise its ETS by lowering the cap on emissions from power and industry sectors, thus increasing the price of carbon and incentivizing reductions, and extending the ETS to cover the maritime sector while reducing free emission allowances. In addition, the proposal includes amending the Renewable Energy Directive (RED) and Energy Efficiency Directive (EED) to increase the targets for renewable energy and energy efficiency, involving boosting the production and use of renewable energy across various sectors, including transport, heating, and cooling. The Carbon Border Adjustment Mechanism (CBAM) aims to prevent carbon leakage by imposing a carbon price on imports of certain goods from outside the EU, aligning with the carbon price paid within the EU. Furthermore, the package includes measures to reduce emissions from the aviation and maritime sectors, suggesting integrating all flights departing from the European Economic Area into the ETS and promoting sustainable aviation fuels. This last one is important as aviation plays a notable role in climate change, being responsible for a substantial portion of human-made carbon emissions.

The ReFuelEU Aviation initiative within the Fit for 55 framework focuses on the use of Sustainable Aviation Fuels (SAF) in jet fuel taken onboard at EU airports. The table below shows the binding SAF targets proposed by the initiative.

**Table 1.1:** SAF targets proposed by the ReFuelEU Aviation initiative as part of the "Fit for 55" program. Source: <https://www.easa.europa.eu/en/light/topics/fit-55-and-refueleu-aviation>

	2025	2030	2035	2040	2045	2050
Percentage of SAF used in air transport:	2%	5%	20%	32%	38%	63%
Of which: sub-mandate Synthetic fuels (or e-fuels):	-	0.7%	5%	8%	11%	28%

Several types of SAFs are considered. The first one is advanced biofuels, which are produced from feedstock listed in Annex IX<sup>2</sup>, Part A of the Renewable Energy Directive. This list includes non-food and non-feed biomass, such as certain types of agricultural and forestry residues, non-food cellulosic material, and lignocellulosic material excluding saw logs and veneer logs. These feedstocks are considered sustainable and have a lower risk of creating indirect land-use change (ILUC) effects. ILUC occurs when the production of biofuels displaces agricultural production, leading to deforestation or conversion of non-agricultural land into agricultural land elsewhere. Advanced biofuels from Part A feedstock are highly valued in the EU's sustainability criteria because they use waste and residue materials and do not compete with food crops for land use.

Fuels from Part B Feedstock: These are derived from feedstock listed in Annex IX, Part B of the Renewable Energy Directive. This list typically includes certain types of crops that are not primarily

<sup>1</sup>[https://ec.europa.eu/commission/presscorner/detail/en/ip\\_21\\_3541](https://ec.europa.eu/commission/presscorner/detail/en/ip_21_3541)

<sup>2</sup>[https://eur-lex.europa.eu/legal-content/EN/TXT/?uri=uriserv:OJ.L\\_.2018.328.01.0082.01.ENG&toc=OJ:L:2018:328:TOC](https://eur-lex.europa.eu/legal-content/EN/TXT/?uri=uriserv:OJ.L_.2018.328.01.0082.01.ENG&toc=OJ:L:2018:328:TOC)

used for food or feed. The sustainability of these crops is generally considered to be lower than those in Part A, primarily due to a higher risk of ILUC. However, they are still included in the directive because they can contribute to the diversification of energy sources and have less environmental impact than fossil fuels.

The third category is the synthetic fuels or e-fuels. These Power-to-Liquid (PtL) fuels are not produced from biomass but are synthesised using renewable energy sources like solar or wind power. Hydrogen can be produced from the electrolysis of water and can be even further combined with CO<sub>2</sub> from carbon capture or industrial sources to create e-methane. These e-fuels have important advantages compared to biofuels. The first advantage is reduced competition with land and water resources. E-fuels do not rely on crops or land for their production, avoiding the potential for ILUC or food-versus-fuel debates. Secondly, they have more flexibility in production location. They can be produced anywhere with access to renewable electricity and water. This can reduce transportation costs and emissions associated with moving fuel to where it's needed. In contrast, biofuels are often produced closer to where the biomass is sourced. Thirdly, when used with captured CO<sub>2</sub> sourced from the atmosphere, it can even result in negative emissions. Due to these advantages, they are given a separate sub-mandate in the SAF targets.

Of these synthetic fuels, hydrogen is seen as one of the most promising for a number of reasons. When hydrogen is used as a fuel in aviation, it produces water vapour as the primary byproduct, with no carbon dioxide or other carbon-based pollutants like soot, being emitted during flight. This contrasts sharply with conventional hydrocarbon aviation fuels. Hydrogen also has a high energy density by weight, approximately three times higher than conventional jet fuel. This characteristic is particularly beneficial for aviation, as it could potentially allow for longer flight ranges and lower fuel weight compared to current jet fuels. Thirdly, hydrogen can be used in aviation in several ways, including combustion in modified gas turbine engines or as a power source for fuel cells to generate electrical power. This versatility makes it adaptable to various aviation applications and future technological developments. Hydrogen is also considered an important energy carrier in other sectors, e.g. automotive or marine industry. This could lead to decreased operating costs if the technology matures and is used on a large scale as the infrastructure for its storage and transportation can be shared.

## 1.2. Hydrogen as a fuel

Hydrogen as a fuel has a unique set of characteristics compared to traditional hydrocarbons. Hydrogen is the most abundant element in the universe, but it is rarely found in its pure form on Earth. As a result, it cannot be directly extracted but must be produced through specific processes. Furthermore, hydrogen has an exceptionally high Lower Heating Value (LHV) and reactivity, which poses challenges in handling and utilization. These characteristics make it distinct from conventional fuels and require the whole value chain to be analysed.

### 1.2.1. Production

Hydrogen's simple chemistry and wide range of applications as feedstock, e.g. hydrocracking and ammonia production, have given rise to several production methods.

The most common method for producing commercial bulk hydrogen is Steam Methane Reforming (SMR), which produces what is called *grey hydrogen*. The process involves reacting methane with steam under high pressures and temperatures to produce hydrogen, carbon monoxide, and a relatively small amount of carbon dioxide. SMR is currently the most cost-effective method for producing hydrogen on a large scale, especially where natural gas is abundantly available at low cost. One of the main disadvantages of this process is that it emits carbon dioxide. Therefore, it should be paired with carbon capture and storage (CCS) technologies to mitigate its environmental impact. Hydrogen can also be made through coal gasification, producing *black hydrogen*, by heating coal in the presence of steam and oxygen, which breaks down the coal into a mixture of gases, including hydrogen and carbon monoxide (a mixture known as syngas). The hydrogen can then be separated and purified from this mixture. Similarly, it can also be produced from heavy oil fractions like petroleum coke. Producing *black hydrogen* is even more carbon-intensive than grey hydrogen. CCS technologies are, therefore, even more important. It is also possible to use biomasses.

A cleaner method of hydrogen production is through electrolysis. Electrolysis of water occurs in an electrolyzer, which is essentially a container housing two electrodes (an anode and a cathode) immersed in a water-based electrolyte solution. When electricity is applied, water molecules are split into hydrogen and oxygen. Although no harmful emissions are produced, it is the most expensive process. An overview of the costs of the different methods is given in Table 1.2. The reasons for these high costs are the noble electrocatalyst's high price and high power consumption for breaking the strong bonds in H<sub>2</sub>O [11].

**Table 1.2:** Production cost of different hydrogen production processes [11]

Hydrogen production sources	Hydrogen production cost [USD/kg]
Steam reforming of methane (Liquid Fuel and Natural Gas)	2.27
Gasification of solid fuel (Coal)	1.48
Biomass process	1.80–2.05
Water Electrolysis	10-30

Due to its higher costs, electrolysis is less popular than the other methods. According to the International Renewable Energy Agency <sup>3</sup>, the global production of hydrogen was mainly derived from fossil fuels, with natural gas accounting for nearly 47% of the total production. Coal contributed to 27%, and oil, primarily as a by-product, constituted 22%. In contrast, only about 4% of hydrogen was produced through electrolysis. Considering the global energy mix for electricity, which had a renewable share of roughly 33% in 2021, it can be estimated that only around 1% of the total hydrogen production globally was generated using renewable energy sources. However, there is a lot of ongoing research in reducing the costs of *green hydrogen*. Over the next ten years, the expenses associated with producing hydrogen via electrolysis are expected to decrease significantly, potentially by around 70% [12]. This cost reduction could pave the way for *green hydrogen* production methods to be adopted more broadly. It is a crucial step in reducing greenhouse emissions.

<sup>3</sup><https://www.irena.org/Energy-Transition/Technology/Hydrogen>

### 1.2.2. Storage and transportation

Storage and transportation of hydrogen presents a new set of challenges compared to hydrocarbon fuels.

Firstly, although the mass-energy density of gaseous hydrogen is three times higher compared to hydrocarbons such as kerosene or diesel, its volumetric energy density is only a fraction of that of liquid hydrocarbons [13]. The reason is hydrogen's low density at atmospheric temperatures. There are several methods to mitigate this problem. The most common way is to compress the gas to high pressures (around 700 bar). Compressed hydrogen is typically stored in cylinders or tanks made from materials that can withstand high pressures. While this is a mature technology, the energy required to compress hydrogen and the need for robust tanks to prevent leakage are challenges. Hydrogen can also be liquefied at cryogenic temperatures, which significantly reduces its volume. However, hydrogen has an exceptionally low boiling point of approximately 20.3 K at atmospheric pressure. As a comparison, the boiling point of methane is only 111.5 K. This makes the liquefaction process very energy-intensive and requires special cryogenic storage tanks, making it less energy-efficient and more expensive than other methods. Hydrogen can also be stored chemically in metal hydrides or chemical compounds like ammonia. While this method streamlines transportation and storage, it necessitates chemical processing to extract the hydrogen for utilization.

Aside from technical storage issues, hydrogen also poses significant safety hazards. Although it is not toxic, it is highly flammable and can form explosive mixtures with air. Due to its low molecular weight and high diffusivity, hydrogen can leak from containers and not be easily detected. Furthermore, hydrogen can cause "hydrogen embrittlement" in some metals, leading to material failure. These conditions make hydrogen very dangerous and expensive to handle. Special training and safety protocols are necessary to prevent accidents.

Hydrogen is typically transported using one of the following methods. High-pressure gas cylinders can be used to transport compressed hydrogen gas in smaller quantities. For larger volumes, hydrogen gas is transported at high pressures in tube trailers. Hydrogen can also be transported in cryogenic liquid tankers, although this method is energy-intensive. For continuous, bulk movement, hydrogen can be transported through pipelines, similar to natural gas. A number of these pipelines already exist and a number of liquid methane pipelines can be repurposed. The European Hydrogen Backbone initiative envisions an increase to 32,616 km of hydrogen pipelines <sup>4</sup>.

### 1.2.3. Consumption

To utilize the energy contained in hydrogen, it is essential to transform its chemical energy into a more practical form. Generally, this transformation is achieved through one of two methods.

#### Hydrogen fuel cell

The most popular method of using hydrogen for power is through fuel cells. Fuel cells are electrochemical devices that convert the chemical energy of a fuel (hydrogen) and an oxidizer (typically oxygen from the air) into electricity through a pair of redox reactions, effectively making it the reverse process of electrolysis. This technology is clean and efficient, with water being the only emission. Fuel cells are used in various applications, from powering electric vehicles to providing backup power for buildings and grid support. Its operation is explained through Figure 1.2.

A fuel cell consists of two electrodes: the anode (negative) and the cathode (positive), and an electrolyte that allows the transfer of ions but not electrons. In a typical hydrogen fuel cell, the process begins at the anode, where hydrogen molecules are introduced. These molecules are split into protons (positive hydrogen ions) and electrons through a process called oxidation. The protons move through the electrolyte towards the cathode, but the electrons are forced to take a different path and travel through an external circuit, thus creating an electric current.

Functionally similar to a battery in generating an electric current, hydrogen fuel cells offer practical benefits like rapid refuelling and higher energy density. However, like batteries, they are somewhat re-

<sup>4</sup><https://ehb.eu/files/downloads/EHB-initiative-to-provide-insights-on-infrastructure-development-by-2030.pdf>

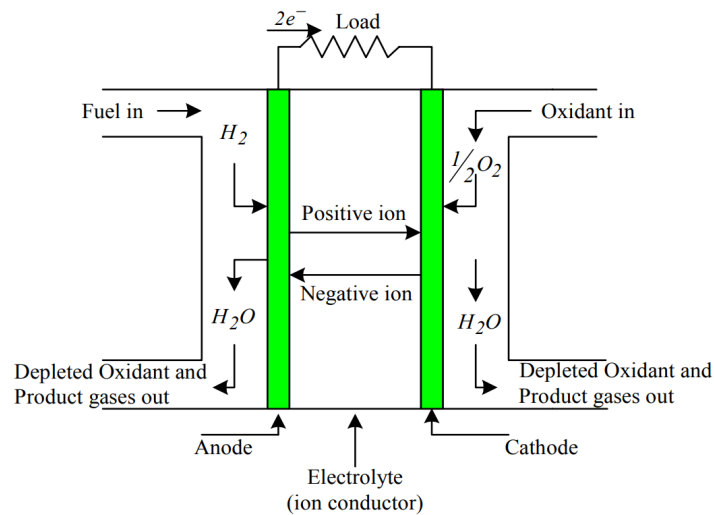


Figure 1.2: Fuel cell operation diagram [15]

stricted in their specific power output, which limits their applications. Examples of lower-power aviation applications are auxiliary power units, ground support equipment and unmanned aerial vehicles [14].

### Hydrogen combustion

Another route that can be taken is through combustion. Although it has lower efficiency compared to fuel cells, it is able to generate power outputs in the range of traditional gas turbines. This is something that is required if it is considered as a serious alternative to kerosene. The workings of a hydrogen-fuelled gas turbine would be conceptually similar to that of a kerosene-based one. It would harvest the chemical energy in the fuel through oxidation with air in order to expand a gas and power the aircraft. However, the current absence of hydrogen-powered commercial aircraft highlights the challenges in its implementation.

## 1.3. Towards a hydrogen combustor

To effectively understand the potential of using hydrogen as a fuel in commercial aviation, it is crucial to first understand how conventional modern combustors operate. This foundational knowledge sets the stage for an exploration of the unique challenges associated with hydrogen combustion in gas turbine engines. The discussion then shifts to an examination of various hydrogen combustors, highlighting their distinctive features and how they are adapted for hydrogen. This analysis leads to the formulation of specific requirements for developing an advanced numerical model tailored for hydrogen combustion, paving the way for more sustainable and efficient aircraft propulsion systems.

### 1.3.1. Conventional gas turbine combustors

Figure 1.3 illustrates a typical modern gas turbine combustor, which commonly employs the Rich-Quench-Lean (RQL) methodology to effectively manage  $\text{NO}_x$  emissions. In this system, combustion is initially established in a primary zone with the aid of a stabilizer, such as a swirler, which is a key component in this process. Here, fuel undergoes combustion in a fuel-rich environment, leading to lower peak temperatures due to the incomplete burning of fuel in the limited available oxygen. This area also plays a vital role in stabilizing the flame during engine start-up and idle settings, when the engine has not yet achieved its optimal operating pressure.

After the primary zone, the hot, fuel-rich mixture progresses to the intermediate or secondary zone, where it undergoes rapid dilution and cooling, effectively 'quenching' the flame. This rapid temperature decrease is a strategic approach to inhibit the formation of significant amounts of  $\text{NO}_x$ , as these emissions predominantly occur at high temperatures.

In the final stage, additional air is introduced in the dilution zone. This stage serves multiple purposes: it compensates for dissociation losses, aids in the oxidation of soot particles, and ensures the combustion of any residual fuel that may have escaped due to suboptimal mixing in earlier stages. The careful orchestration of these zones and processes within the RQL combustor design is crucial for achieving efficient combustion while simultaneously minimizing  $\text{NO}_x$  emissions.

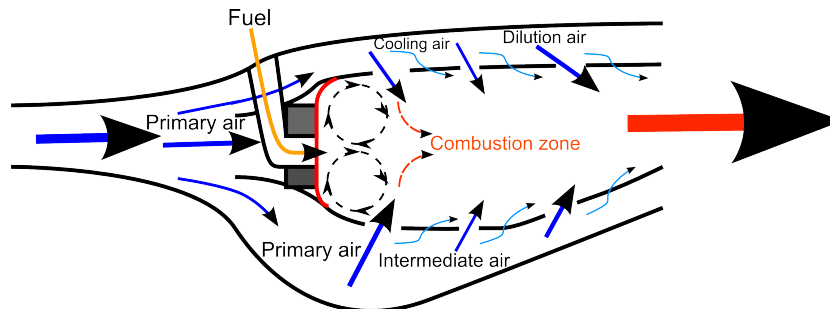


Figure 1.3: Diagram of air flow paths in a gas turbine combustor [16]

### 1.3.2. Challenges for hydrogen combustors

One cannot simply change the fuel to hydrogen in a contemporary aero-engine. Hydrogen has a new set of characteristics and challenges compared to conventional kerosene [17]. A new combustor, therefore, needs to be designed accordingly.

The first important difference compared to hydrocarbon fuels is hydrogen's high reactivity. There are several reasons for this. Hydrogen combustion involves breaking just a single H-H bond in  $\text{H}_2$ , as opposed to methane, which requires the dissociation of four C-H bonds. This simplicity in bond-breaking not only facilitates easier initiation of the reaction but also enhances the formation of radicals, which in turn significantly speeds up the combustion process. Additionally, hydrogen is composed of the smallest and lightest atoms in the periodic table: hydrogen atoms. According to kinetic molecular theory, at a given temperature, lighter molecules have higher average velocities than heavier molecules, such as carbon-based ones. This results in more effective and frequent collisions contributing further to the high reactivity of hydrogen as a fuel.

A second notable contrast between hydrogen and hydrocarbon combustion lies in hydrogen's higher diffusivity. Aside from their higher average velocities due to their lower inertia, the small molecular size of hydrogen molecules makes it easier for them to navigate through intermolecular spaces, effectively giving them a longer mean free path. Furthermore, hydrogen is subject to relatively weak intermolecular forces. Being nonpolar, hydrogen molecules only experience London dispersion forces, the weakest of the van der Waals forces. London dispersion forces are caused by temporary dipoles due to random fluctuations in the electron distribution around the molecule. In contrast, methane, though also nonpolar, has larger molecules with more electrons. This results in stronger London dispersion forces, leading to more significant molecular attraction and, consequently, lower diffusivity compared to hydrogen.

This disparity in diffusivity between hydrogen and hydrocarbon is further reflected in the Lewis number, a dimensionless quantity representing the ratio of thermal diffusivity to mass diffusivity. In the combustion of hydrocarbons, the Lewis number for all species is typically around one, leading to the common assumption of a unity Lewis number in computational models. This means that the molecular diffusivities of all species and the thermal diffusivity are more or less equal. However, the Lewis number for hydrogen is approximately 0.3, making this assumption unsuitable for modelling hydrogen-air combustion. This divergence has two primary consequences. Firstly, because the Lewis number for hydrogen is significantly less than one, the rate of thermal diffusion is slower compared to the rate of molecular diffusion for the fuel. This results in localized variations in enthalpy, which subsequently affect temperature and, by extension, influence the mass burning rate and chemical reaction rates. Secondly, the discrepancy in Lewis numbers leads to what is known as differential diffusion, where different components within a mixture spread at varying rates. When one or more species, like hydrogen, diffuse more quickly than the rest of the mixture, this specific phenomenon is termed preferential diffusion. This leads to differences in mass fractions when compared to the case where diffusivities are assumed to be equal in the mixture. The effects are important to analyse as it can lead to higher flame speeds and temperatures.

The combination of hydrogen's high reactivity and diffusivity results in higher flame speeds compared to hydrocarbons. The (unstretched) laminar flame speed is typically defined as the propagation rate of the normal flame front relative to the unburned mixture [18]. It is a key metric in the design of the combustor as it has consequences regarding residence time and the risk of flashbacks. Hydrogen's laminar flame speed can be more than 12 times higher than methane in some cases [19]. In adapting combustor designs to accommodate hydrogen's unique properties, engineers must consider various factors, including the shape and size of the combustion chamber, the flow dynamics of the fuel and air mixture, and the implementation of effective flame arrestors or other safety mechanisms. The goal is to harness the advantages of hydrogen's high flame speed while mitigating the potential risks it poses, ensuring both efficient and safe operation.

Another consequence of hydrogen's high diffusivity is that the complex diffusive properties may lead to thermo-diffusive instabilities. The concept of flame stretch, which is the measure of how quickly the flame surface area changes relative to the area itself, plays a significant role in determining flame speed, as governed by the Markstein length. Negative Markstein lengths cause an increase in flame speeds with increased stretch, leading to the formation of uneven, wrinkled flame fronts. These irregular fronts enhance flame speeds and amplify variations in local reaction rates. Stretching the flame makes the flame front narrower, intensifying concentration gradients and thereby increasing molecular diffusion. In scenarios where the Lewis number is less than one, molecular diffusion surpasses thermal diffusion, causing the stretched flame speed of hydrogen to rise and further augment the instabilities. Understanding and managing the implications of hydrogen's negative Markstein lengths is crucial in designing safe and efficient hydrogen combustion systems. It necessitates careful consideration of factors like combustion chamber geometry, flame holder design, and operating conditions to ensure stable combustion and prevent flashback or blow-off. The effects of thermo-diffusive instabilities have to be taken into account in premixed combustion but play a relatively minor role in partially premixed flames.

A fifth difference is hydrogen's higher flame temperature. It is caused by the combination of a high LHV and reactivity. It has implications for the structural integrity of the combustor, but also for  $\text{NO}_x$  production. The thermal pathway is highly sensitive to the flame temperature. A higher flame temperature means more  $\text{NO}_x$  production. So although no carbon-based pollutants are formed in hydrogen combustion,

special attention should be given to  $\text{NO}_x$  production through mitigation solutions. One such mitigation technique is lean-burn technology. Burning fuel with an excess amount of oxidiser lowers the flame temperature compared to stoichiometric conditions. The high lower-heating-value and reactivity of hydrogen allow it to be operated at very lean conditions without having lean blow-off. Several studies have shown this effect [20][21][22]. To use this technology in an aircraft engine, a model is needed that captures these important differences and can handle the conditions typically seen in a gas turbine combustor.

### 1.3.3. Hydrogen combustion designs

Although no commercial aircraft are using hydrogen combustion, there have been several academic proposals for hydrogen combustors.

#### Lean direct injection

An alternative to the RQL concept is Lean Direct Injection (LDI) [23][24]. In this approach, the fuel and air are directly injected into the combustion zone with an equivalence ratio close to lean blowout. This simplifies the combustor design as all air enters in the front and there is no need for staged combustion. This strategy is increasingly being adopted in newer aircraft engine designs. However, for hydrogen combustion, it has increased benefits due to the explicit control over the mixture ratio. This allows for more control over the flame temperature and speed. Hydrogen's fast burning velocity and diffusivity make it well-suited for the LDI approach, which relies on the direct and efficient mixing of fuel and air. This can lead to more complete combustion, improving the overall efficiency of the engine.

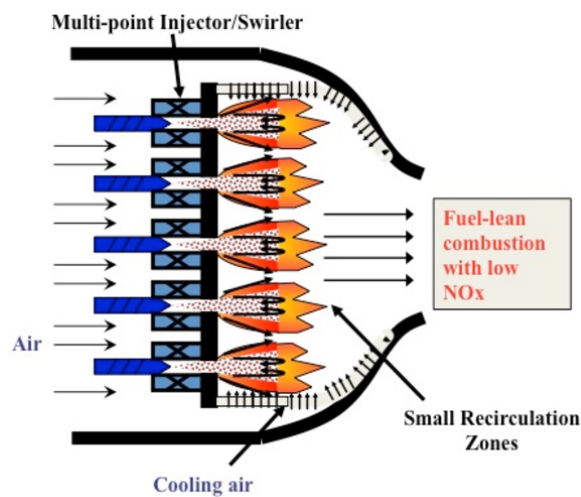


Figure 1.4: LDI concept [25]

#### Micro-mixing concept

Micro-mixing involves the rapid and thorough mixing of hydrogen fuel with air. This is crucial because hydrogen has a high diffusivity and a wide flammability range compared to hydrocarbons. Rapid mixing ensures a more uniform fuel-air mixture, reducing the likelihood of hot spots and high-temperature regions that can lead to the formation of  $\text{NO}_x$ . By finely controlling the mixing process at a micro-scale, the combustion can be made more uniform and complete. This not only improves the efficiency of the combustion process but also minimizes the formation of pollutants [26].

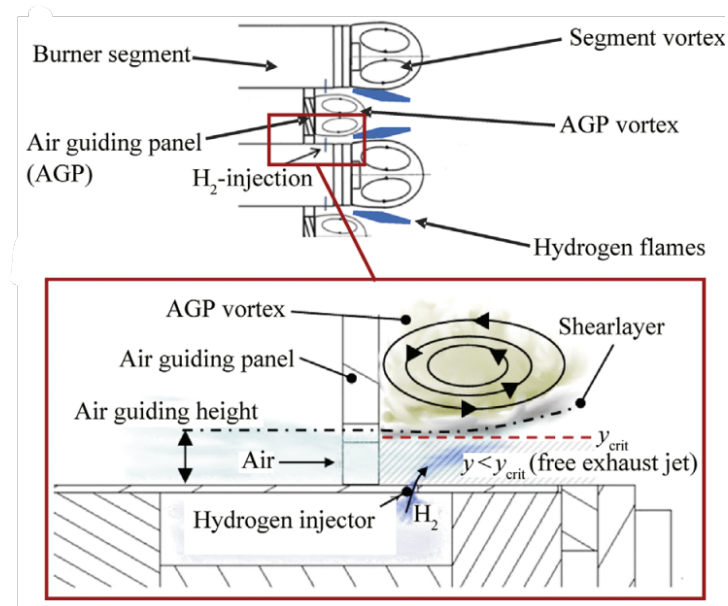


Figure 1.5: Micro-mixing concept diagram [27]

#### Swirl stabilised with axial injection

A traditional lean premixed swirl-stabilised burner poses significant risks of flashback due to hydrogen's high flame speed. A key design criterion in nozzle aerodynamics to prevent flashbacks is that the axial velocity must be as high and as uniform as possible, free of any strong wakes [28]. The introduction of a non-swirling air jet along the central axis of the radial swirl generator helps to meet this criterion. This design choice effectively increases the axial velocity along the rotation axis. As a result, the vortex breakdown is shifted further away from the mixing tube's exit, significantly reducing the risk of flashback in the combustion process [29]. The control over the axial velocity has the additional advantage of being able to be used on different types of fuel, e.g. hydrogen and methane [30]. The Advanced Propulsion and Power Unit (APPU) project at the TU Delft is using this technology as a way to offer the flexibility to operate on either kerosene or hydrogen, depending on the local fuel availability.

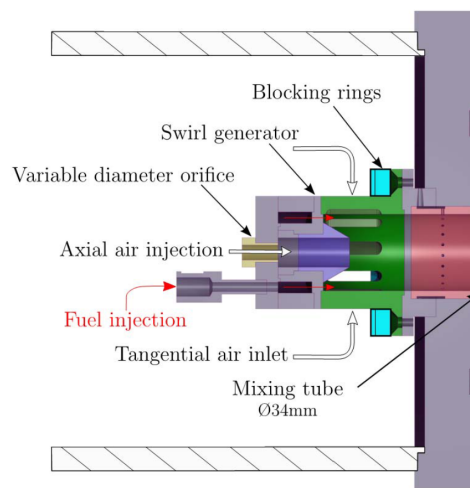


Figure 1.6: Schematic of swirl stabilised burner with axial injection [29]

#### 1.3.4. Hydrogen combustion model requirements

Determining the optimal design for a hydrogen combustor remains a subject of ongoing exploration. The process of constructing and experimenting with various designs is crucial, as it yields valuable real-

world insights into the performance and resilience of materials, components, and systems under diverse operational conditions. However, the feasibility of physically building every design is constrained by factors such as cost and time.

To address this, numerical modelling serves as a powerful tool for engineers. It enables the prediction of a combustor design's performance prior to the construction of a physical prototype. Through modelling, engineers can rapidly iterate and refine design concepts. They have the capability to adjust virtual parameters, including the combustor's geometry, flow rates, and fuel-air mixing mechanisms, and promptly evaluate the resulting impacts. Furthermore, numerical models are instrumental in deciphering complex phenomena inherent in combustion processes. They provide a detailed understanding of intricate chemical reactions and physical processes, aspects that might be challenging or impractical to directly observe in experimental setups.

An effective model tailored for developing a practical hydrogen aircraft engine must fulfil several key criteria, given the uncertainty surrounding the most suitable operational regimes. It must be versatile enough to efficiently operate across a broad spectrum of regimes, encompassing both premixed and non-premixed scenarios. Additionally, the model should be adept at handling fully turbulent conditions, which are characteristic of combustor environments.

Crucially, the model must accurately represent the unique attributes of hydrogen combustion. This includes addressing challenges like differential diffusion and the high flame speeds associated with hydrogen. Furthermore, the model should be flexible enough to facilitate in-depth exploration of various phenomena relevant to hydrogen combustion. These include the implementation of lean-burn technology, the mechanisms of  $\text{NO}_x$  formation, and the effects of high strain rates.

Achieving this comprehensive functionality while maintaining reasonable computational costs is essential. This balance ensures that the model is not only thorough in its analytical capabilities but also practical and accessible for ongoing research and development in hydrogen aircraft engine technology.

The goal of this thesis is to develop and test a model that meets these requirements. Chapter 2 lays the foundational theoretical groundwork on numerical flow theory, encompassing both non-reactive and reactive flows while exploring various numerical solution algorithms. This chapter acts as a primer, leading into the specialized literature on Large Eddy Simulation (LES) for combustion, which predominantly concentrates on the description of the chemical kinetics and the modelling of subgrid-scale flame-turbulence interactions. In Chapter 3, these topics are examined, along with an analysis of several notable experiments focusing on hydrogen-air combustion within the specific framework of aircraft combustors. This chapter concludes by justifying the adoption of an FGM-ESF (Flamelet Generated Manifold - Eulerian Stochastic Field) model for this study. Chapter 4 consists of a standalone document that presents the methodology and findings of this research in the format of an academic paper. The thesis concludes in Chapter 5, which synthesizes the key conclusions drawn from the research and outlines recommendations for future studies in this field.

# 2

## Theoretical background

Turbulent combustion modelling is a field that encompasses a wide array of physical and chemical processes. The complexity comes from the interaction between turbulence and chemical reactions, which are pivotal in determining the efficiency, stability, and emissions of combustion systems. This theoretical background starts by focusing on the non-reactive aspect. The key governing equations are explained and methodologies, such as Direct Numerical Simulation and Large Eddy Simulation are introduced. After that a transition is made to reactive flows, addressing the complexities introduced by chemical reactions in turbulent media. Serving as a foundational precursor, this background bridges the gap to the combustion literature review, which assumed a fundamental level of understanding on LES for reactive flows.

### 2.1. Non-reactive flows

This chapter provides a theoretical background on non-reactive flows. It is inspired by one of the most influential works in turbulent flow dynamics: Pope's *Turbulent Flows* [31].

#### 2.1.1. Governing equations of non-reactive flows

The flow field in fluid dynamics can be described in one of two ways. The Eulerian description focuses on specific locations in space, observing how fluid properties change over time at these fixed points. An analogy for this framework is watching a river flow past a fixed point on a bridge. The changing characteristics of the water (like velocity and pressure) are observed at this point. On the other hand, the Lagrangian description follows individual fluid particles as they move through space and time. This is similar to tracking a leaf floating down the river, noting its velocity, position, and other properties as it travels. Both approaches have their advantages and are used depending on the context of the problem. The Eulerian description is most popular as it is more practical for problems involving flow fields where tracking every particle is not feasible. It is particularly useful in engineering applications like aerodynamics or hydrodynamics, where the focus is on the effects of fluid flows on objects or over regions. However, the Lagrangian description, while computationally more intensive, can be useful in some instances where there is a need for a deeper understanding of the detailed motion of particles in a fluid. Advanced computational fluid dynamics (CFD) techniques can employ both Eulerian and Lagrangian methods to simulate complex fluid flows that can not fully be captured by one framework. An example of this is the Lagrangian Monte Carlo approach which is discussed later.

The governing equations for non-reacting flows are only defined in the Eulerian framework for this theoretical background. The governing equations for non-reacting flows are based on two conservation equations: mass and momentum. For an infinitesimal control volume, the mass-conservation or continuity equation in tensor notation is

$$\frac{\partial \rho}{\partial t} + \frac{\partial \rho u_i}{\partial x_i} = 0, \quad (2.1)$$

where  $\rho$  is density and  $u_i$  the  $i$ th velocity component.  $t$  represents time and  $x_i$  spatial location. The equation only exists of two terms: a local rate of change in density and a convective term.

The momentum conservation equation applies the principles of Newton's second law to fluid motion. It states that the rate of change of momentum of a fluid element is equal to the sum of the forces applied to it. This equation is fundamentally a statement about forces: those that arise from pressure variations within the fluid, those that are due to viscous stresses, and those that are exerted by external fields, such as gravity. The general momentum-conservation equation is given by

$$\frac{\partial \rho u_i}{\partial t} + \frac{\partial \rho u_i u_j}{\partial x_j} = \frac{\partial \tau_{ij}}{\partial x_j} - \frac{\partial p}{\partial x_i} + \rho f_i, \quad (2.2)$$

where  $\tau_{ij}$  is the stress tensor,  $p$  is the pressure, and  $f_i$  is the sum of external body forces, e.g. gravity or magnetism.  $f_i$  is assumed to be zero for the rest of the work. The stress tensor is an important concept in this equation. It represents internal forces within the fluid due to its motion and molecular interactions.

For constant-property Newtonian fluids, where the stress is linearly proportional to the strain rates, the stress tensor simplifies the relationship between the viscous forces and the velocity gradients of the fluid as

$$\tau_{ij} = \mu \left( \frac{\partial u_i}{\partial x_j} + \frac{\partial u_j}{\partial x_i} \right) - \frac{2}{3} \mu \left( \frac{\partial u_k}{\partial x_k} \right) \delta_{ij}, \quad (2.3)$$

where  $\mu$  is the dynamic viscosity and  $\delta_{ij}$  the Kronecker delta function defined as

$$\delta_{ij} = \begin{cases} 0, & \text{if } i \neq j. \\ 1 & \text{if } i = j \end{cases} \quad (2.4)$$

Using this expression in combination with general momentum conservation equations yields the Navier-Stokes equations.

An important dimensionless quantity that can be introduced now is the Reynolds number. It represents the balance between inertial and viscous forces in the flow and is defined as:

$$\text{Re} = \frac{\rho U L}{\mu}, \quad (2.5)$$

where  $U$  and  $L$  are characteristic velocity and length scales respectively. The Reynolds number helps characterise the nature of the flow, whether it is laminar or turbulent. The higher the number, the more turbulent the flow is.

The mass-conservation and Navier-Stokes equations are the foundation upon which computational models of fluid flow are built. They allow engineers and scientists to simulate and predict fluid behaviour practically under a wide range of conditions, forming the basis of computational fluid dynamics (CFD) simulations. There are, however, multiple approaches to solving these equations, two of the most important ones are discussed next.

## 2.1.2. Direct Numerical Simulation

Direct Numerical Simulation (DNS) involves solving the Navier-Stokes equations to capture all motion scales in fluid dynamics. Appropriate initial and boundary conditions are set up for specific flows, where each simulation produces a single realization of the flow. Initially infeasible until the 1970s due to computational limitations, DNS now offers unparalleled accuracy and detail in modelling. However, its application is limited to only low and moderate Reynolds number flows due to its high computation costs. The following analysis explains where this steep increase in Reynolds number comes from.

A conceptual flow that is often studied with DNS is homogeneous turbulence. It refers to turbulence in which statistical properties are uniform in space. In such turbulence, statistical characteristics remain constant across different points in a specific direction. This uniformity simplifies analysis and simulation, as it allows the use of periodic boundary conditions and Fourier transforms in computational methods. Homogeneous turbulence is often studied to understand fundamental aspects of turbulence without the complexity of inhomogeneous effects, like those introduced by walls or varying fluid properties. It serves as a model for more complex turbulent flows. The most popular methods for homogeneous turbulence are the so-called *pseudo-spectral* methods.

The domain of homogeneous turbulence is typically a cube with side  $\mathcal{L}$ . The velocity field  $\mathbf{u}(\mathbf{x}, t)$  is represented as a finite Fourier series as

$$\mathbf{u}(\mathbf{x}, t) = \sum_{\boldsymbol{\kappa}} e^{i\boldsymbol{\kappa}\cdot\mathbf{x}} \hat{\mathbf{u}}(\boldsymbol{\kappa}, t), \quad (2.6)$$

where  $\boldsymbol{\kappa}$  is the wavenumber. The size of the simulation is determined by  $N$ , which refers to the number of Fourier modes, or grid points, used in per dimension. The total number of modes is thus given by  $N^3$ . The largest wavenumber represented in the finite Fourier series is related to  $N$  as

$$\kappa_{\max} = \frac{\pi N}{\mathcal{L}} \quad (2.7)$$

The dimensions of the cube should be sufficiently large to encompass the motions that contain most of the energy and the spacing between grid points needs to be adequately small to accurately capture the smaller scales where energy dissipation occurs. This gives rise to two spatial resolution requirements based on two length scales.

The integral length scale is a measure of the largest eddies in turbulent flow and is associated with the largest structures in the turbulence, where most of the energy is contained. It represents the size of the dominant, energy-containing eddies and sets the scale for the large-scale motions of the flow. To capture the dynamics of these large eddies accurately, the computational domain must be large enough to encompass several integral length scales. This ensures that the energy-containing motions are fully represented within the simulation. Pope [31] sets a lower limit on  $\mathcal{L}$  at eight integral length scales.

The Kolmogorov length scale  $\eta$  represents the smallest scales where the kinetic energy of the turbulent eddies is dissipated into heat due to the viscosity of the fluid. However, the dissipation is already very small beyond  $\kappa\eta = 1.5$ . Therefore,  $\kappa_{\max}\eta \geq 1.5$  is a good resolution requirement for DNS [32]. The relation between these quantities determines the number of modes  $N$ . As the turbulence in the flow increases, the distance between these scales widens. This requires a greater number of modes for accurate representation. It can be related to the Reynolds number as

$$N^3 \sim 4.4 \text{Re}_L^{9/4}. \quad (2.8)$$

For the exact derivation, the reader is referred to the Pope's book.

In CFD methods, the time resolution is inherently linked to spatial resolution. A particle can only move a fraction of the grid spacing  $\Delta x$  per time step  $\Delta t$  to guarantee stability and accuracy. The Courant number is typically used to represent this relation as

$$Co = \Delta t \left( \sum_{i=1}^n \frac{u_i}{\Delta x_i} \right) \quad (2.9)$$

Through this number, an estimation of the required number of timesteps in terms of the Reynolds number can be obtained. The number of mode-steps, therefore, rises very steeply with Reynolds number.

$$N^3 M \sim 160 \text{Re}_L^3 \quad (2.10)$$

To conclude, Pope produces a table estimating the required computational times for different Reynolds numbers.

**Table 2.1:** Estimates, for DNS of isotropic turbulence at various Reynolds numbers, of modes required in each direction,  $N$ ; total number of modes,  $N^3$ ; number of time steps,  $M$ ; number of mode-steps,  $N^3 M$ ; and the time to perform a simulation at 1 gigaflop (assuming 1,000 operations per mode per step)

$Re_L$	$N$	$N^3$	$M$	$N^3 M$	CPU Time
94	104	$1.1 \times 10^6$	$1.2 \times 10^3$	$1.3 \times 10^9$	20 min
375	214	$1.0 \times 10^7$	$3.3 \times 10^3$	$3.2 \times 10^{10}$	9 h
1,500	498	$1.2 \times 10^8$	$9.2 \times 10^3$	$1.1 \times 10^{12}$	13 days
6,000	1,260	$2.0 \times 10^9$	$2.6 \times 10^4$	$5.2 \times 10^{13}$	20 months
24,000	3,360	$3.8 \times 10^{10}$	$7.4 \times 10^4$	$2.8 \times 10^{15}$	90 years
96,000	9,218	$7.8 \times 10^{11}$	$2.1 \times 10^5$	$1.6 \times 10^{17}$	5,000 years

Although computational power has significantly increased since the publication of the book, it shows how DNS, even for a simple flow, already has very expensive computational requirements. When moving towards more complicated cases like wall-bounded or reactive flows, these only become bigger. Therefore, it can be concluded that even though DNS is a powerful research tool for studying the fundamental aspects of turbulence and fluid mechanics, it is limited to relatively simple geometries and low to moderate Reynolds numbers. A different CFD method is required for analysing highly turbulent flows like a hydrogen combustor.

### 2.1.3. Large Eddy Simulation

Solving the Navier-Stokes equations directly is too computationally prohibitive for turbulent flows. A way to reduce costs is choosing to only resolve the largest scales of turbulence, i.e. the largest eddies, and model the others. This strategy is called Large Eddy Simulation (LES). The idea relies on concepts of the energy cascade and scale separation.

To illustrate these concepts, consider the energy spectrum for homogeneous isotropic turbulence in Figure 2.1. It was conceived by calculating the 3-D kinetic energy density (using Equation 2.11) for different wavenumbers using DNS data.

$$E(\kappa_n = \kappa_0 n) = \sum_{\kappa_0(n-\frac{1}{2}) \leq |\kappa| < \kappa_0(n+\frac{1}{2})} \frac{1}{2} \hat{\mathbf{u}}(\kappa) \cdot \hat{\mathbf{u}}^*(\kappa) \quad (2.11)$$

In turbulent flows, energy is produced at large scales, often due to velocity or directional differences between fluid layers, occurring primarily in the energy-containing subrange. These large eddies are shaped by flow boundary conditions and geometry. The energy then cascades to smaller scales predominantly through inertial forces, with minimal influence from viscosity, in the inertial subrange. At the smaller scales, in the dissipation range, energy dissipates as heat due to viscosity. Kolmogorov's theory states that at high Reynolds numbers, small-scale turbulent motions tend to be statistically isotropic. This makes them relatively easy to model.

Note that there is a reverse process called backscatter, where energy moves from smaller to larger scales. However, in most flows, this effect is rather limited.

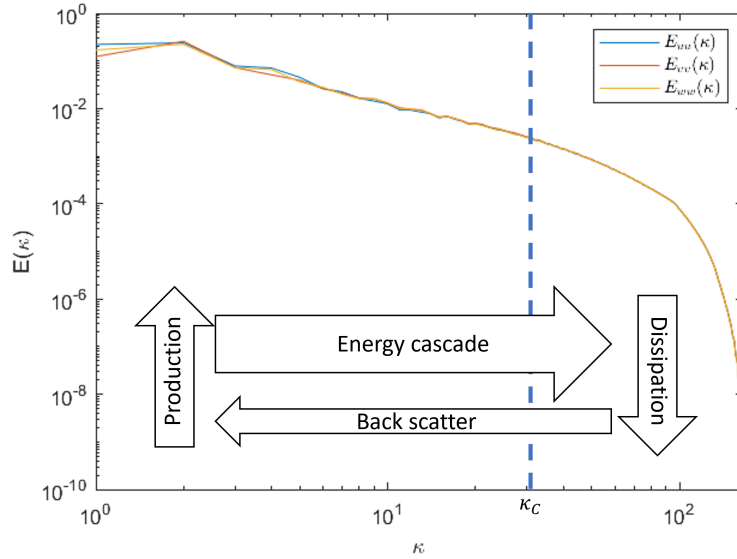


**Figure 2.1:** Energy spectrum for homogenous isotropic turbulence. DNS data provided by Stefan Hickel.

Thus, the large scales in a flow carry most of the kinetic energy and have a strong effect on the macrostructure of a flow, while the smallest scales are mainly responsible for the dissipation of energy and are more predictable. Large Eddy Simulation separates these scales and directly resolves the large-scale eddies while modelling only the effects of the smaller scales. This operation is done by some form of filtering.

Executing an LES consists of four conceptual steps:

1. A filtering operation is defined to decompose  $\mathbf{u}(\mathbf{x}, t)$  in a resolved, or filtered component  $\mathbf{u}(\mathbf{x}, t)$  and a subgrid-scale, or residual component  $\mathbf{u}'(\mathbf{x}, t)$
2. The filtering operation is applied to the Navier-Stokes equations, which resulted in the filtered model equations
3. A closure model is selected for the residual stress tensor, the so-called SGS stress model
4. The filtered equations are solved numerically

This theoretical background focuses on the first three steps as the fourth steps is discussed in detail in chapter 4.

### Filtering operation

For LES, a low-pass filter is applied which only retains the larger scales. This filtered velocity field can be resolved on a relatively coarse grid. The required spatial resolution of the grid is related to filter width  $\Delta$ . The general filtering operation in physical space for a variable  $q$  is given by

$$\bar{q}(x) = \int q(x') \mathcal{G}(x - x') dx'. \quad (2.12)$$

The residual, or subgrid-scale field for  $q$  is given by  $q' = q - \bar{q}$ .

Each filter has a representation in both physical and spectral space. Consider the Fourier transform of  $q$ :

$$\hat{q}(\kappa) \equiv \mathcal{F}\{q(x)\}. \quad (2.13)$$

The filtering operation in spectral space is then defined as

$$\begin{aligned}\hat{q}(\kappa) &\equiv \mathcal{F}\{\bar{q}(x)\} \\ &= \hat{G}(\kappa)\hat{q}(\kappa).\end{aligned}\tag{2.14}$$

There are a number of filters possible, but three of them are most popular.

The most explicit separation of scales is the sharp spectral(-cutoff) filter. It is given in its spectral representation by

$$\hat{G}(\kappa) = \begin{cases} 1 & , |\kappa| \leq \kappa_C \\ 0 & , |\kappa| > \kappa_C \end{cases}\tag{2.15}$$

It sets all wavenumber higher than the cut-off wavenumber  $\kappa_C$  to zero. Its representation in physical space is given by

$$G(x) = \frac{\sin(\kappa_C x)}{\kappa_C x} = \frac{\Delta_C}{\pi x} \sin\left(\frac{\pi x}{\Delta_C}\right)\tag{2.16}$$

Although conceptually very simple, implementing a sharp spectral cutoff filter in physical space can be challenging. This is particularly true in cases where a transformation between physical and spectral space is not straightforward. Therefore, they are more suited for simple, homogeneous, and isotropic turbulence. They are less effective in flows with complex geometries or inhomogeneous conditions, where the turbulence characteristics vary significantly in space.

A more practical filter is the box or top-hat filter. This filter acts by averaging the variable over a certain spatial extent. This extent is typically related to the grid size in numerical simulations. The filter effectively smooths out the flow field by averaging over this predefined 'box'. Its physical representation is given by

$$G(x) = \begin{cases} \frac{1}{\Delta_C} & , |x| \leq \frac{\Delta_C}{2} \\ 0 & , |x| > \frac{\Delta_C}{2} \end{cases}\tag{2.17}$$

A big advantage, compared to the previous filter, is that it only requires information in its immediate neighbourhood. This property makes it easier to implement in various numerical schemes and computational grids. This ease of implementation is particularly useful in complex simulations involving intricate geometries or boundary conditions, making it the preferred filter in practical LES cases.

The third filter is the Gaussian filter. Unlike the previous two filters, it keeps its Gaussian shape in both the physical as the spectral representation. The physical is given by

$$\hat{G}(\kappa) = \exp\left(-\frac{\Delta_C^2 \kappa^2}{24}\right) = \exp\left(-\frac{\pi^2 \kappa^2}{24 \kappa_C^2}\right),\tag{2.18}$$

and the spectral by

$$G(x) = \sqrt{\frac{6}{\pi \Delta_C^2}} \exp\left(-\frac{6x^2}{\Delta_C^2}\right).\tag{2.19}$$

The Gaussian filter is infinitely smooth, which reduces the numerical artefacts (e.g. discretisation or rounding errors) in simulations, making it a good choice for high-accuracy applications. The filter's properties are also often considered to be more physically realistic for simulating turbulent flows, as they provide a more natural separation of scales. However, because of its non-local nature, the Gaussian filter can be more computationally intensive than local filters like the top-hat filter. The choice of the Gaussian filter is often a balance between the need for physical realism and computational feasibility.

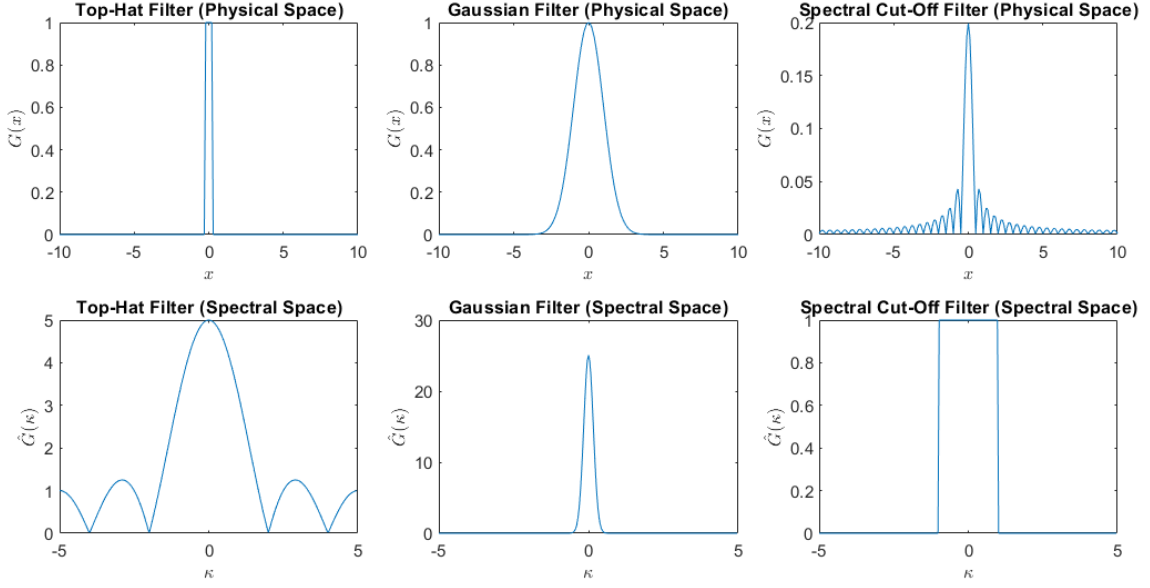


Figure 2.2: Different filters in physical and spectral representation

### Filtered conservation equations

After the filtering operation has been defined, it can be applied to Navier Stokes equation. This yields the following set of equations:

- Conservation of mass:

$$\frac{\partial \bar{\rho}}{\partial t} + \frac{\partial \bar{\rho} \bar{u}_i}{\partial x_i} = 0 \quad (2.20)$$

- Conservation of momentum:

$$\frac{\partial \bar{\rho} u_i}{\partial t} + \frac{\partial \bar{\rho} \bar{u}_i \bar{u}_j}{\partial x_i} = -\frac{\partial \bar{p}}{\partial x_i} + \frac{\partial}{\partial x_i} \left( \bar{\tau}_{ij} - \bar{\rho} \underbrace{(\bar{u}_i \bar{u}_j - \bar{u}_i \bar{u}_j)}_{(u.1)} \right) \quad (2.21)$$

$$\bar{\tau}_{ij} = 2\bar{\mu} \left( \tilde{S}_{ij} - \frac{1}{3} \delta_{ij} \tilde{S}_{kk} \right) \quad (2.22)$$

$$\tilde{S}_{ij} = \frac{1}{2} \left( \frac{\partial \tilde{u}_i}{\partial x_j} + \frac{\partial \tilde{u}_j}{\partial x_i} \right) \quad (2.23)$$

This leads, however, to an unclosed term. The term is referred to as the SGS stress tensor. Closure of the term requires a subgrid scale stress model.

### Subgrid scale stress models

The SubGrid Scale (SGS) stress tensor  $\tau_{sgs,ij}$  represents the effects of unresolved fluid motions and is essential in every LES. A particularly popular type of model in the literature is the Eddy Viscosity Model (EVM). These types of models represent the SGS tensor as

$$-\bar{\rho} (\bar{u}_i \bar{u}_j - \tilde{u}_i \tilde{u}_j) = -\tau_{sgs,ij} = 2\mu_{sgs} \left( \tilde{S}_{ij} - \frac{1}{3} \delta_{ij} \tilde{S}_{kk} \right), \quad (2.24)$$

where  $\mu_{sgs}$  is called the eddy viscosity. It rests on the Boussinesq assumption which states that the dissipativity of the kinetic energy in the flow can be modelled by a viscosity term, similar to the molecular motion in a gas that can be described by a molecular viscosity term. There are multiple ways to model  $\mu_{sgs}$ . In this work, the algebraic and transported eddy-viscosity models are treated.

Aside from EVMs, there are also the so-called structural models, such as the Bardina Scale Similarity model [33]. They take a more theoretical approach to modelling the SGS stress tensor and have a better correlation with the exact SGS stress tensor obtained from DNS data. However, they tend to not work that well in practice and often provide insufficient dissipation. This is especially unstable in reactive flows. That is why they are rarely used in combustion literature and why they are not considered in this theoretical background.

#### 2.1.4. Eddy-viscosity models

EVMs can be broadly classified into two categories: Algebraic Eddy-Viscosity Models (A-EVMs) and Transported Eddy-Viscosity Models (T-EVMs). A-EVMs calculate  $\mu_{sgs}$  using an algebraic relationship that does not require solving additional transport equations. The general form of an algebraic eddy-viscosity model is:

$$\mu_{sgs} = \bar{\rho}(C_m\Delta)^2\mathcal{D}_m(\mathbf{u}), \quad (2.25)$$

where  $C_m$  is a model constant,  $\Delta$  is the filter width, which is typically the cube root of the cell volume, and  $\mathcal{D}_m$  a differential operator of the velocity field  $\mathbf{u}$ .

In contrast to A-EVMs, T-EVMs involve solving one or more additional transport equations to determine the eddy viscosity. These models are more sophisticated and can adapt to local flow conditions, making them suitable for complex flows where turbulence varies significantly in space and/or time.

##### (Dynamic) Smagorinsky model

The first LES model was proposed by Smagorinsky in 1963 [34] and is an A-EVM. It models the eddy viscosity in proportion to the magnitude of the filtered strain-rate tensor  $\bar{S}_{ij}$ . It is given by

$$\mu_{sgs} = \bar{\rho}(C_S\Delta)^2\sqrt{2\bar{S}_{ij}\bar{S}_{ij}}. \quad (2.26)$$

$C_S$  is a model constant which is approximately 0.17 for homogeneous isotropic turbulence [35], but can differ for different types of flows.

The Smagorinsky model is a very simple and efficient model and is therefore widely used, even though it is known to be a too dissipative model. However, its model SGS stresses have poor correlations with the exact SGS stresses and requires ad-hoc fixes for wall boundary layers, such as van Driest damping.

An improvement of this model was proposed by Germano et al. (1991) [36] through a dynamic procedure in which the Smagorinsky constant  $C_S$  is determined based on the knowledge of the resolved scales. This procedure was further improved by Lilly (1992) [37] by using a least-square optimisation on an over-determined problem. It has been widely used for combustion set-ups [38][39][40][41][42][43][44][45][46].

##### $k$ -Equation transported eddy-viscosity model

An alternative approach to modelling eddy viscosity, rather than using an algebraic expression, is to solve an extra transport equation for the SGS kinetic energy  $k_{sgs}$ . This method offers a more dynamic representation of turbulence characteristics.

A notable criticism of the Smagorinsky model is that an assumption of local equilibrium between the subgrid-scale energy production and dissipation rate is made. This means that some non-local and history effects are completely neglected. The one-equation model for the subgrid-scale kinetic energy proposed by Kim and Menon (1995) [47] does not make this assumption. Instead, the SGS tensor is modelled as

$$-\tau_{sgs,ij} = 2\mu_{sgs}\left(\bar{S}_{ij} - \frac{1}{3}\delta_{ij}k_{sgs}\right) \quad (2.27)$$

where the eddy-viscosity is given by

$$\mu_{sgs} = \bar{\rho} (C_k \Delta) \sqrt{k_{sgs}}. \quad (2.28)$$

$k_{sgs}$  is transported as

$$\frac{\partial k_{sgs}}{\partial t} + \bar{u}_i \frac{\partial k_{sgs}}{\partial x_i} = -\tau_{ij} \frac{\partial \bar{u}_i}{\partial x_j} - \varepsilon + \frac{\partial}{\partial x_i} \left( \frac{\mu_{sgs}}{\rho} \frac{\partial k_{sgs}}{\partial x_i} \right), \quad (2.29)$$

and the model is closed with

$$\varepsilon = C_\varepsilon \frac{\sqrt{k_{sgs}}}{\Delta}. \quad (2.30)$$

A dynamic procedure similar to that of the Smagorinsky model can be used to determine  $C_K$  and  $C_\varepsilon$ . This dynamic adjustment allows the model to adapt to varying flow conditions, enhancing its accuracy and applicability to a wider range of turbulent flows. This approach presents a more refined and adaptable framework for turbulence modelling, particularly in scenarios where the assumptions of local equilibrium are not valid.

#### WALE model

The Smagorinsky model, while foundational in turbulence modelling, also suffers from several other drawbacks [48]. Firstly, it only relates the eddy viscosity to the local strain rate and not the rotational rate. However, from DNS results on isotropic turbulence, it is shown that energy is concentrated in the streams, while energy dissipation is concentrated in eddies and convergence zones. Thus, in regions where vorticity dominates irrotational strain, the classical Smagorinsky model tends to be inadequate. This limitation becomes particularly relevant in applications like conventional aero-engine combustors, where swirl is a key component used to stabilize the flame. In such scenarios, the ability to accurately model the effects of vorticity and rotational flow structures is crucial.

A second drawback of the original Smagorinsky model is its scaling near walls. Near walls,  $\mu_{sgs}$  should be zero as all turbulent fluctuations are damped. However, the Smagorinsky model assigns a positive value to it if a velocity gradient exists. Van Driest damping mitigates this problem but is also an ad hoc solution as it is based on the distance to the wall, which can be difficult to determine in complex geometries, like combustors. Furthermore, it scales  $\mu_{sgs} = O(y^2)$ , instead of the proper  $\mu_{sgs} = O(y^3)$  near walls.

The third complication comes from the dynamic procedure for which a test filter is required. Typically a test filter width of  $2\Delta$  is used for this procedure. However, this may become an issue for complex geometries.

To address all of these issues, Nicoud and Ducros have proposed a new A-EVM called the Wall-Adapting Local Eddy viscosity (WALE) model. The WALE model includes both the local strain and rotation rates, goes naturally to zero in the vicinity of a wall with the proper order of magnitude, and requires no dynamic procedure [48].

The idea is to consider the traceless symmetric part of the square of the velocity gradient tensor:

$$s_{ij}^d = \frac{1}{2} (\tilde{g}_{ij} + \tilde{g}_{ji}) - \frac{1}{3} \delta_{ij} \tilde{g}_{kk}^2 \quad (2.31)$$

$$\tilde{g}_{ij} = \frac{\partial \tilde{u}_j}{\partial x_i} \quad (2.32)$$

An LES model based on  $s_{ij}^d s_{ij}^d$  detects turbulent structures with both strain and rotation rates. The eddy viscosity is calculated with

$$\mu_{sgs} = \bar{\rho} (C_w \Delta)^2 \frac{(s_{ij}^d s_{ij}^d)^{2/3}}{(\tilde{S}_{ij} \tilde{S}_{ij})^{5/2} + (s_{ij}^d s_{ij}^d)^{5/4}}, \quad (2.33)$$

where  $C_w$  is a model constant, which has a value of around 0.5.

The model has proven to be popular in the literature [38][49][50][51]. It has been shown to have a more accurate temperature prediction and finer resolved turbulence compared to the dynamic Smagorinsky model [52].

#### Vreman model

Another A-EVM, which was originally developed for turbulent shear flows, was proposed by Vreman [53]. It is constructed in such a way that dissipation is relatively small in transitional and near-wall regions. It is expressed in first-order derivatives, needs no explicit filtering, averaging or clipping procedures, and is rotationally invariant for isotropic filter widths. For these reasons, it is seen as a general-purpose model for engineering applications. It is expressed by

$$\mu_{sgs} = \bar{\rho} C_V \sqrt{\frac{B_\beta}{\tilde{g}_{ij} \tilde{g}_{ij}}}, \quad (2.34)$$

where

$$\begin{aligned} \beta_{ij} &= \Delta_m^2 \tilde{g}_{mi} \tilde{g}_{mj} \\ B_\beta &= \beta_{11} \beta_{12} - \beta_{12}^2 + \beta_{11} \beta_{33} - \beta_{13}^2 + \beta_{22} \beta_{33} - \beta_{23}^2. \end{aligned} \quad (2.35)$$

However, it has been shown to underperform in a combustion setting compared to the WALE and Smagorinsky models because of the underprediction of the eddy viscosity, which directly impacts the predicted heat release [54].

Examples in the literature are [54] and [55].

#### Sigma model

Although these previous A-EVMs improve upon the Smagorinsky model in terms of having zero eddy viscosity in pure shear, they do not vanish in the case of solid rotation. For this reason, Nicoud et al. developed the sigma model [56]. It uses the singular values of  $\mathbf{g}$  denoted by  $\sigma_1, \sigma_2, \sigma_3$  where  $\sigma_1 \geq \sigma_2 \geq \sigma_3$ , hence the name. The eddy viscosity of the model is given by

$$\mu_{sgs} = \bar{\rho} (C_\sigma \Delta)^2 \frac{\sigma_3 (\sigma_1 - \sigma_2) (\sigma_2 - \sigma_3)}{\sigma_1^2} \quad (2.36)$$

It also has cubic scaling near walls, which the Vreman model has not. Examples in the literature are [57] and [58]. Despite its demonstrated efficacy, the sigma model has not gained widespread popularity compared to the more familiar Smagorinsky and WALE models. This is largely attributed to the strong historical precedence and established familiarity within the fluid dynamics community that the latter models enjoy. Their ease of implementation, extensive documentation, and broad validation across various flow scenarios have entrenched them as the go-to choices in many turbulence modelling applications.

## 2.2. Reactive flows

The previous part covered non-reactive flow modelling, now a transition is made to reactive flows, which are flows that involve chemical reactions within them. More specifically, the focus is on combustion. Combustion is understood as a rapid reaction between a fuel and an oxidizer that releases heat and light. This process converts chemical energy into thermal energy, which can then be transformed into mechanical or electrical energy. In an aircraft engine, this thermal energy is converted into kinetic energy in the jet and mechanical energy through the turbines.

This section covers fundamental parts of combustion theory. It primarily prepares the reader for the literature study on chemical mechanisms and flame-turbulence interaction models, which are the main focus of combustion literature. The theoretical overview is inspired by a number of textbooks [59] [60].

### 2.2.1. Premixed and non-premixed combustion

A flame is defined as the region where combustion occurs. It is characterized by the release of heat and light. The nature of a flame is significantly influenced by the method of mixing the fuel with the oxidizer. In premixed combustion, this blending occurs before the combustion process. After the fuel-oxidizer mixture is ignited, the flame propagates through the mixture. The speed and nature of this flame propagation are influenced by various factors including pressure, temperature, the presence of turbulence and the mixture's composition. The mixture composition is often defined in terms of the equivalence ratio  $\phi$ . It is the ratio between the actual fuel-to-oxidiser ratio and stoichiometry. Stoichiometry refers to an exact balance of reactants needed for a chemical reaction to proceed completely, i.e. no leftover fuel or oxidizer. If  $\phi = 1$ , the mixture is stoichiometric. If  $\phi < 1$ , the mixture is (fuel-)lean, indicating there is more oxidizer than required for the complete combustion of the fuel. If  $\phi > 1$ , the mixture is rich, meaning there is excess fuel in the mixture compared to the stoichiometric ratio. Examples of premixed combustion are (petrol) internal combustion engines, gas stoves and boilers.

In non-premixed combustion, also known as diffusion combustion, the fuel and oxidizer are not mixed before they enter the combustion zone. This type of combustion is characterized by a physical mixing process that occurs during combustion itself. The fuel and oxidizer enter the combustion chamber separately and combustion occurs at the interface where the fuel and oxidizer meet and mix. The rate of combustion is often controlled by the rate at which the fuel and oxidizer can mix, making the mixing process a critical aspect of this combustion type. The efficiency and emissions of non-premixed combustion systems are highly influenced by the mixing process. Incomplete mixing can lead to incomplete combustion, resulting in higher emissions of pollutants like unburnt hydrocarbons, carbon monoxide, and particulate matter. Therefore, optimizing the mixing process is crucial for enhancing combustion efficiency and reducing emissions in non-premixed combustion systems. It is prevalent in many practical applications such as diesel engines, industrial furnaces, and some types of gas turbines.

The efficiency of premixed combustion is often higher than that of non-premixed combustion due to the homogeneous mixture of fuel and oxidizer. This homogeneity ensures that the fuel is completely burned, reducing the emission of unburned fuel and other pollutants. The explicit control over the equivalence ratio also allows for a more stable and controllable combustion process, which is crucial in applications like internal combustion engines and gas turbines. Non-premixed flames, in contrast, tend to burn closer to stoichiometric ratios. This leads to higher flame temperatures, which introduces problems like high  $\text{NO}_x$  production. However, premixed combustion also poses certain challenges. The most significant is the risk of unwanted ignition or explosion, especially in confined spaces or under high-pressure conditions. Premixed fuel-air mixtures are highly flammable and, if not carefully managed, may ignite unexpectedly. Safety measures and careful design are therefore essential in these systems.

Partially premixed combustion represents an intermediate process between premixed and non-premixed combustion. It occurs in systems where the fuel and oxidizer are not entirely mixed before combustion but are also not completely separate. This type of combustion can be found in practical applications like certain types of internal combustion engines and industrial burners. Partially premixed combustion is particularly relevant in the context of reducing emissions. It allows for better control over the formation of pollutants like nitrogen oxides ( $\text{NO}_x$ ) and particulate matter, as the combustion can be tuned

to optimize the balance between premixed and diffusion combustion. Research in this area focuses on understanding the complex interactions between mixing, combustion, and emissions. This involves studying the fluid dynamics and chemistry of partially premixed flames and developing advanced computational models to simulate these processes. The aim is to optimize combustion efficiency while minimizing environmental impacts.

### 2.2.2. Chemical Kinetics

Chemical reactions drive the combustion process. Chemical kinetics deals with understanding the rates of these reactions. It is crucial for uncovering the detailed steps (mechanism) by which a reaction proceeds. The central theme of kinetics is the rate of a reaction, which is influenced by various factors including the nature of the reactants, the concentration of reactants and products, the temperature, and the presence of a catalyst.

A foundational concept in kinetics is the rate law, which expresses the rate of a reaction as an empirical function of the concentration of reactants. Consider this single irreversible elementary reaction:



where  $\nu_s^{(r)}$  and  $\nu_s^{(p)}$  denote the stoichiometric coefficients of the reactants and products respectively.

The rate law for species  $i$  is given by

$$\frac{dc_i}{dt} = -k \prod_{s=1}^{n_s} c_s^{\nu_s^{(r)}}, \quad (2.38)$$

where  $c$  represents the molar concentration. In combustion, typically more than one reaction occurs. Consider a set of  $n_r$  reactions

$$\frac{dc_i}{dt} = \sum_{r=1}^{n_r} k_r (\nu_s^{(p)} - \nu_s^{(r)}) \prod_{s=1}^{n_s} c_s^{\nu_s^{(r)}} \quad (2.39)$$

The interplay between different species is a key aspect: the concentration of one species influences the rate at which another is formed. This change in concentration then impacts the first species in turn. This cyclical influence reflects the dynamic nature of combustion reactions, where the presence and concentration of each species have interconnected effects. The rate of change of the concentration of each species is expressed as an Ordinary Differential Equation. Modelling the chemical kinetics, therefore, requires solving a set of ODES.

Due to the high amounts of thermal energy present in combustion, some products can revert back to reactants. These are called reversible reactions. In such reactions, the forward process (reactants forming products) and the reverse process (products reforming reactants) occur simultaneously. Over time, these reactions can reach a dynamic equilibrium, where the rates of both forward and reverse reactions are equal, leading to constant concentrations of both reactants and products. These equilibrium concentrations depend on the ratio of forward and backward rate constant  $k$ .

The rate constant is often expressed as a function of the temperature through the Arrhenius equation:

$$k = AT^\beta \exp\left(-\frac{E_a}{\mathcal{R}T}\right), \quad (2.40)$$

where  $A$  is the pre-exponential factor,  $E_a$  the activation energy and  $\mathcal{R}$  the universal gas constant. Note that this equation differs from the classical Arrhenius equation through the addition of temperature exponent  $\beta$  that reflects the temperature dependence of the pre-exponential factor  $A$ .  $\beta$  is zero in the classical Arrhenius equation. Activation energy is the threshold energy level that reactants must

overcome for a chemical reaction, such as combustion, to proceed. In combustion, the heat released from exothermic reactions often sustains the reaction by providing the necessary energy to overcome activation barriers for subsequent reactions. To initialise this process in a flame, an external source of ignition, e.g. electric spark, is often used. Alternatively, the reactants can also spontaneously ignite if their temperature is raised high enough. This is called auto-ignition.

### 2.2.3. Thermodynamics of combustion processes

Before a reactive version of the Navier-Stokes equation can be constructed, the thermodynamics behind the combustion process need to be understood.

The first law states that the change in internal energy of a system ( $\Delta U$ ) is equal to the heat ( $Q$ ) added to the system minus the thermodynamic work done by the system. In a constant pressure process, the work done by the system is pressure times the volume change ( $P\Delta V$ ), so the first law becomes:

$$\Delta U = Q - P\Delta V$$

This equation can be rearranged as

$$Q = \Delta U + P\Delta V = \Delta H.$$

Here  $H$  is introduced as an important thermodynamic quantity called enthalpy. In flow equations, the specific enthalpy  $h$  is typically used. Enthalpy is particularly useful in the context of chemical reactions and phase changes, where it helps in calculating the heat absorbed or released. For example, in a chemical reaction happening at constant pressure, the heat released or absorbed is equal to the change in enthalpy of the reactants and products. This is especially relevant in combustion.

Enthalpy is needed for capturing the connection between chemical and thermal energy. The relationship between the change in enthalpy and the change in temperature for a substance at a constant pressure is given by

$$\Delta h = \int_T^{T+\Delta T} c_p dT, \quad (2.41)$$

where  $c_p$  is the specific heat capacity at constant pressure. This type of enthalpy is often referred to as sensible enthalpy  $h_s$ . It is the portion of enthalpy of a system that is associated with the change in temperature of the system, as opposed to changes in phase or chemical composition.

The chemical enthalpy change in a system can be captured by the enthalpy of formation  $\Delta h^\circ$ . It is a thermodynamic quantity that measures the change in enthalpy when one mole of a compound is formed from its elements in their standard states. The standard state of a substance is its phase and form as it exists at 1 bar of pressure and a specified temperature, typically 298 K. Hess's law states that the total enthalpy change during a chemical reaction is the same whether the reaction is made in one or several steps. In other words, the enthalpy change for a chemical process is independent of the pathway between the initial and final states. The change in enthalpy through the conversion of reactants in their products can, therefore, be calculated as

$$\Delta h = \Delta h_p^\circ - \Delta h_r^\circ \quad (2.42)$$

The standard enthalpies of formation for a large number of substances have been measured and tabulated. One of the most popular of these tabulations is the JANAF tabulation.

The third type of enthalpy is latent enthalpy, which is associated with phase changes (like melting or boiling) at constant temperature. During a phase change, the system absorbs or releases energy, but its temperature remains constant. However, in the context of this study, the focus is exclusively on fluids in their gaseous state, rendering a detailed discussion of latent enthalpy beyond the scope of this work.

### 2.2.4. Governing equations of reactive flows

Transitioning from the non-reactive Navier-Stokes equations to the reactive version involves integrating chemical reactions into the fluid dynamics. This is done by introducing additional equations to the system to account for the effects of multicomponent mixtures and chemical reactions in the flow.

The first type of equation that is introduced is for species transport. It models the evolution of the mass fractions in the mixture. The mass fraction for a species represents the ratio of the mass of one species to the total mass of the mixture in a control volume. It can be related to the species concentration as  $Y_m = c_m M_m / \rho$ , where  $M_m$  is the molar mass of the species. The sum of all mass fractions in the species has to add up to one. The transport equation for each species  $m$  is given by

$$\frac{\partial \rho Y_m}{\partial t} + \frac{\partial \rho u_i Y_m}{\partial x_i} + \frac{\partial \rho V_{m,i} Y_m}{\partial x_i} = \dot{\omega}_m, \quad (2.43)$$

where  $V_m$  and  $\dot{\omega}_m$  denote the diffusion velocity and chemical source term of species  $m$  respectively. The sum of both reaction rates and diffusive fluxes has to add up to zero to preserve the conservation of mass, i.e.  $\sum_{m=1}^{n_s} \dot{\omega}_m = 0$  and  $\sum_{m=1}^{n_s} V_{m,i} Y_m = 0$ . Modelling the diffusivity requires special attention for lean hydrogen combustion. Therefore, it is treated in more detail below. The chemical source term is retrieved by solving the set of ODEs associated with the chemical kinetics ( $\dot{\omega}_m = \frac{dc_m}{dt} \frac{M_m}{\rho}$ )

The second equation that is introduced concerns the conservation of energy. Typically, this is formulated in terms of the mixture's sensible enthalpy and can be represented as follows:

$$\frac{\partial \rho h_s}{\partial t} + \frac{\partial \rho u_i h_s}{\partial x_i} = \frac{\partial p}{\partial t} + \frac{\partial u_i p}{\partial x_i} + \tau_{ij} \frac{\partial u_i}{\partial x_j} - \frac{\partial}{\partial x_i} \left( -\lambda \frac{\partial T}{\partial x_i} + \rho \sum_{m=1}^{n_s} (h_{s,m} Y_m V_{m,i}) \right) + \dot{\omega}_T + \dot{Q} \quad (2.44)$$

where  $\lambda$  is the thermal conductivity and  $\dot{Q}$  a heat source term, which can model for example thermal radiation or a laser. The thermal source term  $\dot{\omega}_T$  originates from the chemical reactions and can be calculated with the enthalpy of formation as

$$\dot{\omega}_T = - \sum_{m=1}^{n_s} \Delta h_m^\circ \dot{\omega}_m \quad (2.45)$$

The first two terms on the RHS relate to pressure fluctuations. The third to viscous heating. In low Mach flows ( $Ma < 0.3$ ), they are typically neglected to simplify the equation.

#### Mixture properties

For non-reactive flows, mixture properties are typically assumed to be constant. In combustion, however, this is not valid anymore due to large changes in composition and temperature. A number of models for those quantities that are popular in fluid dynamics, and CFD in particular, are discussed here.

Density is a fundamental property that links the mass, momentum, and energy equations within the flow equations. Changes in temperature and mixture composition have a big influence on its value. Under ideal gas assumptions, the density can be related to pressure, temperature and mixture composition through the equation of state given by

$$\rho = \frac{p}{T} \frac{M}{\mathcal{R}}, \quad (2.46)$$

where  $M$  is the mean molar mass of the mixture, which can be calculated as  $M = (\sum_{m=1}^{n_s} Y_m / M_m)^{-1}$ .

Sutherland's law is an empirical formula that provides a way to estimate the dynamic viscosity of an ideal gas as a function of temperature. It is particularly useful because the viscosity of a gas is known to vary with temperature, but not with pressure. Sutherland's law can be expressed with the following formula:

$$\mu = \frac{A_s \sqrt{T}}{1 + T_s/T}, \quad (2.47)$$

where  $A_s$  is an empirical coefficient based on the chosen reference temperature  $T_s$ . It is important to note that various notations of Sutherland's Law exist, each employing different empirical coefficients. The version presented here is chosen for its relevance and implementation in the subsequent model development.

Eucken's expression relates the thermal conductivity  $\lambda$  to its viscosity and specific heat capacities. It is an empirical relationship derived from kinetic theory, and it provides a means to estimate the thermal conductivity of a gas when its viscosity is known. For nitrogen gas it is given by

$$\lambda = \mu c_v \left( 1.32 + \frac{1.77\mathcal{R}}{c_v M} \right), \quad (2.48)$$

where heat capacity at constant volume can be retrieved as  $c_v = c_p - \mathcal{R}/M$ .

### Molecular diffusion

The diffusive flux  $Y_m V_{m,i}$  appears both in Equation 2.43 and Equation 2.44. In a multicomponent mixture, solving the diffusive flux exactly is a challenging task because it involves interactions between multiple diffusing species where each species is influenced by the presence and movement of the other species. A way to simplify these calculations is to use a carrier species that is much more abundant than the other species. By adopting this method, the diffusion of each species can be primarily expressed in relation to this carrier species. For instance, in most combustion processes, air serves as the oxidizer, making nitrogen, which is abundant in air, an effective carrier species. Fick's law expresses the diffusive flux of each species in terms of the mass fraction gradients as

$$Y_m V_{m,i} = -D_m \frac{\partial Y_m}{\partial x_i} - \frac{D_{m,th}}{\rho T} \frac{\partial T}{\partial x_i} \quad (2.49)$$

$D_m$  is the diffusion coefficient or diffusivity of species  $m$ .  $D_{m,th}$  is the thermal diffusivity and can be calculated for the mixture as  $D_{th} = \lambda/(\rho c_p)$ . The last term is caused by thermal diffusion due to temperature gradients and is called the Soret effect. This gradient causes the molecules in the mixture to move from the warmer to the cooler region at different rates, depending on their thermal properties. As a result, the composition of the mixture becomes different in different parts of the system. The Soret effect is often discussed with the Dufour effect, which is its counterpart: it causes an energy flux due to the mass concentration gradient. These terms are often neglected in practical combustion settings, however, due to low relative magnitude compared to other dominant transport phenomena like convection and turbulent diffusion.

$D_m$  can be calculated in several ways. A simple approach uses constant Lewis or Schmidt numbers to relate it to the thermal diffusivity or dynamic viscosity respectively:

$$Le_m = \frac{D_{th}}{D_m} \quad (2.50)$$

$$Sc_m = \frac{\mu/\rho}{D_m} \quad (2.51)$$

The Lewis numbers of the species in hydrocarbon-air combustion are typically around unity. In those cases, the unity Lewis number assumption, i.e.  $Le_m = Le = 1$ , is usually made. The Lewis number of hydrogen (and atomic hydrogen), however, is typically around 0.3, making this assumption invalid for hydrogen-air flames. In those cases, the mixture-averaged approach is preferred. It calculates the diffusivity of each species using the mole fraction and binary diffusion coefficient:

$$D_m = \frac{1 - Y_m}{\sum_{j \neq m} X_j / \mathcal{D}_{mj}}, \quad (2.52)$$

where  $X_j$  denotes the molar fraction and  $D_{m,j}$  is the binary diffusion coefficient from kinetic gas theory.

### 2.2.5. Modelling turbulent flames

The equations governing reactive flows can be directly solved in the case of laminar flows. When dealing with turbulent flows, DNS is an option, but as previously discussed, this method becomes computationally expensive at higher Reynolds numbers. This high computational demand restricts DNS primarily to academic or research settings, where detailed analysis is necessary, and computational resources can be dedicated. For more practical applications, Large Eddy Simulation (LES) is a more viable alternative.

The same filtering operation as in Equation 2.12 can be applied to the flow equations. However, in the context of combustion simulations, significant density fluctuations are frequently encountered. Favre filtering is applied to prevent additional unclosed terms explicitly depending on the statistics of the density fluctuations. For the same variable  $q$ , it is given by

$$\tilde{q} = \frac{\overline{q\rho}}{\bar{\rho}}, \quad (2.53)$$

Filtering the conservation equations for mass, momentum, enthalpy and species gives the following set of equations:

- Conservation of mass:

$$\frac{\partial \bar{\rho}}{\partial t} + \frac{\partial \bar{\rho} \tilde{u}_i}{\partial x_i} = 0 \quad (2.54)$$

- Conservation of momentum:

$$\frac{\partial \bar{\rho} u_i}{\partial t} + \frac{\partial \bar{\rho} \tilde{u}_i \tilde{u}_j}{\partial x_i} = -\frac{\partial \bar{p}}{\partial x_i} + \frac{\partial}{\partial x_i} \left( \bar{\tau}_{ij} - \bar{\rho} \left( \underbrace{\widetilde{u_i u_j}}_{(1)} - \tilde{u}_i \tilde{u}_j \right) \right) \quad (2.55)$$

- Species transport (for  $m = [1, \dots, n_s]$  species):

$$\frac{\partial \bar{\rho} \tilde{Y}_m}{\partial t} + \frac{\partial \bar{\rho} \tilde{u}_i \tilde{Y}_m}{\partial x_i} = \frac{\partial}{\partial x_i} \left( \overline{V_{mi} Y_m} - \bar{\rho} \left( \underbrace{\widetilde{u_i Y_m}}_{(2)} - \tilde{u}_i \tilde{Y}_m \right) \right) + \bar{\omega}_m^{(3)} \quad (2.56)$$

- Enthalpy balance:

$$\frac{\partial \bar{\rho} \tilde{h}_s}{\partial t} + \frac{\partial \bar{\rho} \tilde{u}_i \tilde{h}_s}{\partial x_i} = \frac{\partial}{\partial x_i} \left( \lambda \frac{\partial \bar{T}}{\partial x_i} - \bar{\rho} \left( \underbrace{\widetilde{u_i h_s}}_{(4)} - \tilde{u}_i \tilde{h}_s \right) \right) + \bar{\omega}_T^{(5)} \quad (2.57)$$

Filtering the conservation equations leads to several unclosed terms. Term (1) is closed by the SGS scale stress model, which has been extensively covered in section 2.1. Terms (2) and (4) are generally closed using a simple gradient approximation:

$$\widetilde{u_i Y_m} - \tilde{u}_i \tilde{Y}_m = -D_{m,sgs} \frac{\partial \tilde{Y}_m}{\partial x_i} \quad (2.58)$$

$$\widetilde{u_i h_s} - \tilde{u}_i \tilde{h}_s = -D_{th,sgs} \frac{\partial \tilde{h}_s}{\partial x_i} \quad (2.59)$$

The focus of combustion literature is typically on closing term (3). Closing the term  $\bar{\omega}_m$  is not trivial as it is strongly affected by the SGS turbulence, which is not known in LES. Closure mainly consists of two modelling choices. The first one is on how the chemistry is described. The choice is mainly on which chemical mechanism to use and whether to model kinetics fully or use some form of reduction. The second choice is on how to model the effect of the subgrid-scale turbulence on the source term. The next chapter gives an overview of the most popular options used for these choices in the literature. If  $\bar{\omega}_m$  is closed, the term (5) follows from it through Equation 2.45.

### 2.2.6. Numerical solution algorithms

The Navier-Stokes equations consist of a set of nonlinear partial differential equations which are often very difficult and expensive to solve. The nonlinearity of the convective term makes analytical solutions impossible for most practical cases. Furthermore, the coupling between pressure and velocity creates a complex interdependence. The need for fine resolution also leads to the creation of large meshes, which in turn impose substantial computational demands. An efficient solution algorithm is needed. A summary of a few prominent solution algorithms is provided following [61].

#### SIMPLE algorithm

The Semi-Implicit Method for Pressure-Linked Equations (SIMPLE) algorithm [62] is a widely used method for addressing incompressible fluid flow problems in Computational Fluid Dynamics (CFD). Its primary advantage lies in its capacity to decouple and iteratively solve the velocity and pressure fields, enhancing manageability and computational efficiency. The algorithm uses a relationship between pressure and velocity to iteratively correct the guessed pressure field, ensuring mass conservation. Employing an iterative process, SIMPLE alternates between solving momentum and pressure correction equations until it reaches convergence. To improve stability in that process, SIMPLE uses under-relaxation. Under-relaxation works by slowing down the changes to the solution variables (like pressure and velocity) from one iteration to the next. This is achieved by blending the new values computed in an iteration with the old values from the previous iteration, using a specified under-relaxation factor. This is a number between 0 and 1. A factor of 1 means no under-relaxation (i.e., the full computed change is applied), while a factor closer to 0 means heavy under-relaxation (i.e., only a small portion of the computed change is applied). Properly chosen under-relaxation factors can significantly enhance the stability and convergence of the algorithm, especially in cases with complex boundary conditions or high Reynolds numbers. However, too much under-relaxation can slow down the convergence process.

The SIMPLE algorithm is suitable for a wide range of flow problems, including those with complex geometries and boundary conditions. It is mainly used for generating steady flow solutions in CFD, directly applicable to scenarios where flow variables reach a static state. It can also be used in transient solutions by solving the SIMPLE loop for every timestep. However, this is quite expensive for a large number of timesteps. A new algorithm better tailored to transient solutions is needed.

#### PISO algorithm

The Pressure-Implicit with Splitting of Operators (PISO) algorithm [63] is designed to address the intrinsic coupling between pressure and velocity fields in fluid dynamics, a challenge that is particularly pronounced in transient flow scenarios. Unlike SIMPLE, which is well-suited for steady-state problems, PISO introduces additional steps to refine the pressure-velocity coupling within each time step, making it more suitable for managing fast changes in the flow field. The typical steps involved in the PISO algorithm are as follows. Initially, a velocity field is predicted without considering the pressure changes. This step uses the momentum equations with an estimated pressure field. The pressure field is then corrected to ensure mass conservation. This involves solving a pressure equation (often a Poisson equation) derived from the continuity equation and the predicted velocity field. Based on the pressure correction, the velocity field is updated to reflect the new pressure values. This step ensures that the updated velocity field satisfies the momentum equations with the corrected pressure. Unlike SIMPLE, which typically includes one pressure correction step, PISO can repeat the pressure and velocity correction steps multiple times within each time step. This repetition enhances the accuracy of the pressure-velocity coupling, especially important in transient simulations.

While PISO offers enhanced accuracy for transient flows, it is generally more computationally intensive than SIMPLE due to the additional correction steps. However, this increased computation can be offset by the ability to use larger time steps, reducing the total number of time steps required for a simulation.

One of the key advantages of PISO is its capability to handle larger time steps and higher Courant numbers (Equation 2.9). This feature is crucial for enhancing computational efficiency in transient flow simulations. So although PISO is generally more computationally intensive than SIMPLE due to the additional correction steps, this can be offset by the ability to use larger time steps, reducing the total number of time steps required for a simulation. Thereby it balances computational intensity with efficiency.

Note that, unlike SIMPLE, the PISO algorithm typically does not use under-relaxation. This distinction arises from the nature of transient flow simulations, where choosing smaller time intervals is essential to maintain the accuracy of the evolving solution. In these transient scenarios, the need for under-relaxation to achieve convergence is generally less critical. However, by integrating aspects of the SIMPLE algorithm's robustness into PISO, it becomes feasible to use larger time steps in the simulations. This integration allows for enhanced flexibility in handling time-dependent flows while maintaining solution accuracy and stability.

#### PIMPLE algorithm

The integration of the under-relaxation of SIMPLE into the PISO algorithm leads to a hybrid called PIMPLE. PIMPLE essentially merges the iterative pressure-velocity coupling method of PISO with the robustness of the SIMPLE algorithm. In doing so, it brings together the best of both worlds: the ability of PISO to handle transient flows and the stability of SIMPLE in steady-state problems. This combination allows for maintaining temporal accuracy at high Courant numbers, even exceeding  $Co = 1$  with second-order time schemes.

PIMPLE has high flexibility due to a set of key parameters that can be tuned. The number of PISO loops per SIMPLE iteration can be adjusted. This parameter allows users to control the degree of pressure-velocity coupling within a time step. A higher number of PISO loops may improve accuracy but can increase computational cost. If the number of PISO loops is set to one, PIMPLE essentially reverts to the SIMPLE algorithm. Another parameter is the under-relaxation factor from SIMPLE. An optimal choice of parameters balances accuracy with efficiency.

This chapter has covered a short theoretical background in fluid flow, addressing both non-reactive and reactive flows, along with a number of prominent numerical solution algorithms. It serves as a crucial foundation for understanding advanced topics in Large Eddy Simulation (LES) for combustion. This chapter aims to bridge the gap to more specialized literature on LES, setting the stage for more in-depth discussions on chemical kinetics and flame-turbulence interactions in combustion processes.

# 3

## Literature review

This chapter provides a comprehensive overview of turbulent combustion research. It delves into both experimental approaches and numerical simulation techniques. The emphasis in the numerical section is on Large Eddy Simulation (LES) applied to combustion processes, including detailed discussions on modelling the chemical kinetics and the interaction between flames and turbulence on the subgrid scales. Subgrid-scale stress models are not the main focus here, as they are considered to be mainly a part of the non-reactive flow canon. However, they are examined in chapter 2. For the experiments, this chapter considers a few burner studies, particularly those relevant to aircraft engine combustors.

### 3.1. Modelling chemical kinetics

Chemical kinetics can be accurately represented by directly solving all the reaction equations within the solver loop. However, this approach can be computationally expensive. To mitigate this, several methods have been developed and documented in the literature to efficiently reduce computational costs without significantly compromising accuracy.

#### 3.1.1. Detailed chemistry and reduced schemes

The system of ODEs derived from Equation 2.39 can be directly integrated into CFD simulations. This process necessitates the selection of a chemical kinetic mechanism. It is a theoretical framework to understand how reactants are transformed into products over time. It not only includes the set of species and reactions but also includes the model parameter of Equation 2.40. There are multiple types of chemical mechanisms depending on the level of detail.

A detailed chemistry mechanism tries to model the chemical pathways as completely and precisely as possible. These mechanisms often involve species that are created and consumed within the sequence of reactions. These species, known as intermediates, are crucial for the progression of the overall reaction but might not be present in the final products. This amount of detail, however, comes with a big computational cost. It includes an exhaustive list of all possible reactions with all formable species for a given oxidiser-fuel combination. Due to its complexity, there are rarely unique detailed schemes [64]. Popular examples of detailed mechanisms for hydrogen-air combustion are Yetter [65], Mueller [66], Li [67], San Diego [68], Ó Conaire [69] and DRM-19 [70].

In combustion chemistry, managing the vast number of reactions and species in a detailed mechanism is a significant challenge. One effective approach to simplify these models is the creation of skeletal mechanisms. These mechanisms streamline the process by eliminating species and reactions that have minimal impact on the phenomena under study. A classic example of this is the adaptation of methane-air mechanisms for hydrogen-air combustion, where all carbon-based species are removed. This technique is frequently applied to the widely used GRI-3 mechanism.

Further reduction in the number of reactions can be achieved through reduced mechanisms. These

mechanisms distil the entire combustion process into a set of global reactions, effectively capturing key flame properties like flame propagation and reducing computational demands. Reduced mechanisms are typically categorized into two types: empirically reduced and systematically reduced mechanisms.

Empirically reduced mechanisms aim to replicate global flame properties with a minimal number of reaction steps, generally between one and four. These mechanisms are fine-tuned by comparing their reactions with those in a detailed mechanism and adjusting the parameters of the Arrhenius equations to align reaction rates. Various algorithms have been developed to automate the optimization of these chemical rate parameters, enhancing their accuracy and efficiency.

Systematically reduced mechanisms take a different approach. They choose to set global reactions as a linear combination of elementary equations of a detailed mechanism. This goes hand-in-hand with an assumption of Quasi Steady-State Approximation (QSSA) and/or Partial Equilibrium Approximation (PEA). The former assumes that as some species are much more reactive than others, their variation is already over when the others are still evolving. This can be used to eliminate one of these reactions from the mechanism by setting their change in concentration over time to zero and expressing them as a linear combination of the other reactions. The latter is similar but sets the change in extent, not concentration, over time to zero [71]. Both assumptions lead to algebraic relations between elementary equations.

The early reduced mechanisms were basic few-step global mechanisms. Initially, these mechanisms had limitations in accuracy and were primarily useful for global studies rather than detailed analyses. This was due to their ad-hoc nature and simplistic approach, which failed to capture the intricate dynamics of combustion processes [72]. The pursuit of improvement led to a crucial observation: the disparity between chemical and flow time scales in combustion reactions. Researchers realized that the rapid chemical time scales could be decoupled from the slower flow time scales, paving the way for more sophisticated reduction techniques. This understanding led to the development of two prominent methods: the Computational Singular Perturbation (CSP) method and the Intrinsic Low-Dimensional Manifold (ILDM) method.

The CSP method [73] dynamically identifies fast time scales and automatically adjusts to these variations, providing a highly accurate representation of the combustion process. However, this accuracy comes at the cost of increased computational demands, which limits its practicality in complex simulations. The CSP method's ability to adapt to varying conditions makes it a powerful tool, but its computational intensity often restricts its use to simpler models or academic studies. [72].

The Intrinsic Low-Dimensional Manifold method uses eigenvector analysis on the Jacobian of the chemical source term instead. The eigenvectors corresponding to fast time scales are assumed to be steady-state. The eigenvectors corresponding to the slow time scale are used to construct a low-dimensional manifold. This manifold effectively reduces the dimensionality of the system, simplifying the chemical kinetics while preserving critical aspects of the combustion process.

The ILDM method is effective for systems where chemical reactions are the dominant factor, but it falls short in situations where diffusion is a key element, such as in turbulent flows or at low temperatures. Its failure to consider diffusion leads to less accurate models in cases where diffusion greatly influences overall behaviour, notably in flame fronts or catalytic processes where reactions and diffusion are interconnected. To overcome these shortcomings, the REaction–Diffusion Manifold (REDIM) method [74] enhances ILDM by incorporating diffusion. It does this through a relaxation to an invariant system manifold, which is governed by a parabolic partial differential equation system. This combination of reaction kinetics and diffusion provides a more comprehensive and precise depiction of chemical systems, particularly in scenarios where diffusion is a major influence.

### 3.1.2. Flamelet-tabulation approach

Flamelet approaches in combustion modelling take a physical rather than a mathematical approach to reduce complexity. This strategy is based on the assumption that a multi-dimensional turbulent flame can be represented by a series of one-dimensional laminar flames, known as flamelets. Under this assumption, the complex (unfiltered) reactive flow equations become significantly simpler and easier to solve. Flamelet characteristics under a wide range of conditions can be precomputed and stored

in a database. These characteristics are then accessed using specific coordinates during simulations, making this method computationally efficient.

#### Tabulation strategies

There are multiple strategies to fill the tables using flamelet solutions. The most important ones are given below.

##### *FPI*

Flame Prolongation of ILDM (FPI) enhances the traditional ILDM approach by using flamelet results. Developed by Gicquel et al. (2000) [75], it specifically addresses the limitations of ILDM in modelling regions of lower reactivity, which are common in combustion processes. FPI achieves this by incorporating laminar premixed free flame solutions into the ILDM framework, thus extending the range and accuracy of the manifolds. The extended manifolds offer an improved representation of flame dynamics, particularly in areas where traditional ILDM might struggle. The results of these enhanced manifolds are then tabulated for efficient access and use in simulations, enabling more accurate modelling across a wider range of combustion scenarios.

##### *FGM*

Flamelet Generated Manifold (FGM) method proposed by van Oijen and Goey (2000) [72] starts from the flamelet assumption, that a multidimensional can be described by a collection of one-dimensional premixed flames, and combines it with the concept of constructing a low-dimensional manifold to describe the system. This approach streamlines the solving of conservation equations by focusing solely on controlling variables, while reaction rates and other vital parameters are conveniently stored in a table for easy access. What sets FGM apart from alternative methods is its remarkable adaptability. It has the capability to incorporate specific phenomena such as differential diffusion,  $\text{NO}_x$  production, heat losses, and strain through the manipulation of controlling variables. Adjustments made at the flamelet level can be translated to the flow calculations using these specified controlling variables. sub-section 3.1.2 elaborates on the choice of controlling variables.

##### *FPV*

The Flamelet/Progress Variable (FPV) approach, initially developed by Pierce and Moin (2004) [76] for non-premixed flames, is based on the non-premixed flamelet model by Peters [77]. Unlike FGM and FPI, which were initially designed for premixed flames, FPV specifically targets non-premixed flames using a reaction progress variable to account for non-equilibrium chemistry. This method simplifies chemical kinetics through a singular reaction progress variable, contrasting with FGM's use of multiple reaction control variables. This method efficiently captures phenomena like extinction and re-ignition at a lower computational cost than Flamelet Generated Manifolds (FGM). However, FPV struggles with complex flames, particularly in accurately representing differential diffusion [78] Due to these limitations, FGM offers a more suitable choice for chemistry description in a versatile and practical model for a turbulent hydrogen combustion model.

#### Controlling variable selection

A main advantage of the flamelet approach over a mathematical approach is that there is more flexibility in choosing the set of coordinates. There is no silver bullet when selecting the appropriate coordinates. Instead, it depends on the phenomena of interest. An overview of the most important principle coordinates in the literature is given next.

##### *Progress variable*

An important coordinate to keep track of, especially in premixed combustion, is how far the process is in the conversion from fresh to burnt gases. That can be done using a progress variable  $Y_c$ , which is generally a non-dimensional parameter that consists of a selection of mass fractions of different species that ensure a monotonic and continuous evolution between the initial and final states. It is essential that each value of  $Y_c$  only corresponds to one point in the process so that the corresponding state can be uniquely identified. Typically  $Y_c$  is normalised as

$$c = \frac{Y_c - Y_c^{eq}}{Y_c^0 - Y_c^{eq}} \quad (3.1)$$

so that  $c = 0$  corresponds to the initial state and  $c = 1$  to the final state. Here  $Y_c^0$  corresponds to  $Y_c$  of the fresh gases and  $Y_c^{eq}$  to those in the equilibrium state.

#### Mixture fraction

Another commonly used coordinate is called the mixture fraction. This quantity is critical in cases where mixing phenomena need to be captured, such as in non-premixed or partially premixed combustion. A first and simple definition of the mixture fraction in single-step chemistry can be based on the mass fractions of the oxidiser and the fuel, and their stoichiometric ratio. However, when moving to multi-step chemistry, this quantity is no longer conserved. Instead, a definition based on the atomic or elemental mass fraction  $Y_e$  can be more useful. A famous example of such a mixture fraction for methane-air combustion is the Bilger formula [79]. Its hydrogen version is given as

$$Z = \frac{0.5W_{H_2} (Z_H - Z_H^O) - W_{O_2}^{-1} (Z_O - Z_O^O)}{0.5W_{H_2} (Z_H^F - Z_H^O) - W_{O_2}^{-1} (Z_O^F - Z_O^O)}, \quad (3.2)$$

where  $Y_e^O$  and  $Y_e^F$  denote the elemental mass fraction in the oxidiser and fuel stream respectively.  $W_e$  corresponds to the atomic weight of the element.

#### Enthalpy

When heat losses, e.g. through walls or the environment, need to be tracked, it is useful to consider total enthalpy  $h$  which is different from sensible enthalpy  $h_s$ . In adiabatic conditions, this quantity is conserved across constant-pressure flames. However, if heat exchanges occur, this is not the case anymore. As the temperature has a strong impact on the chemical source terms, it is useful in these non-adiabatic cases to compare them with the adiabatic case. A normalised version of this enthalpy is generally used as

$$h_n = \frac{h - h_{\min}(Z)}{h_{ad}(Z) - h_{\min}(Z)}, \quad (3.3)$$

where  $h_{\min}$  and  $h_h$  is an arbitrary minimal mixture and adiabatic enthalpy respectively.

#### NO<sub>x</sub> emissions

In cases where NO<sub>x</sub> emissions are investigated, a type of progress variable related to atomic nitrogen should be included. One option is to include it in the formulation of the progress variable  $Y_c$ . However, this inherently couples the fuel oxidation reaction to the NO<sub>x</sub> pathways, which is not always desirable. Another option is to include an extra and separate progress variable, e.g.  $Y_{NO}$ , that solely relates to NO formation.

#### Strain and curvature

Chen et al. (2021) [80] have shown that strain and curvature can directly alter the flame structure and combustion properties of a flammable mixture. To include these effects in a strained flamelet library, extra coordinates are needed. Knudsen et al. (2013) [44] use atomic hydrogen to keep track of the strain rate. Recently Wen et al. (2022) [81] extended this work to also use atomic hydrogen to track both strain and curvature effects.

When preparing the tabulation for the strained flamelet library, solutions in physical state space are constrained by the physics of canonical flames. For example, it is hard to come up with an experimental configuration of laminar flame that has negative strain due to its inherent instability. However, this has been observed in turbulent flames [82] [83]. A solution to this is to solve the flamelets in composition space [84].

#### Selected controlling variables

The selected model is the first implementation for a turbulent partially premixed hydrogen flame. The primary objective, therefore, is to analyse its predictive accuracy in relation to experimental results. Although analysing practical combustion designs for NO<sub>x</sub> production, heat loss effects and strain effects would be interesting and is a future ambition, it is, at present, considered out-of-scope. To capture the partially premixed nature of the flame, the progress variable and mixture fraction are chosen as controlling variables.

## 3.2. Subgrid-scale flame-turbulence interaction

Filtering the reactive flow equations for LES gives rise to the unclosed filtered source term  $\bar{\omega}$ . It differs from the source term  $\dot{\omega}$ , which is either obtained from solving the chemical kinetics or tabulation, and needs to be modelled through the flame-turbulence interaction model. While an LES only resolves the large scales in the flow, combustion mainly occurs in the subgrid scales. To couple the two, a model is needed. These models can be classified in one of three approaches.

### 3.2.1. Geometric approach

The geometrical approach is built upon the assumption that the flame front is thin compared to the smallest turbulent scales. Because of this assumption, the flame front is modelled as a thin layer to which the effects of molecular diffusion and chemical reactions are confined to. The flame propagates normally to the flame front. The summary below is largely based on Fiorina et al. (2015) [64].

#### Level set or "G-equation" formalism

The level set method assumes that the flame front is an infinitely thin propagating surface. Its position is tracked using the field variable  $G$ , which represents the signed distance to the flame front. The  $G$ -field is described by the kinematic description introduced by Kerstein et al. [85]

$$\frac{\partial G}{\partial t} + \tilde{\mathbf{u}} \cdot \nabla G = s_T |\nabla G|, \quad (3.4)$$

where  $s_T$  is the subgrid-scale turbulent burning velocity and needs to be modelled. In this field, a given iso-surface represents the instantaneous flame front position.

This method only gives information on the position of the thin reaction zone and not on the filtered flame structure [40]. Knowledge about the temperature around this reaction zone is also needed to consider the effects of heat expansion. Although these drawbacks, it is still a popular approach in the literature on premixed turbulent combustion due to its simplicity and low computational cost.

#### Filtered laminar flames

The next geometrical method also considers a thin flame front. However, instead of treating it as an infinitely thin iso-surface, it is treated as a one-dimensional laminar flame front, which is convected by the turbulent flow field. The reaction is described by filtered progress variable  $c$ , where  $c = 0$  represents a state with fresh reactants and  $c = 1$  a state with burnt products.

The key question in this approach is how to model the filtered flame front displacement  $\overline{\rho w |\nabla c|}$ . Boger et al. [86] propose a way to recast the flame front displacement as

$$\overline{\rho w |\nabla c|} = \langle \rho w \rangle_s \Xi |\nabla \bar{c}|, \quad (3.5)$$

where  $\langle \rho w \rangle_s$  denotes the conditional average of  $\rho w$  over the  $c = c^*$  surface, and  $\Xi$  the wrinkling factor. These two quantities need to be modelled and there are multiple strategies to do that.  $\Xi$  can be modelled using algebraic expressions, similarity assumptions, dynamic modelling or balance equations.  $\langle \rho w \rangle_s |\nabla \bar{c}|$  is modelled using the combination of a model and a filtered laminar one-dimensional flame solution.

Boger et al. (1998) [86] model  $\langle \rho w \rangle_s$  with the unburned density  $\rho_u$  and the laminar flame speed  $s_L$  as

$$\langle \rho w \rangle_s \approx \rho_u s_L, \quad (3.6)$$

and estimate  $|\nabla \bar{c}|$  by filtering a one-dimensional infinitely thin laminar premixed flame.

Duwig (2007) [87] takes another approach and extracts the term,  $\langle \rho w \rangle_s |\nabla \bar{c}|$ , directly by applying a filter over a one-dimensional laminar flame with the help of a Gaussian function in space.

A third popular strategy is called F-TACLES [40] and uses detailed chemistry simulations to tabulate the unclosed terms.

### Artificially thickened flamelet model

The last geometrical method that is covered is called the Artificially Thickened Flamelet model (ATF). It also tackles the problem that the flame front is thinner than the filter width, but addresses it in a different way. Originally proposed by Colin et al. (2000) [88], it considers a flame that is thicker than the real one, but has the same  $s_L$ . When the flame thickness  $\delta_L$  is widened by a sufficiently large factor  $\alpha$ , the artificially thickened can be resolved on the LES mesh. However, to achieve this, a number of quantities have to be scaled using proportionality in simple theories of laminar premixed flames. The laminar flame speed and thickness can be expressed as

$$s_L \propto \sqrt{D_{th}\bar{\omega}} \quad ; \quad \delta_L \propto \frac{D_{th}}{S_L}, \quad (3.7)$$

So, if the flame thickness is increased with factor  $\alpha$ , the thermal diffusivity has to be replaced with  $D_{th}\alpha$  and the reaction rate with  $\frac{\bar{\omega}}{\alpha}$ .

However, when changing these quantities, the Damköhler number changes as well. To compensate for this effect, an effective flame wrinkling factor  $\Xi$ , similar to the filtered laminar flame method, is introduced.

In conclusion, geometric approaches tackle the flame-turbulence interaction in a conceptually simple and intuitive way. However, they rely on strong simplifications of the flame structure and the turbulence-chemistry interaction, which may not capture all relevant physical processes, especially in cases with complex chemistry or strong turbulence-chemistry interactions.

### 3.2.2. Mixing approach

The mixing approach takes a different route. It develops a flame-turbulence interaction model based on mixing characteristics. The summary of the most important model given below is largely based on the review of Fedina et al. (2017) [89].

#### Eddy dissipation concept

The eddy dissipation concept is based on the assumption that combustion only takes place in fine structures of high vorticity and chemical reactivity. These regions are surrounded by regions of low vorticity and chemical reactivity. The reactive pockets interact with their surroundings through advection and diffusion so that the products and thermal energy gets distributed to the non-reactive regions.

The filtered reaction rates are calculated from the weighted average of reaction rates in the fine structures and their surroundings

$$\bar{\omega}_m = \gamma^* \dot{\omega}_m^* (\bar{\rho}, Y_m^*, T^*) + (1 - \gamma^*) \dot{\omega}_m^0 (\bar{\rho}, Y_m^0, T^0), \quad (3.8)$$

where  $\gamma^*$  represents the reacting volume fraction,  $\dot{\omega}_m^*$  the reaction rate in the fine structures and  $\dot{\omega}_m^0$  the reaction rate of the surroundings. The reaction rates are a function of mass density, mass fractions and temperature. Typically,  $\dot{\omega}_m^* \gg \dot{\omega}_m^0$ , so in general  $\dot{\omega}_m^0$  is often set to zero for simplicity.

The filtered mass fractions and temperature are calculated respectively by

$$\tilde{Y}_m = \gamma^* Y_m^* + (1 - \gamma^*) Y_m^0 \quad (3.9)$$

$$\tilde{T} = \gamma^* T^* + (1 - \gamma^*) T^0 \quad (3.10)$$

Determining  $\gamma^*$  can be done in several ways. One way is to estimate it through the cascade process [90], for which

$$\gamma^* = 1.02 (\nu / \Delta v')^{3/4}, \quad (3.11)$$

where  $\nu$  is the molecular viscosity and  $v'$  the subgrid velocity fluctuations given by  $\sqrt{2k/3}$ .

### Fractal model

The fractal model also rests on the EDC assumptions, but it uses a different method to calculate  $\gamma^*$ . The method is based on fractal-like behaviour in fine structures. It calculates  $\gamma^*$  as

$$\gamma^* = \gamma_N (\Delta/\ell_K)^{D_3-2}, \quad (3.12)$$

where  $\gamma_N$  is the ratio of the number of Kolmogorov scales to the total number of scales and  $D_3$  the local fractal dimension. The former needs to be estimated using a fractal generation process. Giacomazzi et al. (2000) [91] propose the analytical fit

$$\gamma_N \approx 1 - \left( (0.36 (\Delta/\ell_K - 1)) / \left( 1 + 0.0469 (\Delta/\ell_K - 1)^{2.7} \right) \right). \quad (3.13)$$

The latter is estimated using a box-counting method so that

$$D_3 = 3 - (\log(\pi) / \log(\Delta/\ell_K)). \quad (3.14)$$

### PaSR

The Partially Stirred Reactor (PaSR) model uses yet another approach to estimate  $\gamma^*$ . It uses theoretical estimates and DNS data to do this. It is given by

$$\gamma^* \approx \beta (v'/s_u)^{5/4} / \left( (\Delta/\delta_u)^{3/4} + \beta (v'/s_u)^{5/4} \right) \quad (3.15)$$

where  $\beta \approx 1.17$ .

### Linear Eddy Model

The Linear Eddy model takes a different approach than the EDC in handling mixing problems. It describes the turbulent mixing process by a simple one-dimensional stochastic rearrangement process that is applied to the one-dimensional scalar field. In this way, it is able to provide a direct estimation of  $\tilde{T}$  and  $\tilde{Y}_m$  without the need for additional transport equations.

The stochastic process rearranges the initial scalar distribution over a given segment of size  $l$  and can be viewed as the effect of an effect of a single vortex of size  $l$ , where  $l_k < l < \Delta$ .

All these mixing approaches are computationally quite efficient and it is the preferred approach in cases where the chemical reaction time scales are much shorter than the mixing time scales, or when detailed chemistry is not the primary concern, and the focus is on the overall flame behaviour, heat release, and macroscopic properties of the combustion system. However, due to its rather strong assumptions, information on, for example, the flame structure is lost. In those cases, a different approach should be taken.

### 3.2.3. Statistical approach

The statistical approach models the uncertainty coming from the flame-turbulence interactions of the subgrid scales using a Probability Density Function (PDF). The filtered thermochemical variable  $\tilde{\varphi}$  is found by averaging over all possible states at a specific point in time and space as

$$\tilde{\varphi}(x, t) = \int \varphi(\Psi) \tilde{P}(\Psi; x, t) d\Psi, \quad (3.16)$$

where  $\Psi$  represents the thermo-chemical state.

The system can be closed either by conditioning on mixture fraction or by using a Filtered Density Function (FDF).

### Conditional moment closure

The conditional moment closure method is a statistical approach for partially premixed or non-premixed combustion. It was proposed for LES by Navarro-Martinez et al. (2005) [92]. The flame-turbulence interaction effects are included in the PDF, just as in FDF approaches. However, the filtered chemical flame structure is described in mixture fraction space. The filtered mean conditioned on a specific mixture fraction  $Z$  is multiplied with the mass-weighted filtered density function of  $Z$  and is integrated over all possible values of the mixture fraction as

$$\tilde{\varphi}(x, t) = \int_0^1 \left( \overline{\varphi | Z^*}; x, t \right) \tilde{P}(Z^*; x, t) dZ^*. \quad (3.17)$$

However, it also has some drawbacks. It has large computational costs, especially for a high number of variables  $\varphi$ , and needs multiple closure schemes [64].

### Filtered density approach

The filtered density approach takes another direction. Here, the notation of Breda (2021) [51] is largely adopted.

The Probability Density Function (PDF) for a controlling variable  $\phi_\alpha$  at a specific point  $x$  in space and at a given time  $t$  can be represented by a Dirac delta function as

$$P_\alpha(\Psi_\alpha; x, t) = \delta(\Psi_\alpha - \phi_\alpha(x, t)), \quad (3.18)$$

where  $\Psi_\alpha$  represents the sample space. This means that  $P_\alpha$  is zero everywhere except where  $\Psi_\alpha = \phi_\alpha(x_i, t)$ .

Extending this to  $n_\alpha$  controlling variables, the marginal PDFs can be combined into a joint PDF as

$$P(\Psi; x, t) = \prod_{\alpha=1}^{n_\alpha} \delta(\Psi_\alpha - \phi_\alpha(x, t)). \quad (3.19)$$

The LES filter  $\mathcal{G}$  can be applied to this PDF which results in the Filtered probability Density Function (FDF)

$$\tilde{P}(\Psi; x_i, t) = \int_V \frac{\rho(x_i - x'_i)}{\bar{\rho}} P(\Psi; x'_i, t) \mathcal{G}(x_i - x'_i, \Delta(x_i)) dx'_i. \quad (3.20)$$

The FDF statistically represents the probable states within the filter volume. In other words, the probability that  $\phi$  resides in the interval  $[\Psi, \Psi + d\Psi]$  can be found by integrating this function.

There are two common strategies to determine  $\tilde{P}$ .

### Presumed filtered density approach

The first one makes an assumption on the distribution and is called the presumed filtered density approach. Usually, flamelet manifolds in steady flame regimes are described by two parameters: the mixture fraction  $Z$  and a second table parameter  $\mathcal{V}$ , which can be a progress variable, scalar dissipation rate, or enthalpy loss. The flame structure, which consists of the mass fractions and temperature, is generalised in the flamelet approach as  $\Psi(Z, \mathcal{V})$ . The flame-turbulence interaction is then modelled as

$$\tilde{\varphi}(x, t) = \iint \varphi(Z, \mathcal{V}) \tilde{P}(Z, \mathcal{V}; x, t) dZ d\mathcal{V}, \quad (3.21)$$

where, assuming independence, the joint PDF can be written as  $\tilde{P}(Z, \mathcal{V}) = \tilde{P}(Z) \tilde{P}(\mathcal{V})$ . Typically,  $\beta$  functions are used for this purpose as suggested by Cook and Riley (1994) [93]. In general, only the progress variable, or mixture fraction in case of non-premixed combustion, is modelled with a  $\beta$

distribution while the other parameters are kept constant using a Dirac function. The beta function for the mixture fraction is given by

$$\tilde{\mathcal{P}}(Z) = Z^{\alpha-1}(1-Z)^{\beta-1} \frac{\Gamma(\alpha+\beta)}{\Gamma(\alpha)\Gamma(\beta)}, \quad \alpha = \tilde{Z}(\gamma-1), \quad \beta = (1-\tilde{Z})(\gamma-1), \quad \gamma = \frac{\tilde{Z}(1-\tilde{Z})}{\tilde{Z}''^2} \quad (3.22)$$

The statistical moments of this function are transported and used to retrieve the filtered scalar quantities from a table.

#### Transported filtered density approach

A drawback of using the presumed FDF approach is that it assumes statistical independence between the controlling variables. Furthermore, the  $\beta$ -function is not appropriate for premixed combustion [38]. An alternative to assuming the form of the distribution is to model  $\tilde{P}$  using transport equations. Adopting the form of Breda et al. (2021) [51], the transport equation is given by

$$\begin{aligned} & \frac{\partial \tilde{\rho} \tilde{P}}{\partial t} + \frac{\partial \tilde{\rho} \tilde{u}_j \tilde{P}}{\partial x_j} + \sum_{\alpha=1}^n \frac{\partial}{\partial \Psi_\alpha} (\tilde{\rho} \tilde{\omega}_\alpha \tilde{P}) \\ & = \frac{\partial}{\partial x_j} \left[ \tilde{\rho} \left( \frac{\bar{\nu}}{Sc} + \frac{\nu_{SGS}}{Sc_{SGS}} \right) \frac{\partial \tilde{P}}{\partial x_j} \right] - \sum_{\alpha=1}^n \sum_{\beta=1}^n \frac{\partial^2}{\partial \Psi_\alpha \partial \Psi_\beta} \left( \tilde{\rho} \frac{\bar{\nu}}{Sc} \frac{\partial \phi_\alpha}{\partial x_i} \frac{\partial \phi_\beta}{\partial x_i} \Big|_{\phi=\Psi} \tilde{P} \right) \end{aligned} \quad (3.23)$$

One should notice that in the third term on the LHS, the chemical source term appears in closed form. This is an advantage for this method as it makes it possible to directly look up  $\tilde{\omega}_\alpha$  from the database.

A deterministic solution to this equation is too computationally expensive due to its high dimensionality. It can be solved instead by replacing this with a statistically equivalent system using a stochastic partial differential equation. A solution can then be found using a Monte Carlo simulation. There are typically two ways to approach this.

One way is to use Lagrangian Monte Carlo particle methods. Here, stochastic particles are simulated for each point in the mesh and are subjected to convection, molecular mixing, turbulent diffusion and chemical reactions. However, a sufficient number of particles is needed for each point in space and time to describe the distribution accurately enough. In fact, statistical convergence may require the total number of particles to be two orders of magnitude greater than the number of mesh elements [51]. This can become problematic in LES applications where the mesh is typically quite fine.

Another approach is the Eulerian Stochastic Fields (ESF) method. Here,  $\tilde{P}$  is decomposed into  $N$  stochastic fields as

$$\tilde{P}(\Psi) = \frac{1}{N} \sum_{n=1}^N \prod_{\alpha=1}^{N_\alpha} \delta(\Psi_\alpha - \zeta_\alpha^n), \quad (3.24)$$

where  $\zeta_\alpha^n$  is the  $n$ -th realisation of the stochastic field corresponding to the scalar with index  $\alpha$ .

The field evolves according to the formulation of Valiño et al. (2016) [94]

$$\begin{aligned} & d\tilde{\rho} \zeta_\alpha^n + \frac{\partial (\tilde{\rho} \tilde{u}_i \zeta_\alpha^n)}{\partial x_j} dt - \frac{\partial}{\partial x_j} \left( \left( \frac{\bar{\mu}}{Sc} + \frac{\mu_{SGS}}{Sc_{SGS}} \right) \frac{\partial \zeta_\alpha^n}{\partial x_j} \right) dt \\ & = \tilde{\rho} \left( \frac{2\mu_{SGS}}{\bar{\rho} Sc_{SGS}} \right)^{1/2} \frac{\partial \zeta_\alpha^n}{\partial x_j} dW_j^n - \frac{\bar{\rho}}{2\tau_{SGS}} (\zeta_\alpha^n - \tilde{\phi}_\alpha) dt - \tilde{\rho} \tilde{\omega}_\alpha^n (\zeta_\alpha^n) dt \end{aligned} \quad (3.25)$$

The Wiener term can be approximated using a random dichotomic vector with zero mean,  $\gamma = -1, 1$ , as a weak first-order approximation for the standard normal distribution. The second term on the RHS represents micro-mixing and is closed using the Interaction by Exchange with the Mean (IEM) model as is commonly done [51] [38].

The original method transports all species fractions [41][43][49]. However, as this is computationally very expensive, it can be combined with chemistry tabulation. In such a hybrid method, only a few controlling variables are transported and the tabulation can be made using, inter alia, REDIM [51] or FGM [38]. This reduction makes the method an attractive option.

In conclusion, statistical approaches can handle complex chemical reactions and kinetics more effectively than some other approaches, making them suitable for cases with detailed chemical mechanisms or when an accurate prediction of species concentrations and reaction pathways is important. The reason for this is that they make less strong assumptions on the flame structure than the other two approaches. However, this comes at the price of an increased computational cost and more complicated implementation.

### 3.3. Hydrogen flame experiments

The scarcity of literature on hydrogen-air flame experiments compared to methane-air flames can be linked to various reasons. Primarily, methane, as the main component of natural gas, finds extensive use in numerous industries like power generation, heating, and chemical synthesis. This wide range of applications drives more research into understanding methane's combustion characteristics. In contrast, experiments involving hydrogen are often more expensive, largely due to the technical complexities and safety concerns associated with its storage and handling. These challenges include managing hydrogen's highly flammable nature and its tendency to leak because of its small molecular size. As a result of these factors, researchers studying hydrogen flames frequently rely on a limited number of past experiments. This reliance is partly due to the higher costs and logistical hurdles in conducting new studies. Therefore, while there is growing interest in hydrogen's potential, these practical challenges have led to a more limited body of research compared to that of methane-air flame studies. The most important of these experiments in the context of aircraft engine combustors are discussed below.

#### 3.3.1. Swirl burner

A low-swirl burner is a combustion system utilized across various industrial sectors, including power generation, heating, and emissions management. This system is engineered for high combustion efficiency, minimal emissions, and versatile fuel adaptability. In CFD research, low-swirl burners are studied to dissect their combustion dynamics and enhance operational efficiency. These burners incorporate a relatively low degree of rotational motion, or swirl, within the combustion chamber. This design approach ensures that the air-fuel mixture maintains a low tangential velocity, producing a stable, evenly distributed flame with low turbulence. Characteristically, low-swirl burners generate a consistent, diffusion-based flame, making them ideal for scenarios where flame steadiness and even temperature distribution are critical. They are frequently employed in industrial heating applications. Low-swirl technology is particularly effective in contexts requiring stable, gentle flames, such as in household gas stoves, water heaters, and certain industrial heaters. Examples of studies on hydrogen low-swirl burners are [95][96][97].

In aircraft engines, however, there are stricter requirements regarding combustion efficiency, emissions and physical dimensions. For that reason, high-swirl type burners are preferred. High swirl burners generate a significantly higher level of swirl within the combustion chamber. The air and fuel mixture is imparted with a high tangential velocity, leading to intense turbulence and enhanced mixing. They create a highly turbulent, premixed flame that promotes rapid combustion and efficient mixing of fuel and air. The higher swirl creates a local low-pressure zone that forces some of the combustion products to recirculate. This makes the flames significantly harder to model due to the detailed, fully coupled, turbulent fluid mechanics and chemical kinetics. A comparison between the solvers is shown in Figure 3.1.

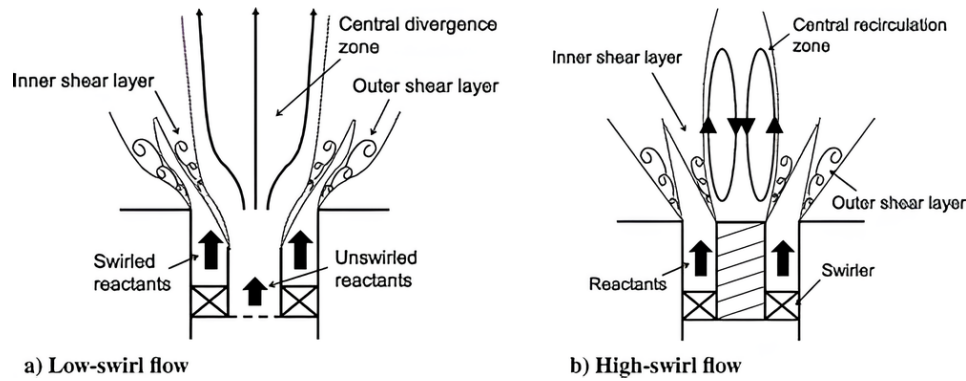


Figure 3.1: Diagram of low-swirl and high-swirl burners (Adapted from [98])

### 3.3.2. Cabra flame

The recirculation of products in a high-swirl burner makes it difficult to test a new model on. However, it is necessary to validate whether the model is able to capture similar chemical kinetics, heat transfer and molecular transport as in a practical combustor. Ideally, an experiment needs to address flame stabilization in combustion products, while decoupling the chemical kinetics from the complex recirculating flow. The aim of the Cabra flame is to design such a set-up that mimics the coupling of chemical kinetics and turbulent mixing typically seen in the recirculation zone of a combustor, without having to deal with the complexity of recirculating flow. This is achieved by surrounding a central  $H_2/N_2$  jet with a co-flow of lean premixed  $H_2$ /air flame, leading to a lifted jet flame. A schematic of the set-up is given in Figure 3.2. This flame has been given several names in the past, but the choice is made to refer to it in this work as the Cabra flame.

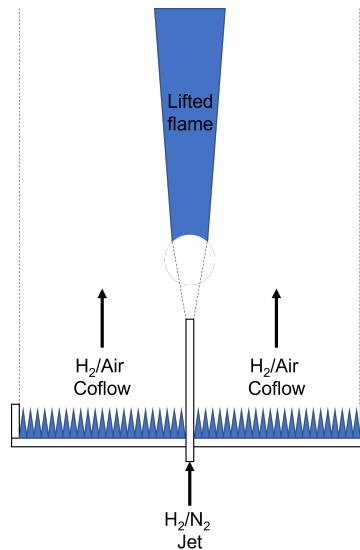


Figure 3.2: Schematic of lifted turbulent jet flame in vitiated coflow (Cabra flame)

The flame has a number of additional properties that make it a suitable validation case, before moving towards a realistic combustor domain. It has hydrogen as only fuel and air as oxidiser. Although technically the hydrogen is diluted with nitrogen, it is absent from the main oxidation reaction chain and is not regarded as fuel. The flame is fully turbulent and it is stabilised using a vitiated co-flow, which leads to a lifted flame. This stabilisation mechanism anchors the hydrogen flame through auto-ignition and is significantly easier to implement than, for example, stabilisation through recirculation. The geometric dimensions of the burner and its boundary conditions are clearly defined and a number of experimental studies provide data on the velocity and temperature profile, and concentrations of

the major species. Furthermore, it has been studied extensively in the literature before. An overview of this literature is given next. As it is the only turbulent partially premixed hydrogen with published experimental data available, it also serves as a review of this specific type of flame.

#### Usage in literature

The burner was originally proposed by Cabra et al. in 2002 [99]. In this work, they present an experimental and numerical investigation. For their experimental study, they use simultaneous measurements of the temperature profile and concentrations of the major species OH and NO through the combination of Raman and Rayleigh scattering, and laser-induced fluorescence. The numerical study consists of two RANS simulations using an EDC model and a TPDF-PMC model. Gordon et al. (2005) [100] further investigate the experimental set-up, with a focus on flame stability characteristics, by changing the flow conditions. They also collect new data on stabilisation and velocity.

Numerous numerical studies on the Cabra burner using RANS have been conducted [101][102][103][104][105][106][107][108]. Literature on LES of the Cabra flame is more sparse and recent due to the higher computational costs.

Jones and Navarro-Martinez (2007) [39] is the first work that models the Cabra flame in an LES framework. The focus is on modelling auto-ignition events. A dynamic Smagorinsky SGS model is used in conjunction with an ESF method on all of the reacting scalars. The detailed chemistry mechanism of Yetter [65] for H<sub>2</sub>-air combustion is adopted. It consists of 9 species and 19 reactions. They come to a good agreement with the experimental data. The results show to be sensitive to the co-flow temperature. It is also discovered that the radical HO<sub>2</sub> is a key intermediate species as it is a source of ignition kernels and pools of radicals are formed near the base of the flame. A follow-up paper published in 2008 [109] uses the same choice of models, but focuses on a parametric study of the jet velocity and co-flow temperature. They are able to reproduce the correct ignition lengths in different regimes without any adjustment or calibration of the model constants. With that, they prove that their results are essentially independent of SGS model parameters. The method is suggested to be attractive for complex combustion problems.

Navarro-Martinez and Kronenburg (2011) [42] take a different approach. While they also choose the dynamic Smagorinsky model and the same detailed chemistry mechanism of Yetter [65], they use a CMC method to model flame-turbulence interaction. They show successful results in predicting flame ignition and stabilisation, however, they indicate that their work lacks accurate modelling of the competition between turbulent quenching and flame propagation at the anchor point. They conclude that their LES-CMC accurately predicts auto-ignition, but not extinction and that the averaging effects of CMC prevent instant response and accurate computation of the local correlations between chemistry, velocity and mixing.

Stanković et al. (2013) [45] aim to illustrate that their LES-CMC approach is viable for a range of different auto-ignition regimes. They also do a sensitivity study of the lift-off height to different co-flow temperatures and velocities, while comparing different chemistry mechanisms. The standard Smagorinsky model is used with three different chemistry mechanisms: Yetter [65], Mueller [66] and Li [67]. They all consist of 9 species and 19 reactions but with different parameters. They are able to well reproduce the following global trends in experimental observations: a decreased auto-ignition length with an increase in co-flow temperature, and an increased auto-ignition length with an increase in co-flow velocity. They also conclude that the choice of chemistry mechanism is important and that although they show similar qualitative behaviour, different boundary conditions are necessary to yield the same ignition length.

Han et al. (2016) [110] opt for a TPDF approach again. However, they choose to utilise a PMC method. They combine this with a dynamic Smagorinsky model and an ISAT method based on the detailed chemistry mechanism of Li [67]. They implement a new IEM model that includes differential diffusion and a dynamic model for scalar mixing time-scale. This leads to a better prediction of major species mass fractions, temperatures and lift-off heights compared to the standard IEM model. The conclusion is made that major species mass fractions, temperatures and lift-off heights are very sensitive to differential diffusion.

More recently, Benim et al. (2019) [50] used a PFDF approach with FGM tabulation based on the detailed chemistry mechanism of Li [67]. The WALE model is used as the SGS model. They come to

comparable results to Jones and Navarra (2007) [39] with a lower computational cost. They demonstrate the predictive capability of FGM as a very cost-effective method to predict lifted hydrogen flames.

Within the combustion group of TU Delft, Ferrante et al. (2023) [111] have worked on a PFDF method using the DRM-19 mechanism [70]. The one-equation transported eddy-viscosity model is used for the SGS stresses. The sensitivity of the lifted flame to differential diffusion is investigated and it is found that the flame lift-off height is highly sensitive to the diffusion model used in the chemistry tabulation, although no clear winner is identified. The goal and set-up of this research are very similar to this master's thesis project. A lot of cooperation with this group of researchers has, therefore, happened and they have laid a lot of the groundwork for this project.

Thus, the FC-ESF method has shown the best results so far. However, it comes at a significant computational cost. A cost that can become prohibitively high when moving towards bigger domains. The FGM-PPDF method has been shown to reduce these costs and get comparable results. However, a set of more restrictive assumptions has to be made. Combining FGM tabulation with the ESF method has not been attempted before for partially premixed hydrogen flames. This hybrid model is selected as a numerical model for this thesis.

## 3.4. Selected model and research questions

The objective of this thesis is to develop an advanced numerical model for hydrogen combustion, specifically tailored for hydrogen aircraft combustors. This model aims to effectively simulate a broad spectrum of combustion scenarios, encompassing both premixed and non-premixed conditions. It is designed to handle the complexities of fully turbulent environments, typical of aircraft combustors, and accurately capture the distinct characteristics of hydrogen combustion, such as its rapid flame speeds and differential diffusion properties.

Key to the model's utility is its adaptability to further investigate various aspects of hydrogen combustion in future extensions. This includes, *inter alia*, studying ultra-lean burn approaches, understanding the formation processes of  $\text{NO}_x$ , and analyzing the impact of high strain rates on combustion. The model's design balances predictive precision with manageable computational demands. This equilibrium is crucial to ensure that the model is not only detailed in its analysis but also practical for use in ongoing research and development in the field of hydrogen-powered aircraft engines.

The optimal approach to meet these requirements is the integration of the Eulerian Stochastic Fields (ESF) method with the Flamelet Generated Manifold (FGM) tabulation, forming the FGM-ESF methodology. For validation purposes, the Cabra flame has been identified as the most fitting test case. The rationale behind these choices has followed from the literature study and is summarised next.

### Chosen model

The selected model is a combination of the Eulerian Stochastic Fields (ESF) method and Flamelet Generated Manifold (FGM) tabulation. Unlike many other models that make predefined assumptions about the flame structure or the statistical behaviour of key variables, the ESF method avoids these simplifications. It introduces stochastic terms to describe the subgrid-scale interactions between the flame and turbulence. This stochastic approach enables the ESF method to capture the random and chaotic nature of turbulence more accurately than most other models. Phenomena like local flame extinction and reignition are particularly challenging in turbulent combustion. These occur due to the intricate interplay between chemical reactions, heat release, and turbulent flow, which can significantly alter the flame structure and behaviour. The ESF method's stochastic nature allows it to capture these phenomena more realistically, as it can account for the randomness and fluctuations in turbulent flows, enhancing its effectiveness in modelling real-world combustion scenarios.

While the Eulerian Stochastic Field (ESF) method offers enhanced detail and accuracy in modelling flame-turbulence interactions, it also demands greater computational resources. To address this, the model incorporates Flamelet Generated Manifold (FGM) tabulation. FGM streamlines the computational process by focusing on a limited set of key controlling variables. This approach allows for the use of detailed chemical mechanisms at the flamelet level, which are then integrated into the solver through these controlling variables. These variables are not only straightforward to implement but also physically interpretable, which makes post-processing easier. Moreover, the FGM framework is designed for flexibility, enabling easy incorporation of additional controlling variables to capture specific phenomena. This includes aspects like  $\text{NO}_x$  formation, differential diffusion, and the influence of strain on combustion. An added benefit of FGM is that it eliminates the need for assumptions about the PDF shape for these controlling variables, simplifying the extension of the model. This integration of FGM with ESF thus balances the model's computational intensity with its ability to accurately simulate intricate combustion processes.

The starting point for the model is the ESF-REDIM implementation of Breda [51] which has been validated for partially premixed methane-air flames.

### Chosen case

As a validation case, the Cabra flame [99] is chosen. This lifted turbulent  $\text{H}_2/\text{N}_2$  jet flame in a vitiated co-flow has been well studied in the literature and has a number of desirable characteristics. The Cabra flame is a fully turbulent, partially premixed hydrogen-air flame. This specific nature of the flame closely mimics the combustion regimes found in actual combustors, where there is a significant interaction between chemical kinetics and turbulent mixing. Unlike high-swirl burners, the Cabra flame does not

possess regions of recirculating flow. Recirculation adds complexity to combustion modelling due to the additional turbulent structures and flow patterns it introduces. The absence of such recirculating flows in the Cabra flame simplifies the modelling process, making it an ideal case for initial validation. Its characteristics position the Cabra flame as an ideal intermediary test case. It offers enough complexity to test and validate the model's ability to handle real-world combustion scenarios while being less complicated than scenarios with recirculating flows. This makes it a suitable precursor before advancing the model to more complex and practical combustor simulations.

### Research questions

The novelty of this thesis lies in the application of the hybrid FGM-ESF approach on a fully turbulent partially premixed hydrogen flame. This has not been done before on this type of flame, to the best of the author's knowledge. Consequently, the primary goal of this thesis is to develop the code and assess the effectiveness of the FGM-ESF method in this application. This evaluation is conducted through a detailed comparative analysis with the more established but computationally intensive classical ESF method that transports all species. The thesis aims to answer the following questions:

- How does FGM-ESF compare to a more expensive FC-ESF model in terms of predictive accuracy?
- How does FGM-ESF compare to a more expensive FC-ESF model in terms of computational costs?

# 4

## Paper

This chapter includes research done in this thesis in academic paper format. The paper is a standalone document that presents the methodology and results.

# Eulerian stochastic field method with FGM tabulation for partially premixed hydrogen flames

V.H. Vloeberghs

## Abstract

In this study, a Large Eddy Simulation (LES) is applied to a partially premixed turbulent lifted hydrogen flame using the Eulerian Stochastic Fields (ESF) method for modelling the subgrid turbulence-flame interactions. A newly developed hybrid model (FGM-ESF) that uses tabulated thermochemistry and only transports a progress variable and mixture fraction is introduced as a cost-effective alternative to the classic ESF approach (FC-ESF) that transports all species. Both models are evaluated for their predictive accuracy and computational efficiency. Results show that both models align well with experimental data in terms of the first statistical moments of velocity, mixture fraction, and temperature, even with a limited number of fields. The FGM-ESF method, however, tends to slightly overestimate the second statistical moment of the mixture fraction due to slower mixing. It also predicts higher peak temperatures and water vapour mass fractions compared to the FC-ESF method. Despite these minor differences, the FGM-ESF model successfully captures the essential qualitative aspects, including the prediction of super-adiabatic conditions and a double-peak pattern in conditional reaction rates. Furthermore, the computational cost of the FGM-ESF model is less impacted by the number of stochastic fields compared to the FC-ESF, offering the potential for enhanced performance through the refinement of the interpolation routine. Through these characteristics, it positions itself as a viable alternative to the FC-ESF method for more extensive and practical applications in partially premixed hydrogen flames.

**Keywords:** Eulerian Stochastic Field, Partially Premixed Hydrogen Flame, Large Eddy Simulation, Flamelet Generated Manifold

## 1 Introduction

Hydrogen is often presented as a carbon-free alternative fuel in the aviation industry, recognised for its high specific energy and producibility through renewable energy [1][2][3][4]. When combusted in a gas turbine, hydrogen can generate sufficient power to propel jet aircraft [5], typically tens of megawatts. However, transitioning to hydrogen

comes with its own set of challenges. The high flame temperature of hydrogen-air combustion results in increased emissions of harmful nitric oxides ( $\text{NO}_x$ ) through the thermal pathway [6]. An emerging mitigation technique uses the wide flammability range of hydrogen to burn at ultra-lean combustion regimes to reduce the operating temperature [7][8]. However, this technology is still in its infancy and requires tools tailored to address hydrogen's unique properties, such as its high diffusivity and flame speed, which lead to increased risk of flashback and thermo-diffusive instabilities [9].

A pivotal tool in numerical combustion research is Large Eddy Simulation (LES). This computational method is used to model turbulent flows by only resolving the large-scale turbulent structures directly. The influence of the smaller, SubGrid Scales (SGS) is modelled [10]. In doing so, LES balances the computational efficiency of Reynolds-Averaged Navier-Stokes (RANS) methods and the accuracy of Direct Numerical Simulations (DNS). For a deeper understanding of ultra-lean combustion regimes, it is crucial to tailor an LES model for hydrogen combustion. Such a method should not only capture detailed and time-dependent flow phenomena to study turbulent mixing and flame stability but also account for the impacts of preferential diffusion, all while maintaining computational efficiency suitable for simulating large-scale practical combustors. Two modelling choices have been given the most attention in the literature.

The first is the chemical mechanism. Modelling the combustion process in an LES requires the description of chemical kinetics. Choosing a detailed mechanism that solves all reactions for the complete set of species offers the most accurate representation of chemistry. However, it means that each species is transported through a separate conservation equation. Furthermore, the chemical balance equations require an Ordinary Differential Equation (ODE) to be solved for every reaction in every mesh cell at every timestep. A way to reduce computational costs is to use a tabulated chemistry technique based on the flamelet assumption. It states that a multidimensional turbulent flame can be described by a collection of one-dimensional laminar flame elements, called flamelets. These flamelets can be cheaply pre-computed for various conditions and stored in a table. In the LES solver loop, the process retrieves the relevant conditions through only a few controlling variables. This approach streamlines the process, focusing only on conservation equations for these specific variables. As a result, this method effectively reduces the total number of variables involved in transport. Examples of these methods are FPV [11] and FGM [12].

The second concerns subgrid scale flame-turbulence interaction. Combustion happens at the subgrid scales, where turbulence and chemistry interact closely. As the flow is not resolved at those levels, an SGS flame-turbulence interaction model is needed. There are multiple approaches to address this problem. In this work, a statistical approach is taken because it does not require strong assumptions on flame shape [13]. The effects of the SGS fluctuations on either the full set of species or the set of selected controlling variables are modelled through a one-point, one-time Probability Density Function (PDF). The characteristics of the PDF have to be determined. In case of very few controlling variables, a simpler strategy is to assume the shape of the PDF a-priori. This is called the Presumed PDF (PPDF) approach. In the turbulent combustion literature, the FGM tabulation method is almost exclusively integrated

with PPDF. However, the method requires strong assumptions regarding the shape and statistical independence of the scalar distributions [14]. A more general approach is to solve a transport equation for the PDF instead. It is called the Transported PDF (TPDF) approach. The transport equation is typically solved using a Monte Carlo simulation to recover the statistical moments.

The Lagrangian Stochastic Particles Method (LSPM) uses an ensemble of stochastic particles to capture the discrete representation of the PDF. Each cell has a separate Monte Carlo simulation that models these particles, factoring in convection, molecular mixing, turbulent diffusion, and chemical reactions. To ensure statistical convergence, the number of particles must be considerably higher, often two orders of magnitude greater than the mesh elements [15]. This poses challenges in LES applications with fine, three-dimensional grids. Furthermore, a mechanism to relay information from the Lagrangian to the Eulerian mesh is needed. An alternative way to perform the Monte Carlo simulation is to decompose the SGS PDF in a number of stochastic fields resulting in a set of Stochastic Partial Differential Equations (SPDE). This is the so-called Eulerian Stochastic Field (ESF) method and is the focus of this work. These continuous fields, spanning the entire domain, are spatially differentiable and temporally continuous, though not time-differentiable. This means that there are no spatially varying sampling errors [14], requiring only a small number of fields (up to 8 [16]) to accurately capture the statistical moments. Furthermore, in contrast to the LSPM, the mesh-based Eulerian solvers in OpenFOAM can be used directly to solve the PDF transport equations. The method is typically combined with a detailed or reduced chemical mechanism, where the fields represent the mass fractions and the enthalpy. Recently, there has been an increasing focus on hybrid methods that utilize tabulated chemistry and transport only a select few controlling variables. These approaches show promise in significantly reducing computational costs while still preserving predictive accuracy [14] [15].

When modelling hydrogen combustors, it is crucial to operate in a wide range of regimes, encompassing high turbulence scenarios and accommodating both premixed and non-premixed burning modes. While there are existing studies on partially premixed hydrogen flames that use PPDF with FGM tabulation (FGM-PPDF) [17], ESF with fully transported chemistry (FC-ESF) [18] or alternative TPDF [19] methods, there is a noticeable gap in the literature regarding the use of an FGM-ESF solver for hydrogen flames. This research aims to fill this gap by focusing on the development and evaluation of an FGM-ESF model specifically for partially premixed hydrogen flames. The study assesses the method’s predictive accuracy and computational efficiency in comparison to the more resource-intensive FC-ESF solver.

The paper is structured as follows. In [section 2](#), the different parts of the model are explained, consisting of the LES, chemistry description and turbulence-flame-interaction. In [section 3](#), the validation case and the numerical implementation are described. The results of both versions of the solver are compared to experimental results and their computational efficiencies are shown in [section 4](#). The most important conclusions are given in [section 5](#).

## 2 Modelling approach

### 2.1 Large eddy simulation

Only the largest scales of turbulence are resolved in an LES. The effect of the smaller, subgrid scales is modelled. The resolved and subgrid scales are separated by applying a filtering operation to the conservation equations. Consider a top-hat filter  $\mathcal{G}(x - x')$ , which corresponds to averaging over a box, on a spatially and temporally varying variable  $q$ . The filtered variable becomes

$$\bar{q}(x) = \int q(x') \mathcal{G}(x - x') dx'. \quad (1)$$

Filtering is done implicitly in the calculations through the numerical grid, i.e. scales smaller than the cell width are not captured.

Strong density fluctuations are not uncommon in combustion simulations. The mass-weighted Favre filtering is often applied to prevent additional unclosed terms. It is defined for variable  $q$  by

$$\tilde{q} = \frac{\bar{q}\bar{\rho}}{\bar{\rho}}, \quad (2)$$

However, it is important to note that Favre filtering is not considered the primary filter mechanism for LES, as it does not separate the scales. Rather it serves as an auxiliary tool to aid the simulation of compressible turbulent flows.

Filtering the conservation equations for mass, momentum, enthalpy and species gives the following set of equations:

- Conservation of mass:

$$\frac{\partial \bar{\rho}}{\partial t} + \frac{\partial \bar{\rho} \tilde{u}_i}{\partial x_i} = 0 \quad (3)$$

- Conservation of momentum:

$$\frac{\partial \bar{\rho} u_i}{\partial t} + \frac{\partial \bar{\rho} \tilde{u}_i \tilde{u}_j}{\partial x_i} = - \frac{\partial \bar{p}}{\partial x_i} + \frac{\partial}{\partial x_i} \left( \underbrace{\bar{\tau}_{ij}}_{(r.1)} - \bar{\rho} \underbrace{(\widetilde{u_i u_j} - \tilde{u}_i \tilde{u}_j)}_{(u.1)} \right) \quad (4)$$

- Species transport (for  $m = [1, \dots, n_s]$  species):

$$\frac{\partial \bar{\rho} \tilde{Y}_m}{\partial t} + \frac{\partial \bar{\rho} \tilde{u}_i \tilde{Y}_m}{\partial x_i} = \frac{\partial}{\partial x_i} \left( \underbrace{\bar{V}_{mi} Y_m}_{(r.2)} - \bar{\rho} \underbrace{(\widetilde{u_i Y_m} - \tilde{u}_i \tilde{Y}_m)}_{(u.2)} \right) + \underbrace{\bar{\omega}_m}_{(s.1)} \quad (5)$$

- Enthalpy balance:

$$\frac{\partial \bar{\rho} \tilde{h}_s}{\partial t} + \frac{\partial \bar{\rho} \tilde{u}_i \tilde{h}_s}{\partial x_i} = \frac{\partial}{\partial x_i} \left( \underbrace{\lambda \frac{\partial T}{\partial x_i}}_{(r.3)} - \bar{\rho} \underbrace{(\widetilde{u_i h_s} - \tilde{u}_i \tilde{h}_s)}_{(u.3)} \right) + \underbrace{\bar{\omega}_T}_{(s.2)} \quad (6)$$

where  $p$  denotes the pressure,  $h_s$  the sensible enthalpy,  $Y_m$  the mass fraction of species  $m$ ,  $V_{mi}$  the local diffusion velocity in direction  $i$  of species  $m$ , and  $\lambda$  the thermal conductivity.

Filtering the conservation equations leads to 8 unclosed terms which can be classified into one of three types: resolved, unresolved and source terms. The resolved unclosed term,  $(r,1)$  is closed through the gradient diffusion hypothesis for Newtonian fluids. The other resolved terms,  $(r,2)$  and  $(r,3)$ , are closed through a simple gradient approximation. The same approximation is used for the last two unresolved terms,  $(u,2)$  and  $(u,3)$ . Sutherland’s law for nitrogen gas is used ( $A_s = 1.67212 \cdot 10^{-6}$  and  $T_s = 170.672$ ) in conjunction with constant Schmidt and Prandtl numbers ( $Sc = Pr = 0.7$ ) to obtain the diffusivity coefficients. Soret and Dufour effects are assumed to be negligible. The (unresolved) Reynold stresses,  $(u,1)$ , are closed using a subgrid-scale stress model. Two types of eddy viscosity models are used: WALE [20] and  $k$ -equation transported eddy viscosity model [21]. The results appear to be weakly sensitive with regard to the choice of the model, as seen in Appendix D.

Closing the filtered source terms,  $(s,1)$  and  $(s,2)$ , requires two types of models. The first model is for the unfiltered source term  $\dot{\omega}_m$ . The chemistry can either be obtained by solving the chemical kinetics for all species directly, or by using a chemistry reduction technique. This is the focus of subsection 2.2. The enthalpy source term  $\bar{\omega}_T$  is obtained by calculating the enthalpy of formation of the mixture from the JANAF thermochemical tables. The second model is for the turbulence-chemistry interaction at the subgrid scales. This effect can not simply be neglected, i.e.  $\bar{\omega}_m \neq \dot{\omega}_m(\bar{T}, \bar{Y}_m)$ . The reason is the highly non-linear behaviour of chemical reaction rates. A transported PDF method is used to obtain the source terms. It is explained in subsection 2.3.

## 2.2 Chemistry description

The chemical source term  $\dot{\omega}_m$  is obtained through two different methods: the first involves directly solving the chemical kinetics (full chemistry), which serves as the benchmark; the second approach utilizes a tabulation method based on flamelet solutions, known as Flamelet Generated Manifolds (FGM), representing the newly-developed method.

The first method solves the ODEs corresponding to the different reactions directly in the solver loop. It needs two state variables and the mass fractions of the species  $\mathbf{Y}$ , i.e.  $\dot{\omega}_m = f(p, T, \mathbf{Y})$ . For the set of species and reactions, the San Diego [22] and Ó Conaire [23] chemistry mechanisms for hydrogen-air combustion are selected. They both have 10 species and 21 reactions but have different reaction rate coefficients. It is a computationally expensive method as a set of ODEs has to be solved in each cell for every timestep. The other method reduces the computational load by using the relation between all chemical variables from pre-calculated results and simplifying them by a selected set of controlling variables.

The second method rests on two assumptions. The first is (time) scale separation. It states that fast reaction time scales can be decoupled from the slow reaction time scales. This means that the fast time scales are assumed to be steady-state and the reactions corresponding to the slow time scales are used to construct a low-dimensional manifold. The manifold is described by a small number of coordinates. The second

assumption is the flamelet assumption which states that a multidimensional turbulent flame can be described by a collection of one-dimensional laminar flame elements, called flamelets. These flamelets can easily be modelled for a range of conditions. Their characteristics can be stored in the data table and accessed through the set of coordinates, i.e. controlling variables. The method is called Flamelet Generated Manifold [24].

The flamelets are a set of premixed one-dimensional flames for different equivalence ratios within the flammability limit. They are solved in CHEM1D using the San Diego and Ó Conaire mechanisms. The controlling variables are the normalised progress variable  $c$  and (Bilger) mixture fraction  $Z$ . They are calculated from the mass fractions of the species as

$$c = \frac{Y_{\text{H}_2\text{O}} - Y_{\text{H}_2\text{O}}^{eq}}{Y_{\text{H}_2\text{O}}^0 - Y_{\text{H}_2\text{O}}^{eq}} = \frac{Y_{\text{H}_2\text{O}} - Y_{\text{H}_2\text{O}}^{eq}}{\theta_c} \quad (7)$$

$$Z = \frac{0.5W_{\text{H}_2} (Z_{\text{H}} - Z_{\text{H}}^O) - W_{\text{O}_2}^{-1} (Z_{\text{O}} - Z_{\text{O}}^O)}{0.5W_{\text{H}_2} (Z_{\text{H}}^F - Z_{\text{H}}^O) - W_{\text{O}_2}^{-1} (Z_{\text{O}}^F - Z_{\text{O}}^O)}, \quad (8)$$

where 0 and  $eq$  represent the initial reactants and the equilibrium state of the products, respectively.  $W_m$  signifies the molar weight of species  $m$ , while  $Z_{\text{H}}$  and  $Z_{\text{O}}$  denote the elemental mass fractions of hydrogen and oxygen. The superscripts  $O$  and  $F$  are used to indicate the oxidizer (coflow) and the fuel stream.

## 2.3 Turbulence-flame-interaction

### 2.3.1 Transported PDF

To model the subgrid-scale flame-turbulence interaction, the approach based on [14] and [15] is followed.  $\phi_\alpha$ , which is either a thermochemical variable in the case of full chemistry, or a controlling variable in the case of FGM, can be described by the one-point one-time fine-grained PDF  $\mathcal{P}_\alpha$  as

$$\mathcal{P}_\alpha(\Psi_\alpha; x_i, t) = \delta(\Psi_\alpha - \phi_\alpha(x_i, t)), \quad (9)$$

where  $\Psi_\alpha$  denotes the sample space of  $\phi_\alpha$  and  $\delta$  the Dirac function. This is the marginal PDF for  $\phi_\alpha$ . Combining the marginals of all variables, and applying LES (Equation 1) and Favre (Equation 2) filtering leads to the density-weighted joint sub-grid PDF function  $\tilde{\mathcal{P}}_{sgs}(\Psi)$ , also called the Filtered Density Function (FDF). It describes the probability that the state vector  $\phi$  falls between the sample space  $\Psi$  and  $\Psi + d\Psi$  for different realisations of  $\phi$  in the filter volume [14]. The derived FDF satisfies the transport equation

$$\begin{aligned}
& \frac{\partial \bar{\rho} \tilde{\mathcal{P}}_{sgs}}{\partial t} + \frac{\partial \bar{\rho} \tilde{u}_j \tilde{\mathcal{P}}_{sgs}}{\partial x_j} + \sum_{\alpha=1}^n \frac{\partial}{\partial \psi_\alpha} \left( \bar{\rho} \dot{\omega}_\alpha \tilde{\mathcal{P}}_{sgs} \right) \\
&= \frac{\partial}{\partial x_j} \left[ \left( \frac{\bar{\mu}}{Sc} + \frac{\mu_{sgs}}{Sc_{sgs}} \right) \frac{\partial \tilde{\mathcal{P}}_{sgs}}{\partial x_j} \right] - \sum_{\alpha=1}^n \sum_{\beta=1}^n \frac{\partial^2}{\partial \psi_\alpha \partial \psi_\beta} \left( \frac{\bar{\mu}}{Sc} \frac{\partial \phi_\alpha}{\partial x_i} \frac{\partial \phi_\beta}{\partial x_i} \Big|_{\phi=\psi} \tilde{\mathcal{P}}_{sgs} \right),
\end{aligned} \tag{10}$$

A complete derivation of this equation is given in [25].

The source term  $\dot{\omega}_\alpha$  appears in closed form. This allows direct look-up from the database for the FGM tabulation. The last term represents the micro-mixing term and can be closed by the Interaction by Exchange with Mean(IEM) [14] as

$$\frac{\bar{\rho}}{\tau_{sgs}} \sum_{\alpha=1}^{n_s} \frac{\partial}{\partial \psi_\alpha} \left[ \left( \psi_\alpha - \tilde{\phi}_\alpha \right) \tilde{\mathcal{P}}_{sgs} \right] \tag{11}$$

where the subgrid time scale  $\tau_{sgs}$  is defined as

$$\frac{1}{\tau_{sgs}} = C_d \frac{\nu_{sgs}}{\Delta^2}. \tag{12}$$

$\tau_{sgs}$  is a function of the SGS mixing constant  $C_d$ , which is typically set to 2 [16], the (kinematic) eddy viscosity  $\nu_{sgs}$  and the filter width  $\Delta$ , which is the same as the cell width in this case. Equal diffusivities are assumed in the equations at both the resolved and SGS levels. However, for this case, the flamelet calculations sufficiently include the effects of differential diffusion, primarily due to turbulent diffusion being more dominant than molecular diffusion at high Reynolds numbers. For situations where differential diffusion effects are more pronounced, alternative approaches exist. At the resolved scales, FC-ESF can accommodate different diffusivities (or Schmidt numbers) for each species. In the context of FGM-ESF, Mukundakumar et al. [26] introduce an additional tabulated term to address the impact of unequal Lewis numbers on the diffusion of controlling variables. At the SGS scale, Han et al. [19] enhance the IEM model by adding a mean drift term to account for differential diffusion. This modification alters the original IEM stochastic diffusion term in physical space to diffusion in composition space.

The PDF transport equation is not solved deterministically due to the high dimensionality of the joint PDF, as that would lead to high computational costs. Instead, a Monte Carlo simulation is used to recover the statistical moments.

### 2.3.2 Eulerian Stochastic Fields

The Monte Carlo formulation based on Eulerian Stochastic Fields, as proposed by Jones and Navarro-Martinez [27] is used. The SPDE that represents the evolution of the  $n$ th realisation of the field  $\zeta_\alpha$  is given by

$$\begin{aligned}
& d\bar{\rho}\zeta_\alpha^n + \frac{\partial(\bar{\rho}\tilde{u}_i\zeta_\alpha^n)}{\partial x_j} dt - \frac{\partial}{\partial x_j} \left( \left( \frac{\bar{\mu}}{Sc} + \frac{\mu_{sgs}}{Sc_{sgs}} \right) \frac{\partial\zeta_\alpha^n}{\partial x_j} \right) dt \\
& = \bar{\rho} \left( \frac{2\mu_{sgs}}{\bar{\rho}Sc_{sgs}} \right)^{1/2} \frac{\partial\zeta_\alpha^n}{\partial x_j} dW_j^n - \frac{\bar{\rho}}{2\tau_{sgs}} (\zeta_\alpha^n - \tilde{\phi}_\alpha) dt + \bar{\rho}\omega_\alpha^n(\zeta^n) dt.
\end{aligned} \tag{13}$$

Note that the source term is again appearing in closed form. It is important to realise that  $\zeta_\alpha$  is not a physical realisation of the real field  $\phi_\alpha$ , but instead an equivalent stochastic system to [Equation 10](#). The SPDE is derived using Itô's integration and the full derivation can be found in Valiño et al. [\[28\]](#). This is the latest formulation where only the subgrid diffusion is included in the stochastic term to avoid unphysical fluctuations.

The stochastic process is driven by  $dW_j^n$ , which denotes the increments of the Wiener process. The Wiener process, or Brownian motion, is a random walk with normally distributed increments. The mean of the increments is zero and the variance is equal to the time increment, i.e.  $dW_j^n \sim N(0, dt)$ . These increments are different for each field but are spatially uniform. This prevents spatially varying sampling errors, in contrast to the LSPM, reducing statistical noise. However, using only a small number of fields can lead to significant differences between the theoretical and sample moments. For that reason, the first-order approximation  $dW_j^n = \gamma_j\sqrt{dt}$  is used.  $\gamma_j$  is a random dichotomic vector with values -1 or 1. To ensure a zero mean, a vector of  $N$  of alternating values is produced and is randomly shuffled. The Wiener process, and its approximation, are continuous but not differentiable in time. For that reason, [Equation 13](#) is given in terms of increments instead of the typical time derivative in the conservation equations. The stochastic fields, however, are spatially smooth. This means that the stochastic fields can be discretized at the grid-size length scale because they are smooth within the cell volume. This is a basic premise of the approach, meaning that the stochastic fields are fully resolved at the grid size level and do not contain any hidden sub-grid scales [\[14\]](#).

The FGM-ESF method has a number of advantages compared to the FGM-PPDF method. Aside from the lack of strong assumptions regarding PDF shape and statistical independence of the variables, another advantage is that the resolved values of the controlling variables do not need to be pre-integrated. Instead, they can be directly computed from the stochastic fields as

$$\tilde{\phi}_\alpha = \frac{1}{N} \sum_{n=1}^N \zeta_\alpha^n \text{ and } \phi_{\alpha,sgs} = \sqrt{\frac{1}{N} \sum_{n=1}^N \zeta_\alpha^n - \tilde{\phi}_\alpha^2}. \tag{14}$$

This means that no model equation is needed for the second moment in the tabulation. A model equation that is not always available. These advantages lead to more freedom in the selection and number of controlling variables. That makes the method flexible to be used on different combustion regimes and to study different phenomena related to novel hydrogen combustion techniques, e.g.  $\text{NO}_x$ , strain, etc.

It should be noted that using the normalised progress variable leads to an additional unclosed source term due to the definition of  $c$  depending on the mixture fraction. It

is defined as

$$\dot{\omega}_{np} = \rho \chi_Z (c/\theta_c) (d^2 \theta_c / dZ^2), \quad (15)$$

where  $\chi_Z = \mathcal{D} |\nabla Z|^2$  is the scalar dissipation rate of  $Z$ .  $\dot{\omega}_{np}$  was observed to be mainly negative and small in magnitude as compared to  $\dot{\omega}_c$  [29]. Since it appears in unclosed form, it is omitted for simplicity, although further considerations are discussed in section 4.

### 3 Validation case and numerical implementation

#### 3.1 Validation case

The code is validated on a turbulent partially premixed hydrogen flame. The case is the experimental set-up of Cabra *et al.* (2002) of a lifted turbulent  $H_2/N_2$  jet flame in a vitiated co-flow [30]. It has been called several names in the past, but the choice is made to refer to it in this work as the Cabra flame. The original aim of the Cabra flame is to design a set-up that mimics the coupling of chemical kinetics and turbulent mixing typically seen in the recirculation zone of a combustor, without having to deal with the complexity of recirculating flow. This is achieved by surrounding a central  $H_2/N_2$  jet with a co-flow of lean premixed  $H_2$ /air flame, leading to a lifted jet flame. A diagram of the set-up is given in Figure 1.

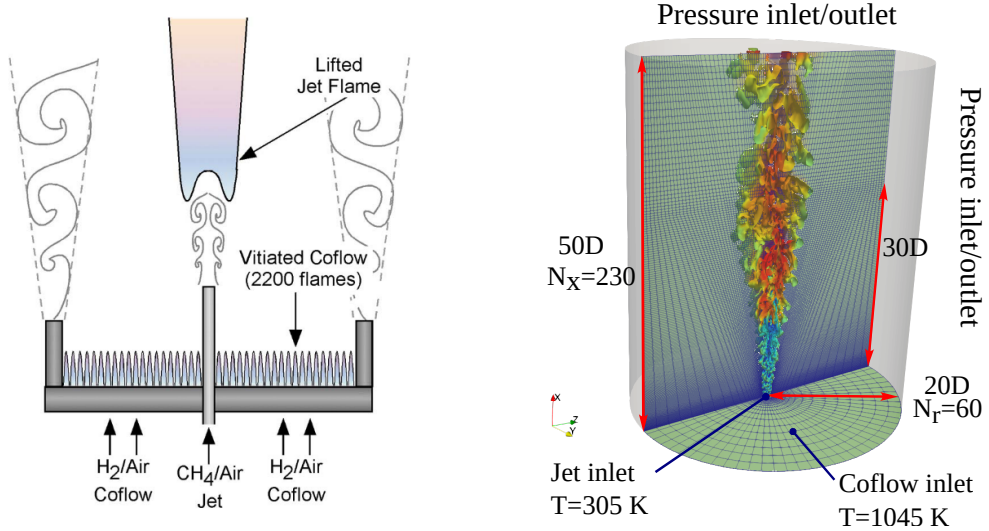


**Fig. 1:** Sketch of the lifted turbulent  $H_2/N_2$  jet flame configuration in vitiated co-flow of Cabra *et al.* [30] (left), and numerical domain with main boundary conditions (right).

The exit diameter of the central jet ( $d$ ) is 4.57 mm and the co-flow is stabilised by a perforated disk, which has an outer diameter of 210 mm and has 87% blockage. The

burner has been run at different flame and flow conditions in the past. For the original paper on this burner [30], these conditions are listed in Table 1. For these flow and flame conditions, the total flame length is observed to be  $H_F/d = 30$  and its liftoff height to be  $H/d = 10$ .

In modelling this case, the focus is on combustion in the lifted flame. The combustion process in the coflow is assumed to have already reached the equilibrium state. The boundary conditions of the vitiated coflow are, therefore, set to that of the fully burned products. Figure 1 shows the boundary conditions.

**Table 1:** Flame and flow conditions of Cabra flame based on [30]

Central Jet		Coflow			
$Q_{H_2}$	25 slm	$Q_{H_2}$	225	slm	
$Q_{N_2}$	75 slm	$Q_{Air}$	2,100	slm	
$T_{Jet}$	305	K	$T_{Coflow}$	1,045	K
$V_{Jet}$	107	m/s	$V_{Coflow}$	3.5	m/s
$Re_{Jet}$	23,600		$Re_{Coflow}$	18,600	
$d_{Jet}$	4.57	mm	$d_{Jet}$	210	mm
			$\phi$	0.25	
$X_{H_2}$	0.2537		$X_{H_2}$	0.1474	
$X_{N_2}$	0.7427		$X_{N_2}$	0.7534	
			$X_{H_2O}$	0.0989	

### 3.2 LES solver

The simulations are run on the open-source CFD software OpenFOAM. Both solvers, FC-ESF and FGM-ESF, are built upon the ESF implementation of Breda et al. [15]. The code is adjusted for hydrogen-air combustion and the REaction-Diffusion Manifold (REDIM) tabulation is changed to FGM. The hexahedron mesh consists of 896,724 cells. The Pope criterion is checked to be below 0.2 in the most critical part of the domain. Further mesh quality assessment is done in Appendix C. Two SGS stress models, WALE and  $k$ -equation transported eddy viscosity model, are used and compared in Appendix D. Both models have strong agreement of the velocity profiles with each other and the experiment.

### 3.3 Overall procedure

The schematics of the FC-ESF solver are shown in Figure 2. The pressure and momentum equations are coupled through the PIMPLE algorithm to solve for velocity  $u_j$ . The Wiener and mixing terms are calculated to create the different stochastic fields. After that, the transport equations for the fields of the mass fractions and enthalpy are solved. These quantities are passed to the combustion model and serve as the input for the chemistry ODE solver from which the source terms for the species and enthalpy are derived. The mean, or first moment, of the mass fractions and enthalpy, is then computed. Based on these means the thermodynamic quantities of the flow are corrected. The solver can proceed to the next time step.

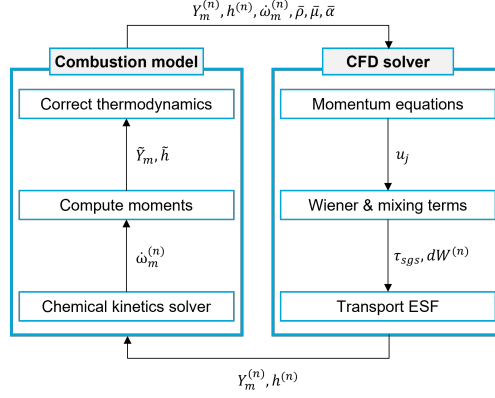


**Fig. 2:** FC-ESF solver schematics

The procedure of the FGM-ESF solver, shown in [Figure 3](#), is similar to the FC-ESF version in terms of the CFD solver, with the exception being the type of fields that are being transported. In this case, the fields for the progress variable and mixture fraction are passed to the combustion model. The controlling variables for each field are used to obtain the temperature and source term from the tabulation. The means for the controlling variables are calculated. From these means, the mass fractions of the species are obtained from a table. They are used to calculate the density from the equation of state. The solver can proceed to the next time step.

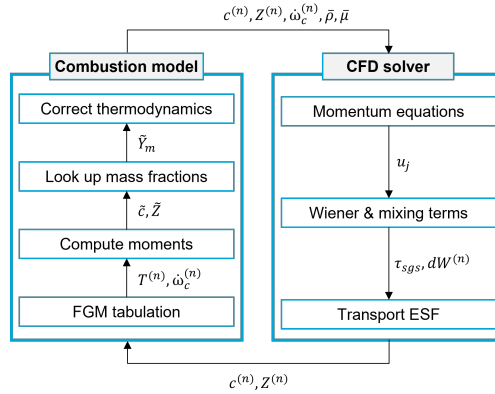


**Fig. 3:** FGM-ESF solver schematics

### 3.4 One-dimensional flamelets and FGM tabulation

The set of one-dimensional Navier-Stokes and species transport equations are solved in CHEM1D to build the flamelet database. The premixed flame is modelled as a freely propagating flame matching the boundary conditions of the validation case. 300

unstrained premixed flames are solved spanning the whole flammability limit from equivalence ratio 0.1329 to 3.5916. The solution for each equivalence ratio is given in terms of the spatial coordinate where one side corresponds to the reactants and the other to the products. The spatial coordinate is mapped onto the normalised progress variable  $c$  and the equivalence ratio onto the (Bilger) mixture fraction  $Z$  creating a two-dimensional table. The points outside the flammability limit are extrapolated to match the boundary condition of the validation case. This corresponds to the boundary conditions of the coflow in the lean limit ( $Z \rightarrow 0$ ), and the condition of the central jet in the rich limit ( $Z \rightarrow 1$ ).

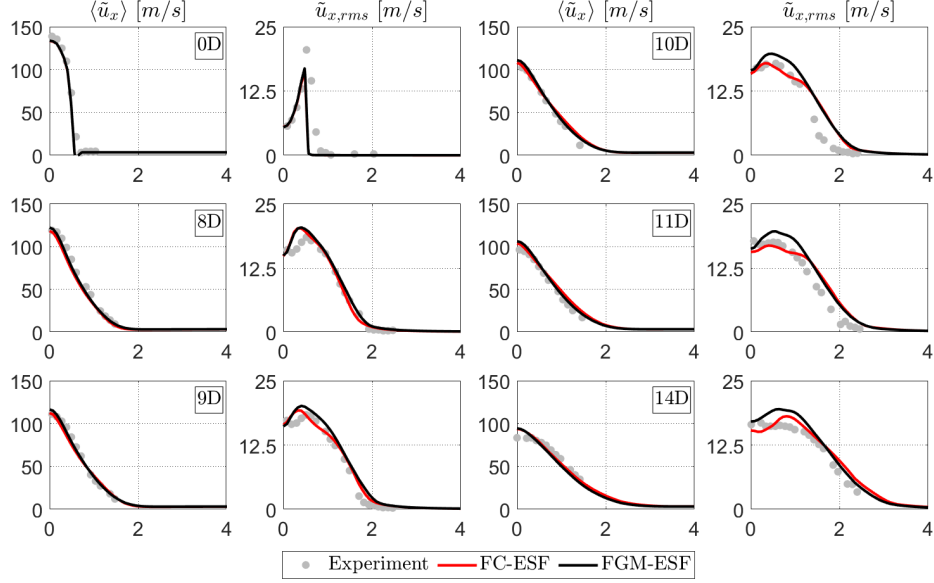
## 4 Results

This section assesses the performance of the FGM-ESF solver. It consists of three parts. The first part compares the obtained numerical results with experimental data to assess the predictive capabilities of both solvers. The next part compares both solvers side-by-side in terms of instantaneous fields to demonstrate the differences between methods. The last part compares the computational costs of the solvers.

### 4.1 Comparison with experimental data

The ESF-FC and ESF-FGM solvers are compared with the experimental results of Cabra et al. [30] in this section. The analysis assesses the mean and root mean squares (rms) of the axial velocity, mixture fraction and temperature. Note that the rms in this context refers to the variability over time of the resolved quantities, and not to the SGS variance, which comes from the local difference between stochastic fields. Both solvers run on the same mesh with 896,724 cells and the WALE SGS stress model. A comparison with the  $k$ -equation SGS model is given in [Appendix D](#)

[Figure 4](#) shows the mean and rms values of the axial velocities. The azimuthal average along different axial locations is plotted. The velocity and rms fields of both solvers is in very good agreement with the experiments. The difference between the first-order statistics is negligible. There are, however, some non-negligible differences with the experiments observed for the rms near the centreline and for axial locations further downstream than  $x/D = 10$ . The figure also shows weak sensitivity to the number of stochastic fields  $N$ . It can be concluded that the turbulence conditions are sufficiently accurately captured by both models.



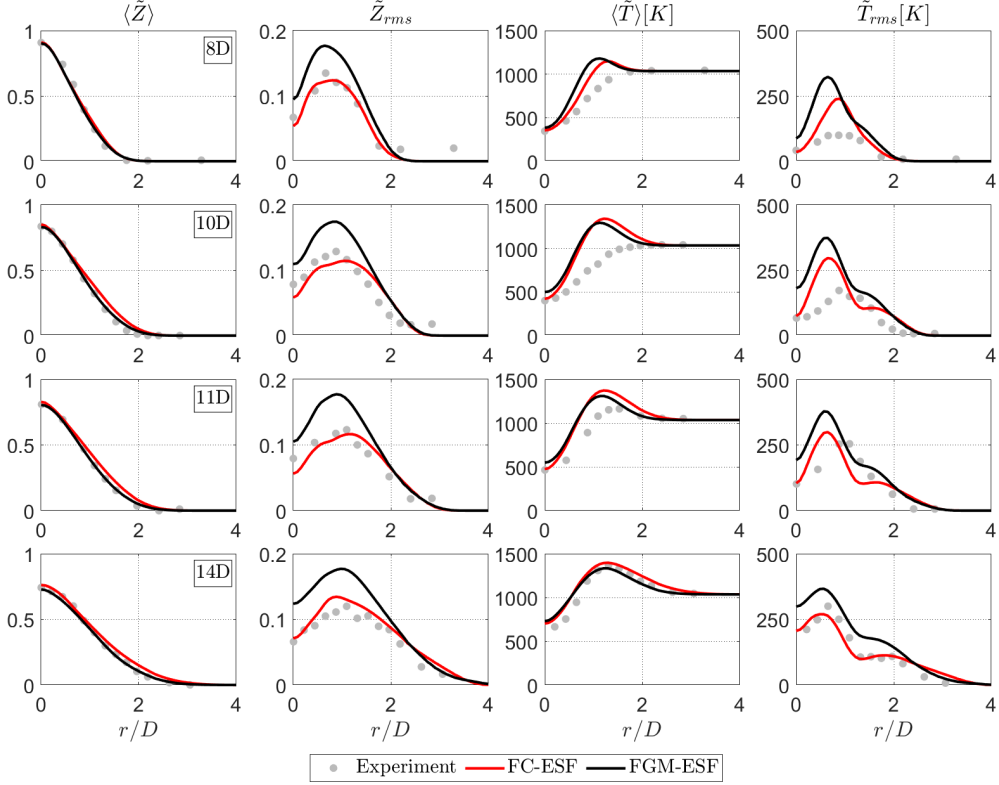
**Fig. 4:** Mean and fluctuating part of velocity  $u_x$  for full chemistry (FC-ESF) and FGM-based (ESF-FGM) solver compared to experimental data [30]

Figure 5 shows the mean and rms of the mixture fraction and temperature along different axial positions. The means of the mixture fraction agree well for both solvers and the experiments. The temperatures of both solvers also agree well, with a slightly higher temperature predicted for the FGM-ESF solver at  $x/D = 8$ . When compared to the experimental data, however, the temperatures are overestimated for more upstream locations due to an underprediction of the lift-off height with about three nozzle lengths. Ignition in the flow is characterised by a peak in temperature in the radial profile. In the absence of such a peak, i.e. monotonic increase in temperature, the increase of temperature is caused by inert mixing between the cold fuel jet and hot coflow. This minor discrepancy in predicting the lift-off height aligns with findings from prior research ([18] and [31]) and was anticipated, considering the high dependence of this variable on the inlet turbulence conditions.

The rms of the mixture fraction is predicted with very good accuracy for the FC-ESF solver. The FGM-ESF solver overestimates this quantity slightly but consistently over all axial locations. The discrepancy is attributed to slower mixing and is further addressed in Appendix B. The rms of temperature shows reasonably good accuracy between models and experiments. However, the underprediction of lift-off height causes a bigger difference between the experiments for more upstream locations.

Analysis of the number of stochastic fields again shows minimal sensitivity to  $N$ , consistent with the observations for the velocity profiles. The FGM-ESF method in particular shows almost identical results for  $N = 2$  and  $N = 8$ , allowing it to be run at relatively low cost. The reason for this result is linked to the weak impact of the subgrid variance on the overall results. Due to the small difference between different

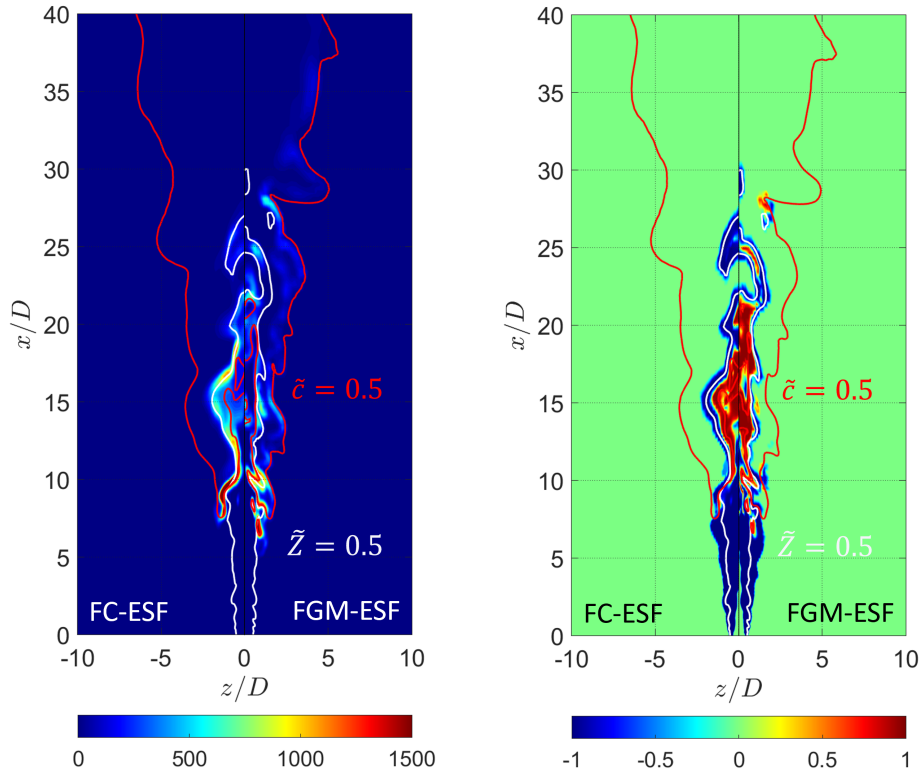
values for  $N$ , only the  $N = 2$  cases are discussed in the remainder of this work. To evaluate the potential capabilities and limitations of the FGM-ESF approach in predicting correct burning states, further characteristics of the reacting flow field as predicted by the two approaches are compared in the next section.



**Fig. 5:** Mean and fluctuating part of mixture fraction  $Z$  and temperature  $T$  for full chemistry (FC-ESF) and FGM-based (ESF-FGM) solver compared to experimental data [30]

## 4.2 Comparison between solvers

Aside from comparing the models with experimental data for validation, it is also useful to investigate differences between both models in terms of instantaneous results, that can not be recovered from experiments. The ESF-FGM approach uses premixed flamelets to predict a partially premixed flame. This implies that it might be limited in predicting the correct burning modes and, by extension, also the correct reaction rates. However, the following analysis shows that despite some small differences with FC-ESF, the less expensive FGM-ESF is capable of representing the correct burning states.



(a) Normalised water reaction rate  $\bar{\omega}_c$

(b) Takeno flame index

**Fig. 6:** Midplane contours of instantaneous flame index and normalised water reaction rate. Stoichiometric mixture fraction  $\tilde{Z} = 0.47$  and progress variable  $\tilde{c} = 0.5$  are marked as white and red lines, respectively

Figure 6a shows an instantaneous snapshot of the midplane contour of the normalised water reaction rate. For the FGM-ESF solver, the value corresponds to the source term in Equation 13 and comes directly from the tabulation. For the FC-ESF solver, the value is reconstructed *a posteriori* using the averaged source term of water ( $\bar{\omega}_{H_2O}$ ). The stoichiometric ratio ( $\tilde{Z} = 0.47$ ) and progress variable of 0.5 are also marked in this figure. Similar features for both approaches are observed through the isocontours of the progress variable and mixture fraction. The anchoring point, or lift-off height, has good agreement between solvers, although FGM-ESF predicts it

slightly more upstream. Also, the magnitude of the normalised reaction rate is comparable. These observations are in line with the time-averaged statistics discussed in the previous section.

To develop a deeper understanding of the instantaneous burning features, [Figure 7](#) shows scatter plots of important thermochemical quantities in the flame region. Each dot represents one cell in the mesh. The colour of each dot represents its axial position in the domain and can serve as a relative time indication between points. In the displayed graphs, the temperatures and water vapour concentrations are only shown for instances where  $\tilde{c} > 0.1$ , to omit the unburnt state. Similarly, the plots for the averaged reaction rate ( $\overline{\tilde{\omega}_c}$ ) focus only on the reactive cells by being limited to realizations exceeding 5% of the maximum reaction rate from flamelet calculations. The equilibrium conditions and the maximum reaction rate, derived from the flamelet database, are denoted by the blue line. The flammability limits and the stoichiometric point are marked by vertical dashed lines. The conditional averages obtained from the FC-ESF and FGM-ESF models are depicted with red and black lines, respectively.

A first observation from the scatter plots is that the FGM-ESF model has higher peak temperatures. In fact, it covers all burning states up until the equilibrium point. The FC-ESF model does not completely reach equilibrium values, suggesting a slower overall combustion timescale compared to the flamelet approach. The conditional average of temperature is very similar for both approaches. The exception is in the rich limit where they differ slightly. This small disparity is caused by two factors: slower mixing for FGM-ESF, which allows for more very rich points, and the linear extrapolation outside the flammability region. The slower combustion timescale is further supported by the water mass fraction data, indicating slightly more water production in the FGM-ESF model. Although again the conditional means in mixture fraction space are similar between both models. Near stoichiometry, the FC-ESF model might also predict some dissociation of water vapour at high temperatures which reduces temperature, through its endothermic nature, and water mass fraction. The main reason, however, seems to be the absence of the corrective term for the reaction rate, discussed later in this section.

An analysis of the colours of the scatter plots also demonstrates interesting differences. While reactive states are observed to start more upstream (darker blue) for FGM-ESF, consistent with the lower lift-off height discussed before, a higher amount of rich burning states are observed at more downstream locations (red). The observation suggests slower mixing for the FGM-ESF model. This conclusion is further supported by the fact that rich equilibrium conditions are reached more downstream for FGM-ESF, even though the flame anchor point lies more upstream. Furthermore, examining the conditional averages of the normalised reaction rates shows that there are two peaks for both solvers. However, the rich peak is shifted slightly to the right for the FGM-ESF method. This indicates that on average the mixture burns at richer conditions compared to FC-ESF. Another observation that can be made from the reaction rate scatter plots is that both models predict super-equilibrium conditions near the rich flammability limit (indicated by points above the blue line). This suggests that the FGM-ESF model is able to predict these states, at least from a qualitative standpoint.

Although the argument of a faster combustion timescale supports the higher (conditional) reaction rates for the FGM-ESF at most mixture ratios, a higher lean peak ( $0.2 < Z < 0.4$ ) is predicted for the FC-ESF solver. This indicates that there might be differences in the predicted combustion modes between models. To analyse this hypothesis, the Takeno flame index is calculated *a posteriori* and shown in [Figure 6b](#). The flame index uses the normalised inner product of fuel and oxidizer gradients to reveal the combustion mode. When both gradients are aligned and point in the same direction, the mixture is assumed to be well mixed and to burn in the premixed mode, corresponding to a value of 1. When both gradients align but point in opposite directions, this suggests non-premixed combustion and corresponds to value -1. Values around zero can indicate either a mixed combustion mode or that at least one of the gradients is zero. The index is defined as

$$\text{F.I.} = \frac{\nabla Y_{\text{H}_2} \cdot \nabla Y_{\text{O}_2}}{|\nabla Y_{\text{H}_2} \cdot \nabla Y_{\text{O}_2}|}. \quad (16)$$

Although the accuracy of this definition has been debated, it is used here only as a relative and qualitative measure between methods. For the FC-ESF method, the instantaneous contour of the index shows a flame index approaching -1 in regions of inert fuel-oxidizer mixing upstream of the flame. Downstream of the ignition point ( $X/D \approx 8$ ), a non-premixed burning mode is identified along the stoichiometric line. A premixed mode at rich conditions also appears in the core of the jet at  $10 < x/D < 20$  as the dominating mode. It is surrounded by the residual unburnt fuel that further reacts with the oxidizer in the coflow in the non-premixed mode. The FGM-ESF predicts a similar distribution of the index, even though it retrieves the mass fractions of oxygen and fuel from laminar flamelets. Thus, the chosen set of controlling variables appears to adequately capture the information necessary to recover the correct burning modes. Comparing the flame index with the reaction rates, one can infer that the lean peak observed in [Figure 7](#) corresponds to the lean premixed combustion mode close to the flame ignition point. The rich premixed combustion occurs mostly downstream. Near stoichiometry, the flame mainly burns in the non-premixed mode.

In the previous calculations, the correction for the source term ([Equation 15](#)) is ignored. To evaluate whether this has a material impact on the results, it is calculated *a posteriori* by looking up the second derivative term from the FGM database. The corrected reaction rate ( $\bar{\omega}_c + \bar{\omega}_{\text{np}}$ ) is shown by the black dash-dot line in [Figure 7](#). The correction is strongest near stoichiometric conditions and appears to be effective in retrieving the correct burning state in those regimes.  $\bar{\omega}_{\text{np}}$  appears to be larger than  $|\bar{\omega}_c|$  in most cases. This leads to a negative overall source term, which could lead to numerical issues when solving the transport equations. That problem needs to be addressed before it can be directly implemented in the LES. A solution would be to truncate negative values, which would only lead to negligible differences in the conditional conditional averages of reaction rate.

The analysis presented above suggests that the FGM approach with a premixed flamelet database is effective in depicting the correct burning states. While there are minor differences compared to the FC-ESF approach, they are anticipated due to a better representation of the chemical processes when species are transported in the LES. However, these discrepancies do not appear to have a significant impact on the

statistical predictions. A benefit of this simplified representation of the FGM-ESF method is reduced computational load. This is assessed next.

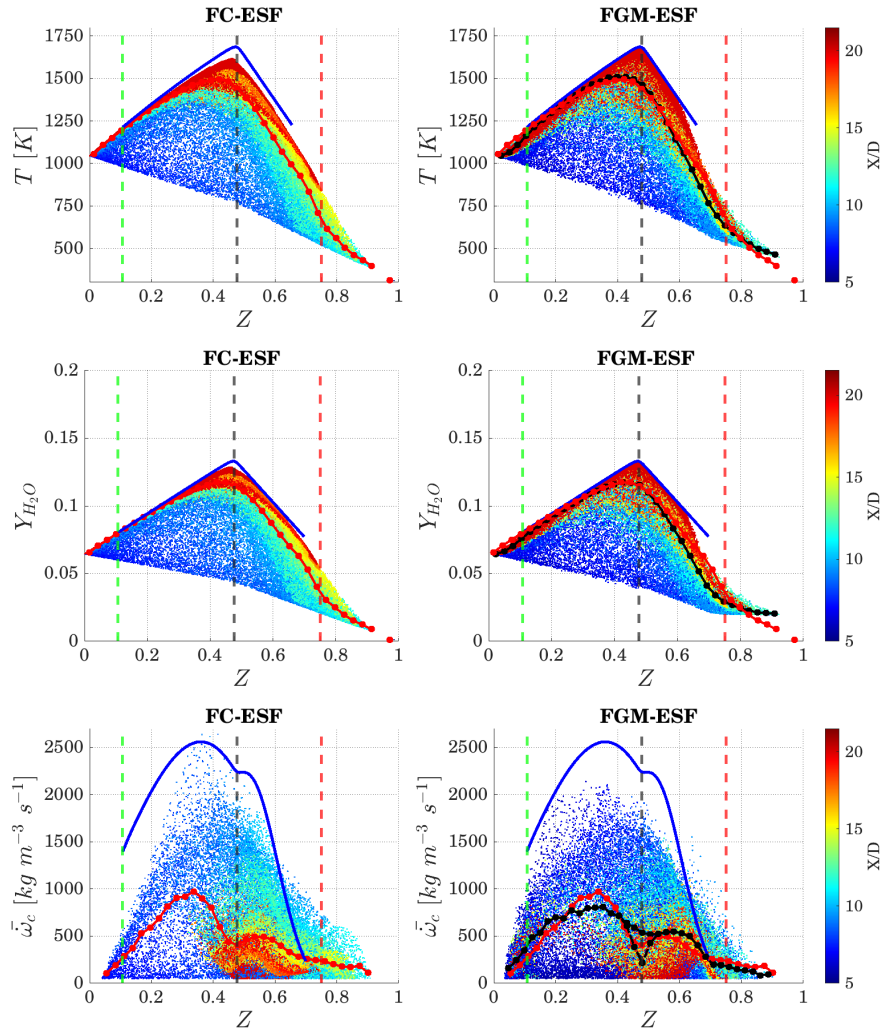


**Fig. 7:** Scatter plots at a random time step of temperature  $T$  (top), water mass fraction  $Y_{\text{H}_2\text{O}}$  (centre) and water normalised reaction rate  $\bar{\omega}_c$  (bottom) versus mixture fraction, obtained using the FC-ESF (left) and FGM-ESF (right) models.

### 4.3 Computational efficiency

Both solvers are tested for computational speed on the fully developed flow. Their execution times are measured across 100 iterations, using a constant timestep and

varying the number of fields. The findings are presented in [Figure 8](#). Two key insights emerge from these tests.

First, the FGM-ESF solver exhibits less sensitivity to the number of fields compared to the FC-ESF solver. This difference arises from the way each solver handles fields in their transport equations. In the FGM-ESF solver, only two controlling variables are transported, the actual number of transported fields is  $2N$ . In contrast, the FC-ESF solver includes 10 species and an enthalpy equation, increasing the field count to  $11N$ . This disparity becomes particularly noticeable in complex mechanisms involving a large number of species, such as in kerosene combustion. Hydrogen combustion, however, is a relatively simple process.

Secondly, the scaling behaviour of the two solvers shows a notable difference. While FC-ESF scales efficiently with increased processors, the performance of the FGM-ESF solver begins to plateau around the 100-processor mark and even shows increased execution times with a larger number of processors. It should be noted, however, that the number of cells per processor falls below 10,000 at that point, which is considered to be very low in the context of CFD simulations. This limitation in minimum cell numbers is more a consequence of implementation inefficiencies rather than an intrinsic shortcoming of the method. The FC-ESF solver is built on the foundation of existing chemical kinetics and mesh-based Eulerian solvers in OpenFOAM, which are inherently designed to support parallel processing. In contrast, the primary computational load for the FGM-ESF solver comes from 2D table interpolation, a process that has not been fully optimized yet. Therefore, there is significant potential for performance improvements in the FGM-ESF solver through optimization efforts. Furthermore, preliminary testing on larger meshes indicates that the FGM-ESF method may offer substantial reductions in computational costs when compared to the FC-ESF method. However, these findings are yet to be formally substantiated, owing to resource limitations, and thus require further validation.

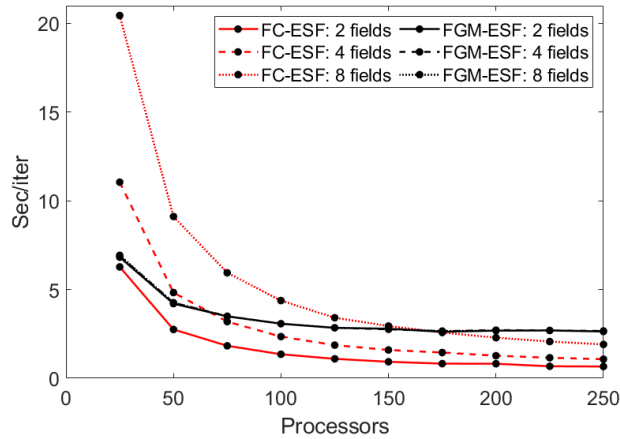


**Fig. 8:** Solver speeds based on 100 iterations on the fully developed flow

## 5 Conclusion

An LES method with ESF closure and (premixed) FGM tabulation (FGM-ESF) has been developed and analysed. This innovative hybrid model is tailored for partially premixed hydrogen flames, demonstrating for the first time the predictive capabilities of the method for this particular type of flames. The FGM-ESF method was assessed and compared not only with experiments but also with the classical and more expensive ESF method that utilises fully transported chemistry (FC-ESF).

Both the FGM-ESF and FC-ESF models exhibit excellent agreement with experimental measurements in terms of mean velocity, temperature, and mixture fraction. However, the rms values for these quantities are slightly overpredicted in the FGM-ESF approach, attributed to the slower mixing of the mixture fraction. Despite this, the FGM-ESF model still closely mirrors the results of the fully transported chemistry approach. Additionally, the FGM-ESF model has been found to be weakly sensitive to the number of Eulerian stochastic fields used, with using just two fields proving to be satisfactory.

The examination of the instantaneous burning states reveals that, generally, the FGM-ESF model predicts a faster time scale. However, this does not hold true in lean areas and in regions with a very rich mixture composition. The discrepancies observed near the stoichiometric point are primarily due to the prevalence of non-premixed burning, especially near the flame's ignition zone. Despite this, implementing a corrective factor has proven effective in rectifying the burning state, even though the FGM's thermochemical database relies solely on premixed flamelets.

In regions dominated by premixed burning, particularly the lean and very rich areas, some variations in local reaction rates have been noted. Yet, the FGM-ESF model successfully captures the essential qualitative aspects, including the prediction of super-adiabatic conditions and a double-peak pattern in conditional reaction rates. Importantly, these quantitative deviations have only a minimal impact on the overall statistical predictions.

In terms of computational cost, the ESF-FGM model is less sensitive to an increase in stochastic fields due to the smaller number of transport equations. However, it has currently reached its maximum computational speed of 10,000 cells per processor. Further improvements are likely achievable by optimizing the tabulation interpolation routine for parallel computing, enhancing the model's overall efficiency and applicability in practical scenarios.

The predictive capabilities of the FGM-ESF are promising, especially considering the potential reduction in costs on larger meshes. As the pursuit of developing precise and economically viable numerical tools for designing effective hydrogen combustion technologies continues, the ESF-FGM model can emerge as a valuable asset by offering a blend of precision and cost-efficiency that is essential for practical applications.

## Appendix A Notes on code development

This appendix offers a perspective on the development of the new code, specifically focusing on the implementation of the FGM-ESF solver.

The FGM-ESF solver is a novel approach, with Avdic et al.'s work [14] being the only prior instance of a similar implementation, albeit applied to a markedly different flame (stratified methane flame). The implementation performed within this thesis work is based on the REDIM-ESF solver, originally presented by Breda et al. [15] and applied to the Sandia flame. Additionally, the FC-ESF solver, based on Hansinger's work [32], was in a workable state due to the previous application on a trapped vortex hydrogen flame. The mesh for the Cabra flame of Ferrante et al. [33] was used.

Implementing the FC-ESF code for the Cabra flame was relatively straightforward, thanks to the pre-existing mesh and functioning example case. However, challenges arose with the REDIM-ESF implementation. There were no pre-existing functioning cases to reference, and the lack of REDIM tabulation data made case setup for this solver too time-consuming. There was no documentation on the code aside from the paper, which focused primarily on the model and not on the code itself. Consequently, the entire code had to be reverse-engineered line-per-line while the student had no prior experience in OpenFOAM or C++.

This approach started by copying the existing Cabra flame setup for the FC-ESF solver. To prevent ignition, the boundary conditions were altered to reflect ambient environmental conditions. As a temporary measure, a dummy tabulation consisting of constant values was used. Following these adjustments, the code was executed. Each error encountered guided the student to modify or insert the necessary line. This meticulous, line-by-line process continued until the solver successfully completed several timesteps without any errors. This success paved the way for the next step: generating and implementing the FGM tabulation.

The REDIM-ESF code and the FGM-ESF shared similar types of control variables due to being developed for partially premixed flames, namely a  $\text{CO}_2$ -based progress variable and a  $\text{N}_2$ -based mixture fraction. After figuring out the specific format required for the tabulation, the next step was to transform the CHEM1D flamelet data into this format. Gioele Ferrante provided me with flamelet data and the code to post-process this efficiently. This provided a significant speed-up of this important step significantly. In the generation of the FGM tabulation, various definitions of mixture fractions were tested. These included the nitrogen-based mixture fraction, which is only effective under the unity Lewis number assumption, as well as the Regele [34] mixture fraction, which is convenient for a one-step irreversible chemical reaction, and the Bilger [35] mixture fraction, which is based on elemental mass fractions. Interestingly, the results across all these fractions were remarkably consistent, each appearing as near-perfect projections of the others. After careful consideration, the Bilger mixture fraction was selected, as it is deemed the most scientifically robust choice for these types of flames.

Two distinct versions of the flamelets are considered in this work. The first version was based on the unity Lewis number assumption in the flamelet calculations. However, this approach resulted in poor flame anchoring. Surprisingly, the issue stemmed from

an excessively high source term, which consequently reduced the chemical timescale. This led to an exceptionally thin flame front, which, in the face of intense turbulence, failed to stabilize effectively. The second version, utilizing a mixture-averaged approach, demonstrated improved flame anchoring. Despite incorporating differential diffusion effects into the flamelet calculations, it remained an open question whether a specific model was necessary for the controlling variables, particularly for the mixture fraction, which is the key variable to differential diffusion effects.

A preferential diffusion model [26] was implemented for both the mixture fraction and the progress variable. This model includes different Lewis numbers for the species in the formulation of the diffusive flux of controlling variable  $\phi_\alpha$

$$\mathbf{j}_{\phi_\alpha} = -\frac{\lambda}{c_p} \nabla \left( \underbrace{\sum_{i=1}^{N_s-1} \frac{\alpha_i - \alpha_{N_s}}{Le_i} Y_i}_{\beta_{\phi_\alpha}} \right), \quad (\text{A1})$$

where  $\lambda$  is the conductivity,  $c_p$  is the specific heat capacity at constant pressure, and  $\alpha_i$  corresponds to the weights of the species  $i$  in controlling variable  $\phi_\alpha$ . The term  $\beta_{\phi_\alpha}$  can be calculated from flamelets and tabulated as a function of the controlling variables. This required the inclusion of extra variables in the tabulation, adjustment of the solver code and construction of a new combustion class in OpenFoam. However, this model resulted in an excessively low lift-off height, while the previous results, without an explicit differential diffusion model, were already sufficiently accurate. The reason for this model's inefficiency could be attributed either to its implementation or its suitability for this specific type of flame. This aspect was not further explored, as the mixture averaged model without the preferential diffusion model was already performing adequately.

Once a functional base version and case for the code were established, a sensitivity analysis on various parameters was performed, with the most significant ones detailed in the other appendices. This analysis encompassed several factors: the SGS scale stress model, chemical mechanisms, mixture coefficient, the number of fields, and the choice between a fixed or varying timestep. With the exception of the chemical mechanism, these adjustments yielded comparable and satisfactory outcomes. The only open issue is that of the rms overprediction for which no clear explanation was found in time. It is discussed further in [Appendix B](#).

In summary, a substantial portion of the student's efforts was devoted to bringing the solver to an operational state, a task complicated by the scarcity of examples and documentation. This focus on foundational development meant that there was limited opportunity to apply the solver to other cases or to delve into specific phenomena such as NOx formation or the effects of strain, which were part of the original objectives. However, the current work has proven the potential capabilities of the model and serves as an important foundation for future extensions of the model.

## Appendix B Investigation on rms overprediction

This appendix sheds light on the discrepancy in the rms predictions of the FGM-ESF solver.

In Figure 5, it is observed that rms values of the mixture fraction are higher than those obtained from the FC-ESF solver and experimental data. Similarly, the rms values for temperature are also overestimated. It is important to note that temperature is just a dependent value determined by the mixture fraction (and progress variable), indicating that the primary difference is with the mixture fraction.

Initially, one may think that this overestimation is due to an inaccurate estimation of the second statistical moment of  $\tilde{\mathcal{P}}_{sgs}$ , but this is not the case. These rms values are derived from time-averaged data at the resolved scale level. The overprediction is actually caused by transient, fuel-rich areas moving past the measurement point, leading to oscillating local mixture fraction values. Figure B1a presents an instantaneous cross-section of the mixture fraction, demonstrating this effect. The cause is essentially slower mixing for the FGM-ESF solver. Several potential factors have been explored.

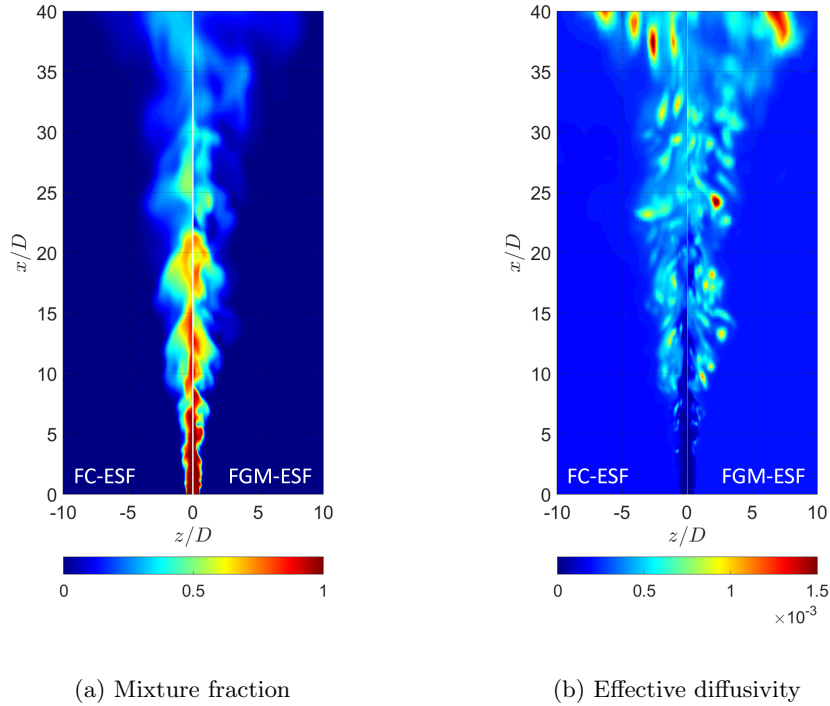


**Fig. B1:** Midplane contours for FC-ESF (left) and FGM-ESF (right) solvers

There are several terms in [Equation 13](#) influencing the mixing behaviour of the scalars. The turbulent diffusion term (third term on the LHS) is determined by diffusivity and scalar gradient. A comparative analysis of these variables between the two solvers indicates negligible differences, as can be seen in [Figure B1b](#). Furthermore, the stochastic term (first term on the RHS) was eliminated by setting  $dW$  to zero, yet the rms values remained overestimated. An evaluation of the micro-mixing term's effect (second term on the RHS) was also conducted by setting  $N$  to 1, cancelling the term. However, this gave the same result.

Considerable time and effort have been invested in addressing this issue but the definitive root cause has yet to be identified. The discrepancy might stem from intrinsic differences between the solvers or from variations in their implementation. While this issue does not significantly affect other results, it presents an intriguing anomaly that merits further investigation in future studies.

## Appendix C Mesh quality assessment

This appendix assesses the quality of the mesh. The same mesh was used as in Ferrante et al. [33], where similar calculations were performed using an FGM-PPDF approach. Due to a lack of computational resources, it was not possible to run a mesh independence study on a finer mesh. However, the quality of the mesh is assessed through a set of other criteria.

### C.1 Mesh geometry

The *checkMesh* utility in OpenFOAM returns several checks and metrics to check the mesh's geometry.

The mesh has passed all build-in topology checks, including boundary definition, cell-to-face addressing, and point usage. This suggests that the mesh is well-constructed without evident topological errors. The mesh contains 5 boundary patches, each characterized as "non-closed singly connected," which is typical for inlet, outlet, and wall boundaries in CFD. This indicates appropriate treatment of boundary conditions.

The cell and boundary openness values are exceptionally close to zero (approximately at machine precision:  $10^{-16}$ ), demonstrating that the mesh is properly sealed with no gaps or misalignments. The maximum aspect ratio stands at 82.08, which, while slightly high, indicating some cells may be elongated, remains within acceptable parameters. The maximum non-orthogonality is recorded at 40.52 degrees, averaging 10.13 degrees, which falls within the acceptable range. The maximum skewness, at 2.42, is considered acceptable, signifying that the cells are not overly distorted. Furthermore, the minimum and maximum face areas and cell volumes are well within good ranges, ensuring there are no excessively small or large cells that could adversely affect the simulation's stability and precision.

### C.2 Pope criterion

To be able to sufficiently accurately model the flow in LES, enough of the kinetic energy should be captured by the resolved scales. Finer meshes include smaller scales in the resolved scales, thus increasing the amount of resolved kinetic energy in the flow. There are several estimators used in the literature. While using multi-grid estimators, such as LES\_IQ [36], would be desirable for determining the actual order of numerical or modelling errors instead of relying on their theoretical values [37], constraints in computational resources necessitate the use of single-grid estimators. A popular single-grid estimator is the relative resolved turbulent kinetic energy content, calculated as

$$RKE = \frac{\langle k_{sgs} \rangle}{\langle k_{sgs} \rangle + K}, \quad (C2)$$

where  $K$  represents the resolved kinetic energy, which can be calculated from the rms values as

$$K = 0.5(\tilde{u}_{x,rms}^2 + \tilde{u}_{y,rms}^2 + \tilde{u}_{z,rms}^2) \quad (C3)$$

Time-averaged values of  $k_{sgs}$  are used in order to align with the rms values of  $u_i$ , which are inherently time-averaged.

$k_{sgs}$  is more complicated to retrieve for the WALE model due to its implicit modelling approach. However, it can be easily retrieved for the  $k$ -equation model as it is a transported quantity. According to the Pope criterion, a minimum of 80% of the kinetic energy must be resolved. [Figure C2](#) illustrates the relative turbulent kinetic energy content (RKE). To meet the criterion, this quantity should be less than 0.2. The white line indicates the lean flammability limit  $\tilde{Z} = 0.107$ . The criterion is largely met throughout the domain, with exceptions occurring in areas significantly downstream. Here, higher  $RKE$  values arise due to  $K$  approaching zero, whereas  $k_{sgs}$  does not. This discrepancy stems from the incomplete convergence of time-averaged moments in these zones. The lower typical velocities found far downstream, approximately one-third of those at the start of the jet, result in a longer period needed for the time averages to stabilize. Extending the time-averaging window would rectify these discrepancies, eliminating areas of high values. However, due to computational limitations, running further timesteps was not feasible. Despite this, the available data sufficiently supports adequate fulfilment of the Pope criterion.

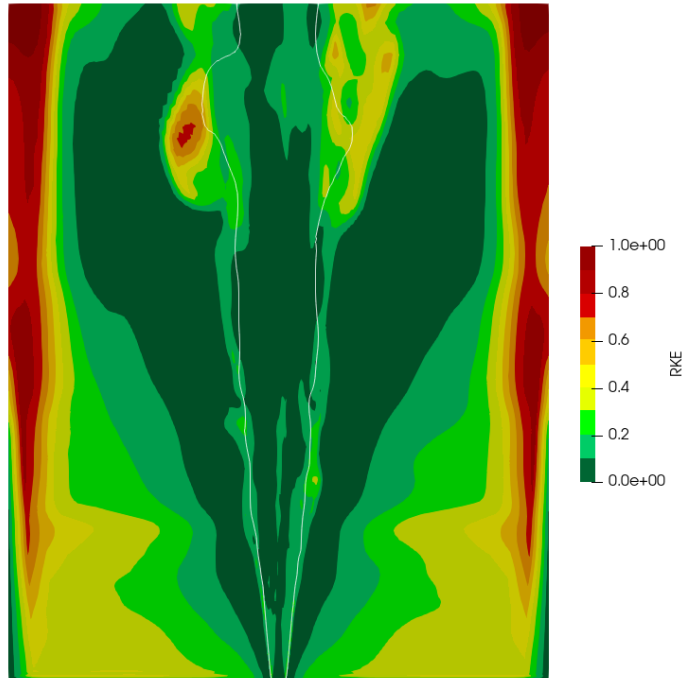


**Fig. C2:** Relative resolved turbulent kinetic energy content. Lean flammability limit  $\tilde{Z} = 0.107$  is marked in white.

## Appendix D Sensitivity analysis on SGS stress model

This appendix compares the sensitivity with respect to the SGS stress model used in the analysis.

Figure D3 presents the midplane contours of the instantaneous subgrid-scale (SGS) eddy viscosity ( $\nu_{sgs}$ ) for two different turbulence models. The visualization clearly shows the distinct results of the algebraic and transported eddy viscosity models in calculating  $\nu_{sgs}$ .

In the algebraic WALE model, high eddy viscosity values are observed in areas characterized by intense local strain rates and vorticity. This model computes eddy viscosity based on the instantaneous local flow conditions without considering the flow's prior history. As a result, the WALE model tends to form localized pockets of high eddy viscosity where the flow is particularly turbulent.

Conversely, the  $k$ -equation model, which is a transported model, derives eddy viscosity directly from the transported subgrid-scale kinetic energy ( $k_{sgs}$ ). This approach inherently incorporates the flow's history, as  $k_{sgs}$  embodies the accumulation of SGS turbulent energy over time. Consequently, in the  $k$ -equation model, the eddy viscosity at a given point is influenced not only by the current flow conditions but also by past turbulence, leading to a more distributed or "smeared out" pattern of eddy viscosity across subsequent time steps.

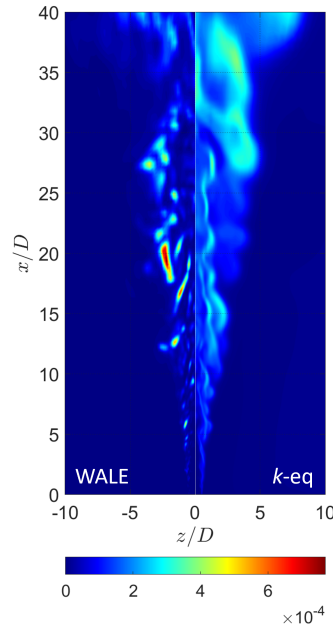
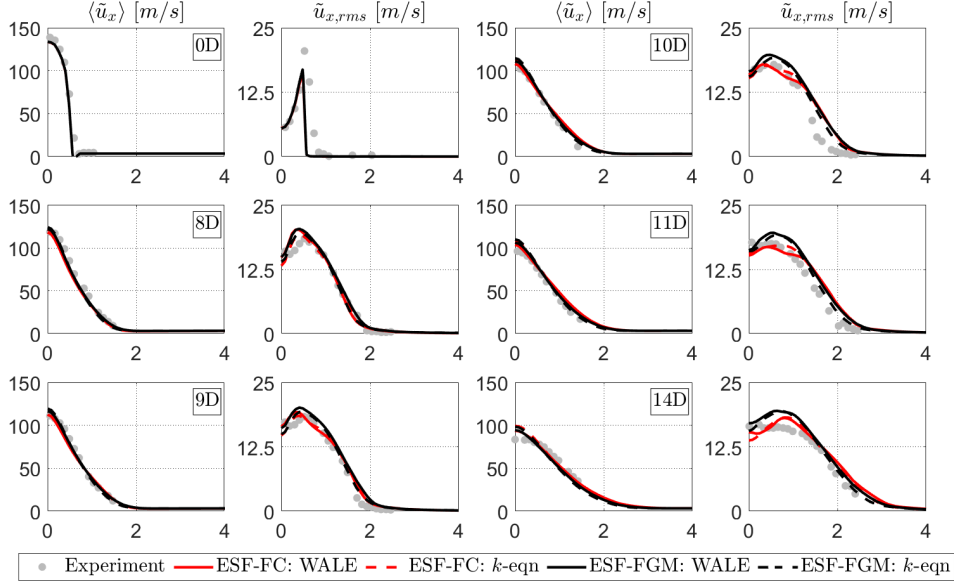


Fig. D3: Eddy viscosity  $\nu_{sgs}$  for WALE (left) and  $k$ -equation (right) SGS stress models

Despite these fundamental differences in the calculation and distribution of eddy viscosity between the two models, it is interesting to note that their velocity profiles, as shown in [Figure D4](#), are remarkably consistent. This similarity suggests that while the models may represent the turbulent viscosity differently, they both effectively capture the overall flow dynamics, particularly in terms of velocity distribution. This observation reinforces the idea that different modelling approaches can yield similar macroscopic flow characteristics, even though they may represent the underlying turbulent processes in distinct ways.



**Fig. D4:** Mean and fluctuating part of velocity  $u_x$  for full chemistry (FC-ESF) and FGM-based (ESF-FGM) solver with different SGS stress models compared to experimental data [\[30\]](#)

In this specific case, both models exhibit a high level of agreement in their results. However, it is essential to recognize that this agreement may not hold true for all scenarios. One critical factor to consider is the interaction with walls. The Cabra flame’s minimal interactions with walls is a key point, as wall effects can profoundly influence turbulence behaviour and significantly impact the performance of turbulence models. In practical combustor designs, wall interactions often play an important role, demanding models capable of accurately simulating these complex dynamics. The Wall-Adapting Local Eddy-viscosity (WALE) model, purposefully designed for situations involving wall interactions, excels in accurately representing turbulence near walls, making it well-suited for real-world applications like combustors. However, similar to other algebraic eddy viscosity models, the WALE model is built on the assumption of a local equilibrium between the production and dissipation of SGS

kinetic energy. This assumption is used to formulate an expression for eddy viscosity that depends on the resolved strain rate tensor. This method stands in contrast to transported eddy viscosity models, which do not depend on the assumption of local equilibrium but instead transport the subgrid-scale kinetic energy. The transported eddy viscosity model is, therefore, expected to perform better in non-equilibrium flows such as transitioning flows where, if turbulence transitions quickly enough from one self-similar state to another, non-equilibrium characteristics can be observed. This evolution must occur rapidly in comparison to the turbulent time scales, as a sufficiently gradual change might result in a quasi-static evolution through equilibrium states [38].

## Appendix E Sensitivity analysis on chemical mechanisms

This appendix delves into the selection of the chemical mechanism, a decision primarily influenced by the preliminary analysis of the FC-ESF solver, which handles the chemistry computations within the solver framework. The following conclusions can be extended to the FGM-ESF as well.

For this thesis, two chemical mechanisms are considered. The San Diego mechanism [39] was initially developed for hydrocarbons up to C3 [40] but the H<sub>2</sub>/O<sub>2</sub> is often used for hydrogen combustion. The second mechanism is the Ó Conaire mechanism [23], which is a dedicated hydrogen-oxygen mechanism. Both mechanisms consist of 10 species and 21 reactions but the parameters of the Arrhenius equation differ slightly. These differences lead to the San Diego mechanism predicting a lower lift-off height than Ó Conaire as can be seen in Figure E5.

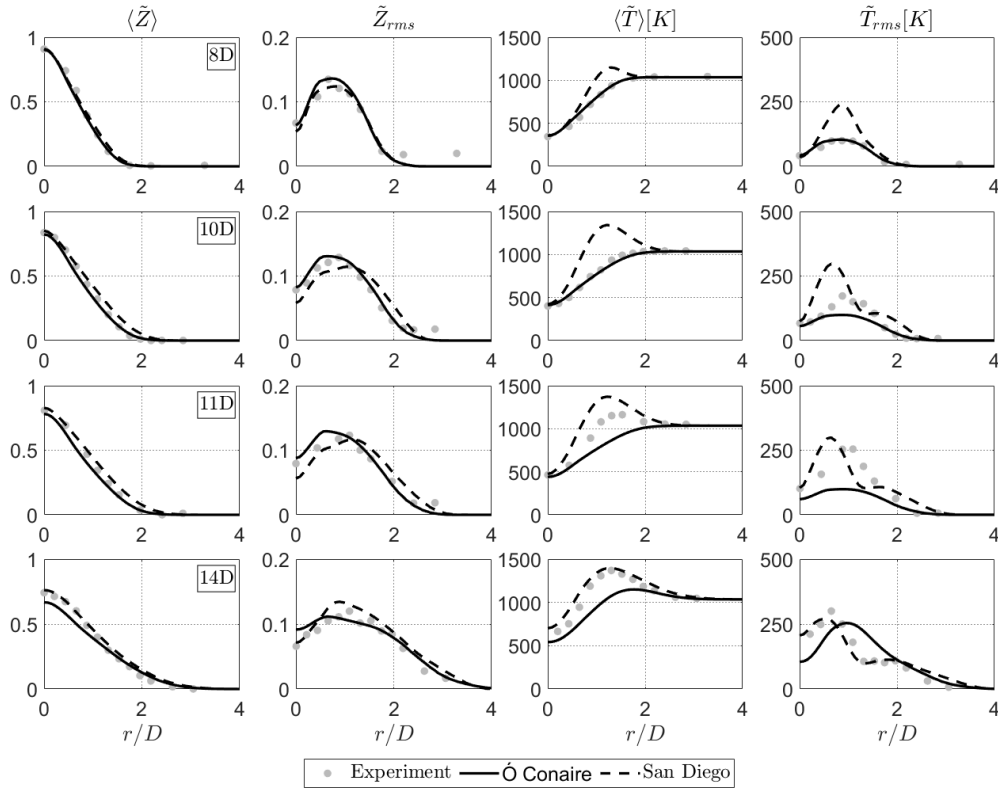


**Fig. E5:** Mean and fluctuating part of mixture fraction  $Z$  and temperature  $T$  for Ó Conaire and San Diego mechanisms compared to experimental data [30]

The most important difference between the two mechanisms is that in the chain-branching reaction ( $\text{H} + \text{O}_2 = \text{OH} + \text{O}$ ) a temperature correction is made for the San Diego mechanism. This reaction is considered one of the most important and sensitive reactions in hydrogen combustion [40]. Differences in reaction coefficients significantly impact key metrics like chemical timescale. Consider Figure E6 where the reaction forward rate constant  $k_f$  is plotted for different temperatures.

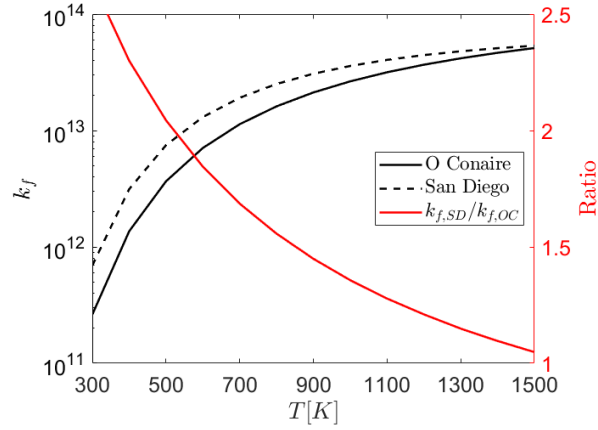


**Fig. E6:** Forward rate constant of chain-branching reaction at different temperatures

The values for the rate constants for the chain-branching reaction approach zero for higher temperatures. However, at lower temperatures significant differences can be observed. The negative temperature exponent  $\beta$  has a less significant impact on the rate constant at these lower temperatures for the San Diego mechanism causing a higher forward rate constant than Ó Conaire. This higher rate constant causes the lift-off height to be smaller for San Diego.

## References

- [1] Bicer, Y. & Dincer, I. Life cycle evaluation of hydrogen and other potential fuels for aircrafts. *International Journal of Hydrogen Energy* **42**, 10722–10738 (2017).
- [2] Rao, A. G., Yin, F. & Werij, H. G. Energy transition in aviation: The role of cryogenic fuels. *Aerospace* **7**, 181 (2020).
- [3] Yusaf, T. *et al.* Sustainable aviation—hydrogen is the future. *Sustainability* **14**, 548 (2022).
- [4] Verstraete, D. On the energy efficiency of hydrogen-fuelled transport aircraft. *International Journal of Hydrogen Energy* **40**, 7388–7394 (2015).
- [5] Manigandan, S., Praveenkumar, T., Ryu, J. I., Verma, T. N. & Pugazhendhi, A. Role of hydrogen on aviation sector: A review on hydrogen storage, fuel flexibility, flame stability, and emissions reduction on gas turbines engines. *Fuel* **352**, 129064 (2023).
- [6] Skottene, M. & Rian, K. E. A study of nox formation in hydrogen flames. *International Journal of Hydrogen Energy* **32**, 3572–3585 (2007).
- [7] McDonell, V. *Lean combustion in gas turbines* (Elsevier, 2016).
- [8] Schefer, R. W., White, C. & Keller, J. *Lean hydrogen combustion* (Elsevier, 2008).
- [9] Lipatnikov, A. & Chomiak, J. Molecular transport effects on turbulent flame propagation and structure. *Progress in energy and combustion science* **31**, 1–73 (2005).
- [10] Pope, S. B. Turbulent flows. *Measurement Science and Technology* **12**, 2020–2021 (2001).
- [11] Pierce, C. D. & Moin, P. Progress-variable approach for large-eddy simulation of non-premixed turbulent combustion. *Journal of fluid Mechanics* **504**, 73–97 (2004).
- [12] Van Oijen, J. & De Goey, L. Modelling of premixed laminar flames using flamelet-generated manifolds. *Combustion science and technology* **161**, 113–137 (2000).
- [13] Fiorina, B., Veynante, D. & Candel, S. Modeling combustion chemistry in large eddy simulation of turbulent flames. *Flow, Turbulence and Combustion* **94**, 3–42 (2015).
- [14] Avdić, A., Kuenne, G., di Mare, F. & Janicka, J. LES combustion modeling using the Eulerian stochastic field method coupled with tabulated chemistry. *Combustion and Flame* **175**, 201–219 (2017).

- [15] Breda, P., Yu, C., Maas, U. & Pfitzner, M. Validation of an eulerian stochastic fields solver coupled with reaction–diffusion manifolds on LES of methane/air non-premixed flames. *Flow, Turbulence and Combustion* **107**, 441–477 (2021).
- [16] Jones, W. & Prasad, V. Large eddy simulation of the sandia flame series (d–f) using the eulerian stochastic field method. *Combustion and Flame* **157**, 1621–1636 (2010).
- [17] Benim, A. C., Pfeiffelmann, B., Ocloń, P. & Taler, J. Computational investigation of a lifted hydrogen flame with LES and FGM. *Energy* **173**, 1172–1181 (2019).
- [18] Jones, W. & Navarro-Martinez, S. Large eddy simulation of autoignition with a subgrid probability density function method. *Combustion and Flame* **150**, 170–187 (2007).
- [19] Han, W., Raman, V. & Chen, Z. LES/PDF modeling of autoignition in a lifted turbulent flame: Analysis of flame sensitivity to differential diffusion and scalar mixing time-scale. *Combustion and Flame* **171**, 69–86 (2016).
- [20] Nicoud, F. & Ducros, F. Subgrid-scale stress modelling based on the square of the velocity gradient tensor. *Flow, turbulence and Combustion* **62**, 183–200 (1999).
- [21] Kim, W.-W. & Menon, S. *A new dynamic one-equation subgrid-scale model for large eddy simulations* (AIAA, 1995).
- [22] Balakrishnan, G., Smooke, M. & Williams, F. A numerical investigation of extinction and ignition limits in laminar nonpremixed counterflowing hydrogen-air streams for both elementary and reduced chemistry. *Combustion and Flame* **102**, 329–340 (1995).
- [23] Ó Conaire, M., Curran, H. J., Simmie, J. M., Pitz, W. J. & Westbrook, C. K. A comprehensive modeling study of hydrogen oxidation. *International journal of chemical kinetics* **36**, 603–622 (2004).
- [24] Van Oijen, J. & De Goey, L. Modelling of premixed laminar flames using flamelet-generated manifolds. *Combustion science and technology* **161**, 113–137 (2000).
- [25] Haworth, D. C. Progress in probability density function methods for turbulent reacting flows. *Progress in Energy and combustion Science* **36**, 168–259 (2010).
- [26] Mukundakumar, N., Efimov, D., Beishuizen, N. & van Oijen, J. A new preferential diffusion model applied to FGM simulations of hydrogen flames. *Combustion Theory and Modelling* **25**, 1245–1267 (2021).
- [27] Jones, W. & Navarro-Martinez, S. Study of hydrogen auto-ignition in a turbulent air co-flow using a large eddy simulation approach. *Computers & fluids* **37**, 802–808 (2008).

- [28] Valiño, L., Mustata, R. & Letaief, K. B. Consistent behavior of eulerian monte carlo fields at low reynolds numbers. *Flow, Turbulence and Combustion* **96**, 503–512 (2016).
- [29] Chen, Z. X. *et al.* Large eddy simulation of a dual swirl gas turbine combustor: Flame/flow structures and stabilisation under thermoacoustically stable and unstable conditions. *Combustion and Flame* **203**, 279–300 (2019).
- [30] Cabra, R. *et al.* Simultaneous laser raman-rayleigh-lif measurements and numerical modeling results of a lifted turbulent h<sub>2</sub>/n<sub>2</sub> jet flame in a vitiated coflow. *Proceedings of the Combustion Institute* **29**, 1881–1888 (2002).
- [31] Cao, R. R., Pope, S. B. & Masri, A. R. Turbulent lifted flames in a vitiated coflow investigated using joint PDF calculations. *Combustion and flame* **142**, 438–453 (2005).
- [32] Hansinger, M. *et al.* The eulerian stochastic fields method applied to large eddy simulations of a piloted flame with inhomogeneous inlet. *Flow, Turbulence and Combustion* **105**, 837–867 (2020).
- [33] Ferrante, G., Kruljevic, B. & Langella, I. *Differential diffusion modelling of a lifted H<sub>2</sub> flame in vitiated coflow using LES-flamelet approach* (2023).
- [34] Regele, J. D., Knudsen, E., Pitsch, H. & Blanquart, G. A two-equation model for non-unity lewis number differential diffusion in lean premixed laminar flames. *Combustion and flame* **160**, 240–250 (2013).
- [35] Bilger, R., Stårner, S. & Kee, R. On reduced mechanisms for methane-air combustion in nonpremixed flames. *Combustion and Flame* **80**, 135–149 (1990).
- [36] Celik, I. B., Cehreli, Z. N. & Yavuz, I. Index of Resolution Quality for Large Eddy Simulations. *Journal of Fluids Engineering* **127**, 949–958 (2005).
- [37] Celik, I., Klein, M. & Janicka, J. Assessment Measures for Engineering LES Applications. *Journal of Fluids Engineering* **131**, 031102 (2009).
- [38] Rubinstein, R. & Clark, T. T. “equilibrium” and “non-equilibrium” turbulence. *Theoretical and applied mechanics letters* **7**, 301–305 (2017).
- [39] Chemical-kinetic mechanisms for combustion applications. San Diego Mechanism web page, Mechanical and Aerospace Engineering (Combustion Research), University of California at San Diego. URL <http://combustion.ucsd.edu>. Last Accessed: 2024-01-04.
- [40] Weydahl, T., Poyyapakkam, M., Seljeskog, M. & Haugen, N. E. L. Assessment of existing h<sub>2</sub>/o<sub>2</sub> chemical reaction mechanisms at reheat gas turbine conditions. *international journal of hydrogen energy* **36**, 12025–12034 (2011).

# 5

## Conclusion

Hydrogen combustion is seen as a crucial step in reducing aviation emissions, but its unique characteristics necessitate novel combustion designs. Developing these designs requires a model capable of handling the complexities of hydrogen and high turbulence, and the ability to accommodate both premixed and non-premixed combustion modes. Furthermore, the model should be adaptable enough to study phenomena relevant to hydrogen combustion, e.g.  $\text{NO}_x$  formation, effects of high strain rates, etc. A Large Eddy Simulation (LES) model that integrates Eulerian Stochastic Field (ESF) closure with Flamelet Generated Manifold (FGM) tabulation emerges as the most suitable candidate. In this study, the model (FGM-ESF) has been implemented and specifically adapted for partially premixed hydrogen flames, undergoing comprehensive development and detailed analysis. The newly developed hybrid model demonstrates its predictive capability for such flames, a first in this domain. It was evaluated against both experimental data and the more classical and computationally intensive fully transported chemistry ESF method (FC-ESF).

The FGM-ESF model aligns well with experimental data in predicting mean velocity, temperature, and mixture fraction, though it slightly overestimates the root mean square (rms) values of these parameters. This is caused by slower mixing rates. Despite this, it closely approximates the FC-ESF outcomes. Notably, the model's performance shows minimal sensitivity to the number of Eulerian stochastic fields used, with two fields being sufficient for effective simulation. Further investigation into instantaneous burning states indicated that the FGM-ESF model generally predicts faster reaction times, except in lean or very rich mixture conditions. Near the stoichiometric point, discrepancies due to non-premixed burning are effectively corrected with a compensatory factor, despite the FGM's reliance on premixed flamelets. In premixed dominated regions, the FGM-ESF model captures key qualitative features, including super-adiabatic conditions and double-peak conditional reaction rates, with minimal impact on overall statistical predictions. From a computational perspective, the FGM-ESF model is less impacted by increases in stochastic fields and has reached a maximum efficiency of 10,000 cells per processor. Further enhancements, particularly in optimizing parallel computing routines, could increase its efficiency.

The FGM-ESF model, with its promising predictive capabilities and potential for reduced computational costs, especially in larger meshes, stands as a valuable tool in advancing precise and cost-effective hydrogen combustion technologies. Several possible next steps can be taken to extend the capabilities of the model.

A first recommendation is to improve the efficiency of the interpolation routine, which is the limiting factor in computation speeds. At present a simple 2D interpolation routine is used. However, when moving to more controlling variables there are better alternatives like Delaunay triangulation or using Artificial Neural Network (ANN) to reduce computational costs.

On a more fundamental level, differential diffusion effects can be analysed for a case where they are more important, e.g. micro-mixing concept. These effects are more pronounced in flows that are lean and less turbulent than the Cabra flame. If the inclusion of differential effects in the flamelets

should prove to be insufficient, there are ways to improve the FGM-ESF method. On the resolved scales, an additional tabulated term can be added to address the impact of unequal Lewis numbers on the diffusion of the controlling variables. This addition has already been implemented in the solver, but not yet validated. An adjustment can also be made on the subgrid-scale. Both solvers implicitly assume equal Lewis numbers in the micro-mixing term. A mean drift term can be added to account for differential diffusion for FC-ESF. It alters the stochastic diffusion term in physical space to a diffusion in composition space for the different species. To use this for FGM-ESF, the term needs to be adapted to the controlling variables.

The transport equation for the progress variable needs a correction for the source term. This term has been ignored at the moment. However, analysis shows that the correction appears to be effective in retrieving the correct burning state near stoichiometry. The correction does lead to a negative source term which causes numerical instabilities. Truncating the negative values to zero is a solution that can be investigated.

The results of the Cabra flame are also weakly sensitive to the number of fields due to this dominance of turbulent mixing on molecular diffusion. The prediction of the subgrid variance, i.e. the second moment between the fields, does not have a large impact on the overall results for this flame. This variance can not be measured as it is inherently linked to the LES method. However, a comparison with the FGM-PPDF method can give valuable insights into how many fields are needed to retrieve this statistic and to what extent the presumed PDF agrees with its discrete Monte Carlo counterpart. An analysis of computational costs between these two solvers is also useful.

Regarding the FGM tabulation, [112] has shown that the non-premixed FGM tabulation works well for partially premixed flames. A counterflow diffusion flamelet database is used with a similar set of controlling variables. A comparison with REDIM tabulation can also be useful.

On a more applied level, the model can be used to study several practical problems. The San Diego and Ó Conaire mechanisms do not include  $\text{NO}_x$  pathways. Switching to a mechanism that does (e.g. [57]) opens the possibility of studying the production of these important pollutants. It is still an open question whether nitrogen-containing species have to be added to the progress variable, like in [113]. The FGM-ESF solver can make significant gains in terms of computational efficiency compared to the FC-ESF solver for larger domains. This makes it possible to study lean-burn and highly-strained combustion technologies for practical combustor domains. In that state, it achieves its final goal in helping towards the development towards a hydrogen aircraft engine.

# References

- [1] Y. G. Zhang, M. Pagani, Z. Liu, S. M. Bohaty, and R. DeConto, "A 40-million-year history of atmospheric  $\text{CO}_2$ ," *Philosophical Transactions of the Royal Society A: Mathematical, Physical and Engineering Sciences*, vol. 371, no. 2001, p. 20130096, 2013.
- [2] R. B. Jackson, E. Solomon, J. Canadell, M. Cargnello, and C. Field, "Methane removal and atmospheric restoration," *Nature Sustainability*, vol. 2, no. 6, pp. 436–438, 2019.
- [3] A. Durocher, M. Meulemans, P. Versailles, G. Bourque, and J. M. Bergthorson, "Back to basics – no concentration measurements in atmospheric lean-to-rich, low-temperature, premixed hydrogen–air flames diluted with argon," *Proceedings of the Combustion Institute*, vol. 38, no. 2, pp. 2093–2100, 2021.
- [4] A. L. Purohit, A. Nalbandyan, P. C. Malte, and I. V. Novosselov, "NNH mechanism in low- $\text{NO}_x$  hydrogen combustion: Experimental and numerical analysis of formation pathways," *Fuel*, vol. 292, p. 120186, 2021.
- [5] S. Iavarone, M. Cafiero, M. Ferrarotti, F. Contino, and A. Parente, "A multiscale combustion model formulation for  $\text{NO}_x$  predictions in hydrogen enriched jet flames," *International journal of hydrogen energy*, vol. 44, no. 41, pp. 23436–23457, 2019.
- [6] A. J. Haagen-Smit, "Chemistry and physiology of los angeles smog," *Industrial & Engineering Chemistry*, vol. 44, no. 6, pp. 1342–1346, 1952.
- [7] B. Rani, U. Singh, A. Chuhan, D. Sharma, and R. Maheshwari, "Photochemical smog pollution and its mitigation measures," *Journal of Advanced Scientific Research*, vol. 2, no. 04, pp. 28–33, 2011.
- [8] P. M. Vitousek, J. D. Aber, R. W. Howarth, *et al.*, "Human alteration of the global nitrogen cycle: Sources and consequences," *Ecological applications*, vol. 7, no. 3, pp. 737–750, 1997.
- [9] A. Singh and M. Agrawal, "Acid rain and its ecological consequences," *Journal of Environmental Biology*, vol. 29, no. 1, p. 15, 2007.
- [10] T.-M. Chen, W. G. Kuschner, J. Gokhale, and S. Shofer, "Outdoor air pollution: Nitrogen dioxide, sulfur dioxide, and carbon monoxide health effects," *The American journal of the medical sciences*, vol. 333, no. 4, pp. 249–256, 2007.
- [11] S. Anwar, F. Khan, Y. Zhang, and A. Djire, "Recent development in electrocatalysts for hydrogen production through water electrolysis," *International Journal of Hydrogen Energy*, vol. 46, no. 63, pp. 32284–32317, 2021.
- [12] A. I. Osman, N. Mehta, A. M. Elgarahy, *et al.*, "Hydrogen production, storage, utilisation and environmental impacts: A review," *Environmental Chemistry Letters*, pp. 1–36, 2022.
- [13] A. Gangoli Rao, F. Yin, and J. P. van Buijtenen, "A hybrid engine concept for multi-fuel blended wing body," *Aircraft Engineering and Aerospace Technology: An International Journal*, vol. 86, no. 6, pp. 483–493, 2014.
- [14] A. Baroutaji, T. Wilberforce, M. Ramadan, and A. G. Olabi, "Comprehensive investigation on hydrogen and fuel cell technology in the aviation and aerospace sectors," *Renewable and Sustainable Energy Reviews*, vol. 106, pp. 31–40, May 2019.
- [15] A. Kirubakaran, S. Jain, and R. Nema, "The pem fuel cell system with dc/dc boost converter: Design, modeling and simulation," *International Journal of recent trends in Engineering*, vol. 1, no. 3, pp. 157–161, 2009.
- [16] M. Li, Z. Wang, R. Xu, X. Zhang, Z. Chen, and Q. Wang, "Advances in plasma-assisted ignition and combustion for combustors of aerospace engines," *Aerospace Science and Technology*, vol. 117, p. 106952, 2021.
- [17] E. J. Adler and J. R. Martins, "Hydrogen-powered aircraft: Fundamental concepts, key technologies, and environmental impacts," *Progress in Aerospace Sciences*, vol. 141, p. 100922, 2023.

- [18] C. T. Chong and J.-H. Ng, "Chapter 4 - combustion performance of biojet fuels," in *Biojet Fuel in Aviation Applications*, C. T. Chong and J.-H. Ng, Eds., Elsevier, 2021, pp. 175–230, ISBN: 978-0-12-822854-8.
- [19] M. Ilbas, A. Crayford, İ. Yilmaz, P. Bowen, and N. Syred, "Laminar-burning velocities of hydrogen–air and hydrogen–methane–air mixtures: An experimental study," *International Journal of Hydrogen Energy*, vol. 31, no. 12, pp. 1768–1779, 2006.
- [20] E.-S. Cho and S. H. Chung, "Improvement of flame stability and NO<sub>x</sub> reduction in hydrogen-added ultra lean premixed combustion," en, *Journal of Mechanical Science and Technology*, vol. 23, no. 3, pp. 650–658, Mar. 2009.
- [21] I. Yakovenko, M. Ivanov, A. Kiverin, and K. Melnikova, "Large-scale flame structures in ultra-lean hydrogen-air mixtures," *International Journal of Hydrogen Energy*, vol. 43, no. 3, pp. 1894–1901, 2018.
- [22] S. Biswas and L. Qiao, "Ignition of ultra-lean premixed hydrogen/air by an impinging hot jet," *Applied energy*, vol. 228, pp. 954–964, 2018.
- [23] J. Ziemann, F. Shum, M. Moore, *et al.*, "Low-nox combustors for hydrogen fueled aero engine," *International Journal of Hydrogen Energy*, vol. 23, no. 4, pp. 281–288, 1998.
- [24] C. Marek, T. Smith, and K. Kundu, "Low emission hydrogen combustors for gas turbines using lean direct injection," in *41st AIAA/ASME/SAE/ASEE joint propulsion conference & exhibit*, 2005, p. 3776.
- [25] D. S. Endicott, "Experimental development of a lean direct injection combustor utilizing high-low swirl intensity combinations," 2014.
- [26] G. Babazzi, P. Q. Gauthier, P. Agarwal, J. McClure, and V. Sethi, "NO<sub>x</sub> emissions predictions for a hydrogen micromix combustion system," in *Turbo Expo: Power for Land, Sea, and Air*, American Society of Mechanical Engineers, vol. 58608, 2019, V003T03A008.
- [27] A. H. Ayed, K. Kusterer, H.-W. Funke, J. Keinz, C. Striegan, and D. Bohn, "Improvement study for the dry-low-nox hydrogen micromix combustion technology," *Propulsion and Power Research*, vol. 4, no. 3, pp. 132–140, 2015.
- [28] T. Lieuwen, V. McDonell, D. Santavicca, and T. Sattelmayer, "Burner development and operability issues associated with steady flowing syngas fired combustors," *Combustion Science and Technology*, vol. 180, no. 6, pp. 1169–1192, 2008.
- [29] T. G. Reichel, S. Terhaar, and C. O. Paschereit, "Flashback resistance and fuel–air mixing in lean premixed hydrogen combustion," *Journal of Propulsion and Power*, vol. 34, no. 3, pp. 690–701, 2018.
- [30] A. G. Rao and A. Bhat, "Hybrid combustion system for future aero engines," in *Proceedings of the 2nd National Propulsion Conference*, IIT Bombay Powai, Mumbai, 2015, pp. 1–9.
- [31] S. B. Pope, "Turbulent flows," *Measurement Science and Technology*, vol. 12, no. 11, pp. 2020–2021, 2001.
- [32] P.-K. Yeung and S. B. Pope, "Lagrangian statistics from direct numerical simulations of isotropic turbulence," *Journal of Fluid Mechanics*, vol. 207, pp. 531–586, 1989.
- [33] J. Bardina, J. Ferziger, and W. Reynolds, "Improved subgrid-scale models for large-eddy simulation," in *13th fluid and plasmadynamics conference*, 1980, p. 1357.
- [34] J. Smagorinsky, "General circulation experiments with the primitive equations: I. the basic experiment," *Monthly weather review*, vol. 91, no. 3, pp. 99–164, 1963.
- [35] D. Haworth and K. Jansen, "Large-eddy simulation on unstructured deforming meshes: Towards reciprocating ic engines," *Computers & fluids*, vol. 29, no. 5, pp. 493–524, 2000.
- [36] M. Germano, U. Piomelli, P. Moin, and W. H. Cabot, "A dynamic subgrid-scale eddy viscosity model," *Physics of Fluids A: Fluid Dynamics*, vol. 3, no. 7, pp. 1760–1765, 1991.
- [37] D. K. Lilly, "A proposed modification of the germano subgrid-scale closure method," *Physics of Fluids A: Fluid Dynamics*, vol. 4, no. 3, pp. 633–635, 1992.
- [38] A. Avdić, G. Kuenne, F. di Mare, and J. Janicka, "LES combustion modeling using the Eulerian stochastic field method coupled with tabulated chemistry," en, *Combustion and Flame*, Special Issue in Honor of Norbert Peters, vol. 175, pp. 201–219, Jan. 2017.
- [39] W. Jones and S. Navarro-Martinez, "Large eddy simulation of autoignition with a subgrid probability density function method," *Combustion and Flame*, vol. 150, no. 3, pp. 170–187, 2007.

- [40] B. Fiorina, R. Vicquelin, P. Auzillon, N. Darabiha, O. Gicquel, and D. Veynante, "A filtered tabulated chemistry model for LES of premixed combustion," en, *Combustion and Flame*, vol. 157, no. 3, pp. 465–475, Mar. 2010.
- [41] W. P. Jones and V. N. Prasad, "Large Eddy Simulation of the Sandia Flame Series (D–F) using the Eulerian stochastic field method," en, *Combustion and Flame*, vol. 157, no. 9, pp. 1621–1636, Sep. 2010.
- [42] S. Navarro-Martinez and A. Kronenburg, "Flame stabilization mechanisms in lifted flames," *Flow, Turbulence and Combustion*, vol. 87, pp. 377–406, 2011.
- [43] W. P. Jones, A. J. Marquis, and V. N. Prasad, "LES of a turbulent premixed swirl burner using the Eulerian stochastic field method," en, *Combustion and Flame*, vol. 159, no. 10, pp. 3079–3095, Oct. 2012.
- [44] E. Knudsen, H. Kolla, E. R. Hawkes, and H. Pitsch, "LES of a premixed jet flame DNS using a strained flamelet model," en, *Combustion and Flame*, vol. 160, no. 12, pp. 2911–2927, Dec. 2013.
- [45] I. Stanković, E. Mastorakos, and B. Merci, "Les-cmc simulations of different auto-ignition regimes of hydrogen in a hot turbulent air co-flow," *Flow, turbulence and combustion*, vol. 90, pp. 583–604, 2013.
- [46] I. Langella and N. Swaminathan, "Unstrained and strained flamelets for LES of premixed combustion," *Combustion Theory and Modelling*, vol. 20, no. 3, pp. 410–440, May 2016, Publisher: Taylor & Francis \_eprint: <https://doi.org/10.1080/13647830.2016.1140230>.
- [47] W.-W. Kim and S. Menon, "A new dynamic one-equation subgrid-scale model for large eddy simulations," in *33rd Aerospace Sciences Meeting and Exhibit*, 1995, p. 356.
- [48] F. Nicoud and F. Ducros, "Subgrid-scale stress modelling based on the square of the velocity gradient tensor," *Flow, turbulence and Combustion*, vol. 62, no. 3, pp. 183–200, 1999.
- [49] M. Hansinger, T. Zirwes, J. Zips, *et al.*, "The Eulerian Stochastic Fields Method Applied to Large Eddy Simulations of a Piloted Flame with Inhomogeneous Inlet," en, *Flow, Turbulence and Combustion*, vol. 105, no. 3, pp. 837–867, Sep. 2020.
- [50] A. C. Benim, B. Pfeiffelmann, P. Ocloñ, and J. Taler, "Computational investigation of a lifted hydrogen flame with les and fgm," *Energy*, vol. 173, pp. 1172–1181, 2019.
- [51] P. Breda, C. Yu, U. Maas, and M. Pfitzner, "Validation of an Eulerian Stochastic Fields Solver Coupled with Reaction–Diffusion Manifolds on LES of Methane/Air Non-premixed Flames," en, *Flow, Turbulence and Combustion*, vol. 107, no. 2, pp. 441–477, Aug. 2021.
- [52] I. M. De Cachinho Cordeiro, H. Liu, A. C. Y. Yuen, T. B. Y. Chen, A. Li, and G. H. Yeoh, "Numerical assessment of les subgrid-scale turbulence models for expandable particles in fire suppression," *Experimental and Computational Multiphase Flow*, pp. 1–12, 2021.
- [53] A. Vreman, "An eddy-viscosity subgrid-scale model for turbulent shear flow: Algebraic theory and applications," *Physics of fluids*, vol. 16, no. 10, pp. 3670–3681, 2004.
- [54] A. Yuen, G. Yeoh, V. Timchenko, S. Cheung, and T. Chen, "Study of three les subgrid-scale turbulence models for predictions of heat and mass transfer in large-scale compartment fires," *Numerical Heat Transfer, Part A: Applications*, vol. 69, no. 11, pp. 1223–1241, 2016.
- [55] A. Vreman, R. Bastiaans, and B. Geurts, "A similarity subgrid model for premixed turbulent combustion," *Flow, turbulence and combustion*, vol. 82, pp. 233–248, 2009.
- [56] F. Nicoud, H. B. Toda, O. Cabrit, S. Bose, and J. Lee, "Using singular values to build a subgrid-scale model for large eddy simulations," *Physics of fluids*, vol. 23, no. 8, p. 085 106, 2011.
- [57] T. Capurso, D. Laera, E. Riber, and B. Cuenot, "NO<sub>x</sub> pathways in lean partially premixed swirling H<sub>2</sub>–air turbulent flame," en, *Combustion and Flame*, vol. 248, p. 112 581, Feb. 2023.
- [58] S. Buhl, F. Dietzsch, C. Buhl, and C. Hasse, "Comparative study of turbulence models for scale-resolving simulations of internal combustion engine flows," *Computers & Fluids*, vol. 156, pp. 66–80, 2017.
- [59] J. Warnatz, U. Maas, R. W. Dibble, and J. Warnatz, *Combustion*. Springer, 2006.
- [60] K. K. Kuo, "Principles of combustion," 1986.
- [61] C. J. Greenshields and H. G. Weller, *Notes on computational fluid dynamics: General principles*. CFD Direct Limited, 2022.
- [62] S. V. Patankar and D. B. Spalding, "A calculation procedure for heat, mass and momentum transfer in three-dimensional parabolic flows," in *Numerical prediction of flow, heat transfer, turbulence and combustion*, Elsevier, 1983, pp. 54–73.

- [63] R. I. Issa, "Solution of the implicitly discretised fluid flow equations by operator-splitting," *Journal of computational physics*, vol. 62, no. 1, pp. 40–65, 1986.
- [64] B. Fiorina, D. Veynante, and S. Candel, "Modeling Combustion Chemistry in Large Eddy Simulation of Turbulent Flames," en, *Flow, Turbulence and Combustion*, vol. 94, no. 1, pp. 3–42, Jan. 2015.
- [65] R. A. Yetter, F. Dryer, and H. Rabitz, "A comprehensive reaction mechanism for carbon monoxide/hydrogen/oxygen kinetics," *Combustion Science and Technology*, vol. 79, no. 1-3, pp. 97–128, 1991.
- [66] M. Mueller, T. Kim, R. Yetter, and F. Dryer, "Flow reactor studies and kinetic modeling of the h<sub>2</sub>/o<sub>2</sub> reaction," *International journal of chemical kinetics*, vol. 31, no. 2, pp. 113–125, 1999.
- [67] J. Li, Z. Zhao, A. Kazakov, and F. L. Dryer, "An updated comprehensive kinetic model of hydrogen combustion," *International journal of chemical kinetics*, vol. 36, no. 10, pp. 566–575, 2004.
- [68] G. Balakrishnan, M. Smooke, and F. Williams, "A numerical investigation of extinction and ignition limits in laminar nonpremixed counterflowing hydrogen-air streams for both elementary and reduced chemistry," *Combustion and Flame*, vol. 102, no. 3, pp. 329–340, 1995.
- [69] M. Ó Conaire, H. J. Curran, J. M. Simmie, W. J. Pitz, and C. K. Westbrook, "A comprehensive modeling study of hydrogen oxidation," en, *International Journal of Chemical Kinetics*, vol. 36, no. 11, pp. 603–622, 2004, \_eprint: <https://onlinelibrary.wiley.com/doi/pdf/10.1002/kin.20036>.
- [70] A. Kazakov and M. Frenklach, *Drm19 reaction mechanism*, 1994.
- [71] A. Pellissier-Tanon, G. Morgado, L. Jullien, and A. Lemarchand, "Quasi-steady-state and partial-equilibrium approximations in chemical kinetics: One stage beyond the elimination of a fast variable," 2021.
- [72] J. A. van Oijen and L. Goey, "Modelling of Premixed Laminar Flames using Flamelet-Generated Manifolds," *Combustion Science and Technology*, vol. 161, no. 1, pp. 113–137, Dec. 2000, Publisher: Taylor & Francis \_eprint: <https://doi.org/10.1080/00102200008935814>.
- [73] S. Lam and D. Goussis, "The csp method for simplifying kinetics," *International journal of chemical kinetics*, vol. 26, no. 4, pp. 461–486, 1994.
- [74] V. Bykov and U. Maas, "The extension of the ildm concept to reaction–diffusion manifolds," *Combustion Theory and Modelling*, vol. 11, no. 6, pp. 839–862, 2007.
- [75] O. Gicquel, N. Darabiha, and D. Thévenin, "Liminar premixed hydrogen/air counterflow flame simulations using flame prolongation of ildm with differential diffusion," *Proceedings of the Combustion Institute*, vol. 28, no. 2, pp. 1901–1908, 2000.
- [76] C. D. Pierce and P. Moin, "Progress-variable approach for large-eddy simulation of non-premixed turbulent combustion," *Journal of fluid Mechanics*, vol. 504, pp. 73–97, 2004.
- [77] N. Peters, "Laminar flamelet concepts in turbulent combustion," in *Symposium (International) on combustion*, Elsevier, vol. 21, 1988, pp. 1231–1250.
- [78] J. Van Oijen, A. Donini, R. Bastiaans, J. ten Thijsse Boonkkamp, and L. De Goey, "State-of-the-art in premixed combustion modeling using flamelet generated manifolds," *Progress in Energy and Combustion Science*, vol. 57, pp. 30–74, 2016.
- [79] R. Bilger, "The structure of diffusion flames," *Combustion science and technology*, vol. 13, no. 1-6, pp. 155–170, 1976.
- [80] X. Chen, H. Böttler, A. Scholtissek, C. Hasse, and Z. Chen, "Effects of stretch-chemistry interaction on chemical pathways for strained and curved hydrogen/air premixed flames," en, *Combustion and Flame*, vol. 232, p. 111 532, Oct. 2021.
- [81] X. Wen, T. Zirwes, A. Scholtissek, *et al.*, "Flame structure analysis and composition space modeling of thermodynamically unstable premixed hydrogen flames — Part I: Atmospheric pressure," en, *Combustion and Flame*, vol. 238, p. 111 815, Apr. 2022.
- [82] G. Fru, G. Janiga, and D. Thévenin, "Impact of volume viscosity on the structure of turbulent premixed flames in the thin reaction zone regime," *Flow, turbulence and combustion*, vol. 88, pp. 451–478, 2012.
- [83] A. Scholtissek, F. Dietzsch, M. Gauding, and C. Hasse, "In-situ tracking of mixture fraction gradient trajectories and unsteady flamelet analysis in turbulent non-premixed combustion," *Combustion and Flame*, vol. 175, pp. 243–258, 2017.

- [84] A. Scholtissek, P. Domingo, L. Vervisch, and C. Hasse, "A self-contained composition space solution method for strained and curved premixed flamelets," en, *Combustion and Flame*, vol. 207, pp. 342–355, Sep. 2019.
- [85] A. R. Kerstein, W. T. Ashurst, and F. A. Williams, "Field equation for interface propagation in an unsteady homogeneous flow field," *Phys. Rev. A*, vol. 37, pp. 2728–2731, 7 Apr. 1988.
- [86] M. Boger, D. Veynante, H. Boughanem, and A. Trouvé, "Direct numerical simulation analysis of flame surface density concept for large eddy simulation of turbulent premixed combustion," in *Symposium (International) on Combustion*, Elsevier, vol. 27, 1998, pp. 917–925.
- [87] C. Duwig, "Study of a filtered flamelet formulation for large eddy simulation of premixed turbulent flames," *Flow, Turbulence and Combustion*, vol. 79, pp. 433–454, 2007.
- [88] O. Colin, F. Ducros, D. Veynante, and T. Poinso, "A thickened flame model for large eddy simulations of turbulent premixed combustion," *Physics of fluids*, vol. 12, no. 7, pp. 1843–1863, 2000.
- [89] E. Fedina, C. Fureby, G. Bulat, and W. Meier, "Assessment of Finite Rate Chemistry Large Eddy Simulation Combustion Models," en, *Flow, Turbulence and Combustion*, vol. 99, no. 2, pp. 385–409, Sep. 2017.
- [90] B. Magnussen, "19th aiaa aerospace science meeting," *Saint-Louis, Missouri, 1991*, 1981.
- [91] E. Giacomazzi, C. Bruno, and B. Favini, "Fractal modelling of turbulent combustion," *Combustion Theory and Modelling*, vol. 4, no. 4, p. 391, 2000.
- [92] S. Navarro-Martinez, A. Kronenburg, and F. D. Mare, "Conditional moment closure for large eddy simulations," *Flow, Turbulence and Combustion*, vol. 75, pp. 245–274, 2005.
- [93] A. W. Cook and J. J. Riley, "A subgrid model for equilibrium chemistry in turbulent flows," *Physics of fluids*, vol. 6, no. 8, pp. 2868–2870, 1994.
- [94] L. Valino, R. Mustata, and K. B. Letaief, "Consistent behavior of eulerian monte carlo fields at low reynolds numbers," *Flow, Turbulence and Combustion*, vol. 96, pp. 503–512, 2016.
- [95] M. S. Celtek and A. Pınarbaşı, "Investigations on performance and emission characteristics of an industrial low swirl burner while burning natural gas, methane, hydrogen-enriched natural gas and hydrogen as fuels," *International Journal of Hydrogen Energy*, vol. 43, no. 2, pp. 1194–1207, 2018.
- [96] J. B. Bell, M. Day, and M. Lijewski, "Simulation of nitrogen emissions in a premixed hydrogen flame stabilized on a low swirl burner," *Proceedings of the Combustion Institute*, vol. 34, no. 1, pp. 1173–1182, 2013.
- [97] T. Shoji, S. Tachibana, T. Suzuki, Y. Nakazumi, and T. Yokomori, "A new pattern of flame/flow dynamics for lean-premixed, low-swirl hydrogen turbulent jet flames under thermoacoustic instability," *Proceedings of the Combustion Institute*, vol. 38, no. 2, pp. 2835–2843, 2021.
- [98] T. Shoji, Y. Iwasaki, K. Kodai, S. Yoshida, S. Tachibana, and T. Yokomori, "Effects of flame behaviors on combustion noise from lean-premixed hydrogen low-swirl flames," *AIAA journal*, vol. 58, no. 10, pp. 4505–4521, 2020.
- [99] R. Cabra, T. Myhrvold, J. Chen, R. Dibble, A. Karpetsis, and R. Barlow, "Simultaneous laser raman-rayleigh-lif measurements and numerical modeling results of a lifted turbulent h<sub>2</sub>/n<sub>2</sub> jet flame in a vitiated coflow," *Proceedings of the Combustion Institute*, vol. 29, no. 2, pp. 1881–1888, 2002.
- [100] R. Gordon, S. Starner, A. Masri, and R. Bilger, "Further characterisation of lifted hydrogen and methane flames issuing into a vitiated coflow," in *Proceedings of the 5th Asia-Pacific conference on combustion*, 2005, pp. 333–336.
- [101] A. Masri, R. Cao, S. Pope, and G. Goldin, "Pdf calculations of turbulent lifted flames of h<sub>2</sub>/n<sub>2</sub> fuel issuing into a vitiated co-flow," *Combustion Theory and Modelling*, vol. 8, no. 1, p. 1, 2003.
- [102] R. R. Cao, S. B. Pope, and A. R. Masri, "Turbulent lifted flames in a vitiated coflow investigated using joint pdf calculations," *Combustion and flame*, vol. 142, no. 4, pp. 438–453, 2005.
- [103] R. L. Gordon, A. R. Masri, S. B. Pope, and G. M. Goldin, "A numerical study of auto-ignition in turbulent lifted flames issuing into a vitiated co-flow," *Combustion Theory and Modelling*, vol. 11, no. 3, pp. 351–376, 2007.
- [104] H. Wang and S. B. Pope, "Lagrangian investigation of local extinction, re-ignition and auto-ignition in turbulent flames," *Combustion Theory and Modelling*, vol. 12, no. 5, pp. 857–882, 2008.

- [105] Z. Ren and S. B. Pope, "Sensitivity calculations in pdf modelling of turbulent flames," *Proceedings of the Combustion Institute*, vol. 32, no. 1, pp. 1629–1637, 2009.
- [106] K. Gkagkas and R. Lindstedt, "The impact of reduced chemistry on auto-ignition of h<sub>2</sub> in turbulent flows," *Combustion Theory and Modelling*, vol. 13, no. 4, pp. 607–643, 2009.
- [107] J. Lee and Y. Kim, "Dqmom based pdf transport modeling for turbulent lifted nitrogen-diluted hydrogen jet flame with autoignition," *International journal of hydrogen energy*, vol. 37, no. 23, pp. 18 498–18 508, 2012.
- [108] S. M. M. Najafizadeh, M. T. Sadeghi, R. Sotudeh-Gharebagh, and D. J. Roekaerts, "Chemical structure of autoignition in a turbulent lifted h<sub>2</sub>/n<sub>2</sub> jet flame issuing into a vitiated coflow," *Combustion and flame*, vol. 160, no. 12, pp. 2928–2940, 2013.
- [109] W. Jones and S. Navarro-Martinez, "Study of hydrogen auto-ignition in a turbulent air co-flow using a large eddy simulation approach," *Computers & fluids*, vol. 37, no. 7, pp. 802–808, 2008.
- [110] W. Han, V. Raman, and Z. Chen, "Les/pdf modeling of autoignition in a lifted turbulent flame: Analysis of flame sensitivity to differential diffusion and scalar mixing time-scale," *Combustion and Flame*, vol. 171, pp. 69–86, 2016.
- [111] G. Ferrante, B. Kruljevic, and I. Langella, "Differential diffusion modelling of a lifted H<sub>2</sub> flame in vitiated coflow using LES-flamelet approach," in *12th Mediterranean Combustion Symposium*, 2023.
- [112] W. Ramaekers, J. Van Oijen, and L. De Goey, "A priori testing of flamelet generated manifolds for turbulent partially premixed methane/air flames," *Flow, turbulence and combustion*, vol. 84, pp. 439–458, 2010.
- [113] G. Godel, P. Domingo, and L. Vervisch, "Tabulation of nox chemistry for large-eddy simulation of non-premixed turbulent flames," *Proceedings of the Combustion Institute*, vol. 32, no. 1, pp. 1555–1561, 2009.